

Computational fluid dynamics in the stented arteria femoralis superficialis

Master thesis Technical Medicine

Lisa Rutten



Computational fluid dynamics in the stented arteria femoralis superficialis

A dissertation presented

by

Lisa Rutten

to

The Department of Science and
Technology

In partial fulfilment of the requirements
for the degree of
Master of Science
in the subject of
Technical Medicine

Graduation committee

Chair & medical supervisor	Prof.dr. M.M.P.J. Reijnen
Technical supervisor	Dr.ir. R. Hagmeijer
Daily supervisor	L. van de Velde, MSc.BMus.
Process supervisor	Drs. P.A. van Katwijk
External member	J.K. van Zandwijk, MSc.

Defense

14 May 2020 – Digital conference

Abstract

Introduction: Visualizing the blood flow could provide a better understanding and improved prediction of the development of an in-stent restenosis in the *arteria femoralis superficialis* (AFS). Computational fluid dynamics (CFD) could be used to simulate the complex blood flow, but simplifications and assumptions are necessary to reduce the complexity of the computational model and compensate for the lack of (adequate) patient-specific data that could affect the CFD solution. In this thesis the effect of uncertainty in the patient-specific geometry and inlet velocity profile on the CFD solution in the stented AFS is investigated.

Method: The uncertainty in lumen segmentation that is induced by blooming artifacts by radiopaque stent markers and stent-in-stent placement was quantified in-vitro. The visible lumen, strut thickness, contrast-to-noise ratio and signal-to-noise ratio were compared between conventional and spectral image reconstructions and analysis locations. Sensitivity of the CFD solution to uncertainty in the lumen diameter near radiopaque stent markers in the patient-specific geometry was analyzed. Furthermore, an analytical Womersley and measured echo particle image velocimetry (echo PIV) velocity profile were compared. Velocity streamlines and regions of low time-averaged wall shear stress (TAWSS) (<0.4 Pa) were visualized to analyze the effect of on the CFD solution.

Results: The blooming artifact showed the largest reduction in the conventional iterative model reconstruction (IMR) and was most prominent near proximal/distal radiopaque stent markers causing an underestimation of the in-stent lumen of 33%. Uncertainty in the geometry near proximal/distal radiopaque stent markers caused local changes in the CFD solution. Overestimation of approximately 33% resulted in an increased region of low TAWSS of a factor ten in the proximal AFS. Over- and underestimation of approximately 16% caused an increased region of low TAWSS of a factor three and two, respectively, in the AFS, resulting in a global difference of approximately 10%. Uncertainty in inlet velocity profile induced local changes in the CFD

solution of 30% in the AFC, resulting in a global difference of 14.6%. Differences in flow rate caused global differences in the CFD solution up to 250%.

Conclusion: Blooming showed the largest reduction in the IMR image reconstruction and was most prominent near proximal/distal radiopaque stent markers. Uncertainty in the geometry near these stent markers caused local changes in the CFD solution. Uncertainty in the inlet velocity profile resulted in local changes in the CFD solution as well. The effect of uncertainty in the geometry and inlet velocity profile on the global CFD solution were significantly smaller than the effect of the flow rate on the global CFD solution.

Preface

Before you lies my master thesis entitled "Computational fluid dynamics in the stented arteria femoralis superficialis". I conducted this research to obtain my MSc title in Technical Medicine at the University of Twente. Thirteen months ago I started my graduation internship at the department of vascular surgery at Rijnstate. From the moment I started this internship, I knew I was going to face some challenges as computational fluid dynamics was completely new to me. I did not know if I was any good, but I could not resist this great opportunity to learn. Now, at the end of my graduation internship, I am proud to say that I have overcome many obstacles, but this would not have been possible without the support of others.

First of all I would like to thank my supervisors for their guidance and support. During the past year you provided me the space to grow, which I really appreciated. Michel, thank you for your clinical input in this rather technical research and the important lesson you taught me: "Expectations are realistic as long as you keep adjusting them". Rob, thank you for being approachable and kind. I never had the feeling that I could ask a stupid question. Paul, thank you for your guidance during the past two years. I did not always like your hard questions, but they payed off. Lennart, thank you for always being their to answer my questions and discuss my results. I highly appreciated your detailed feedback.

Furthermore, I would like to thank all the interns from the 'Rijnstage' group for all the coffee breaks, laughs and feedback moments. Special thanks to Anne-Jet, Cindy and Tim who were always there for me if I needed to talk, discuss or laugh. I am really going to miss our trips to Dadawan. Moreover, I would like to thank all the researchers for making me feel at home and all the vascular surgeons for helping me in my clinical development. Beau, Merle and Cindy, thank you for listening and helping me grow.

Finally, I would like to thank my parents and Michael. You were always there to support me, encourage me and help me see the positive side of everything

I encountered. Without you, I would not be where I am today and for that I am eternally grateful.

Lisa
May, 2020

Contents

List of abbreviations	vii
0 Introduction	1
1 Clinical background	3
1.1 Peripheral arterial disease	3
1.2 Atherosclerosis	5
1.3 Arterial hemodynamics	6
1.4 Obtaining wall shear stress	9
2 Computational fluid dynamics	11
2.1 Introduction	11
2.2 Preprocessing	11
2.3 CFD solver	22
2.4 Postprocessing	23
2.5 Simulation error	23
3 Blooming artifact: an in-vitro study	25
3.1 Introduction	25
3.2 Methods	27
3.3 Results	32
3.4 Discussion	41
3.5 Conclusion	47
4 Uncertainty quantification	49
4.1 Introduction	49
4.2 Method	50
4.3 Results	57
4.4 Discussion	70
4.5 Conclusion	74
5 Future perspectives	77

6 Conclusion	79
Bibliography	81
A Velocity profile based on echo PIV measurements	89
A.1 Longitudinal to axial echo PIV velocity profile	90
A.2 Echo PIV fitted to grid SimVascular	90
A.3 2D to 3D velocity profile	93
A.4 Smoothing	93
B Uncertainty in patient-specific geometry	95
B.1 Standard simulation of patient 1	96
B.2 Case S1	98
B.3 Case S2	100
B.4 Case S3	102
B.5 Case S4	104
C Uncertainty in inlet velocity profile	107
C.1 Womersley with DUS based flow rate	108
C.2 Womersley with echo PIV based flow rate	110
C.3 Echo PIV with echo PIV based flow rate	112

List of abbreviations

ABI	Ankle-brachial index
AFC	Arteria femoralis communis
AFP	Arteria femoralis profunda
AFS	Arteria femoralis superficialis
CFD	Computational fluid dynamics
CNR	Contrast-to-noise ratio
CTA	Computed tomography angiography
DSA	Digital subtraction angiography
DUS	Duplex ultrasound
FWHM	Full width at half maximum
HU	Hounsfield Units
IMR	Iterative model reconstruction
MRA	Magnetic resonance angiography
OCT	Optical coherence tomography
PAD	Peripheral arterial disease
PC-MRI	Phase-contrast magnetic resonance imaging
PIV	Particle image velocimetry
PVL	Percentage visible lumen
SNR	Signal-to-noise ratio
TAWSS	Time-averaged wall shear stress
WSS	Wall shear stress

Introduction

Peripheral arterial disease (PAD) is a severe clinical problem with an increasing incidence rate as a result of an ageing population. [1] PAD affects three to ten percent of the population in the age range of 40-59 years and the prevalence increases to 20% above 70 years of age. [2, 3] Symptoms of PAD vary from pain or cramping in the leg during exercise, which is relieved by rest, to critical limb ischemia, that could eventually require limb amputation. [4, 5] PAD in the *arteria femoralis superficialis* (AFS) is the most common cause of symptomatic PAD. When medical and exercise therapy are unsuccessful and the symptoms are still disabling, revascularization is indicated. Due to innovations in stent design and revascularization techniques, stent placement is now the recommended treatment in lesions with a total length of <25 cm. [5–7] However, in about 20% of the patients an in-stent restenosis occurs within one-year after treatment and a subsequent reintervention is needed. [8, 9]

The formation of a stenosis is caused by a chronic disease of the vessel wall called atherosclerosis. [10] Atherosclerosis is induced by both systemic risk factors, including smoking, hypertension and hyperlipidaemia, and the local arterial microenvironment. [11] Current therapies focus on reducing systemic risk factors through medication, thereby preventing global progression of atherosclerosis. Local progression of atherosclerosis, as is seen near bifurcations and branches, could be explained by the local arterial microenvironment. [11, 12] Near bifurcations and branches, the blood flow is disturbed due to flow separation, inducing changes in flow direction and less-organized zones of flow recirculation. The resulting low shear stresses cause the endothelium to become more susceptible to atherosclerosis. [13] As flow dynamics are involved in the local progression of atherosclerosis, being able to visualize the blood flow could provide a better understanding and improved prediction of stent failure.

Current clinically available techniques are unable or very limited in visualizing these complex alterations in blood flow in patients. [14–18] Complex

blood flow could, however, be simulated using computational fluid dynamics (CFD). [19] From these simulations, non-measurable flow parameters in patients could be derived. Furthermore, it is possible to simulate changes due to a treatment, for instance the placement of a stent, and analyze the effect of the treatment on the blood flow. CFD could, therefore, change the endovascular treatment planning and follow-up from a general treatment to a personalized treatment. However, for clinically feasible CFD simulations, modelling simplifications and assumptions are unavoidable. [19] On the one hand, simplifications are needed to reduce the complexity of the computational model. On the other hand, simplifications are necessary due to not having all (adequate) patient-specific data needed as input to the CFD model. These simplifications influence the accuracy of the CFD model. To be able to use CFD in a clinical workflow, the accuracy of the CFD model needs to be sufficient to be predictive for the clinical outcome. Therefore, the aim of this thesis is to analyze the effect of CFD input parameters on the CFD solution in the stented AFS.

The outline of the thesis is as follows. In **Chapter 1** the clinical background on PAD, atherosclerosis, arterial hemodynamics and current imaging modalities are presented. **Chapter 2** elaborates on the CFD simulation process and the choices in inputs to the CFD model that can be made in the different phases of the CFD simulation. As the blooming artifact in the used scans resulted in a large uncertainty in the obtained geometry used in the CFD simulation, the effect of the blooming artifact on the segmented arterial lumen is researched in an in-vitro study in **Chapter 3**. In **Chapter 4** the influence of uncertainty in the geometry and inlet boundary condition on the CFD solution is analyzed by performing uncertainty analysis. **Chapter 5** discusses future perspectives based on this study and in **Chapter 6** the most important findings of this study are summarized and an overall conclusion is presented.

Clinical background 1

1.1 Peripheral arterial disease

PAD, a disorder defined by a stenosis in medium-sized and large arteries, except for the coronary and cerebral arteries, is a common age-related condition. [2,20,21] PAD affects 3% to 10% of the population in the age range 40 to 59 years and the prevalence increases to 20% above 70 years of age. [2,3] Risk factors for PAD include smoking, hypertension, hyperlipidaemia, diabetes mellitus, obesity and family history. [21] The AFS is a common anatomical site for a stenosis or occlusion and this is the most common cause of symptomatic PAD. [3–5] Intermittent claudication, pain or cramping in the muscles of the lower extremities that is induced by exercise and relieved by rest, is often the first symptom of PAD. [4,5] In a further stage, PAD could result in chronic or critical limb ischaemia that eventually requires limb amputation. [4] Based on the patient's symptoms, the patient is classified using the Fontaine classification or Rutherford classification, shown in Table 1.1. [6]

PAD is initially diagnosed using the ankle-brachial index (ABI). [21] The ABI is calculated by dividing the systolic blood pressure measured at the *arteria dorsalis pedis* or *arteria tibialis posterior* (ankle) by the systolic blood pressure measured at the *arteria brachialis* (arm). An ABI <0.9 indicates PAD, which could be divided into mild PAD (ABI 0.7-0.9), moderate PAD (ABI 0.5-0.7) and severe PAD (ABI <0.5). Although ABI is a relatively simple and reliable method to diagnose PAD, the ABI is less sensitive in patients with diabetes mellitus or chronic kidney disease. [21–23] Due to the higher presence of medial artery calcification in these diseases, the arterial compliance in the ankle arteries is reduced. Therefore, a falsely elevated systolic blood pressure could be measured at the ankle, resulting in an unreliable high ABI value. In these patients, a blood pressure measurement at the toe instead of at the ankle is performed. [23]

For all patients diagnosed with PAD, modification of risk factors is recommended, since they have a two to threefold increased risk of cardiovascular

Table 1.1: Classification of peripheral arterial disease according to the Fontaine classification and Rutherford classification. IC = intermittent claudication. [6]

Fontaine classification		Rutherford classification		
Stage	Symptoms	Grade	Category	Symptoms
I	Asymptomatic	0	0	Asymptomatic
IIa	IC >200 m walking distance	I	1	Mild IC
IIb	IC <200 m walking distance	I	2	Moderate IC
III	Ischemic rest pain	I	3	Severe IC
		II	4	Ischemic rest pain
IV	Ulceration/gangrene	III	5	Minor tissue loss
		III	6	Major tissue loss

events. [6, 21, 23, 24] Medical therapy focuses on control of lipid and glucose, the normalization of blood pressure, preventing platelet aggregation and inhibiting thrombus formation. [21] Supervised exercise programs are advised to patients suffering from IC. Exercise therapy could result in an increased pain-free walking distance by improving the skeletal muscle metabolism, endothelial function and gait biomechanics, thereby increasing the quality of life of these patients. [23] Furthermore, for all patients smoking cessation is highly recommended, since continued smoking counteracts the positive effects of medical and exercise therapy and increases the risk of cerebral and cardiac events. [21] If the symptoms are still disabling after medical and exercise therapy or if the patient is classified as Fontaine III or IV, revascularization is indicated.

To choose the right revascularization technique, first the location and severity of the vascular lesion need to be identified. [6] This could be achieved using imaging techniques including duplex ultrasound (DUS), computed tomography angiography (CTA), magnetic resonance angiography (MRA) and digital subtraction angiography (DSA). DUS combines B-mode echography and Doppler to identify vascular lesions and determine its hemodynamic severity. [6] It is often the first choice imaging technique, since it is easy to use, inexpensive, non-invasive, real time and is able to measure haemodynamics. In case exact anatomy for endovascular stent placement is desired, other imag-

ing techniques are required. [5,6] CTA and MRA are usually chosen over DSA since they are fast, non-invasive, available in most clinics and have a high resolution. CTA, MRA and DSA all provide information about lesion location, its severity and upstream and downstream status, necessary to determine the right revascularization technique. [6]

For complex lesions in the femoropopliteal tract, open surgical revascularization was the gold standard technique for decades. [25,26] Due to innovations in stent design and endovascular revascularization techniques, endovascular intervention is now recommended in more complex lesions (total length <25 cm). [5-7] In simple and short lesions (<3 cm) plain balloon angioplasty is performed, while in intermediate-length lesions stents are typically placed, because plain balloon angioplasty alone is in these lesions most often not a long-lasting solution. [25] In the AFS, it was shown that endovascular intervention has lower mortality and morbidity rates, a lower risk, an improved quality of life, a faster recovery and similar patency rates at one year follow-up compared to an open surgical femoropopliteal bypass. [8,23,25] Despite improvements in endovascular techniques and stents, in-stent restenosis still occurs in 13-20% of the patients at 1-year follow-up after endovascular intervention in the AFS. [8,9,27] This percentage is much higher in the AFS than in other vascular beds and results in more reinterventions in the AFS. [9]

1.2 Atherosclerosis

The formation of a stenosis is caused by a chronic disease of the vessel wall called atherosclerosis in which atherogenesis, the formation of atheromatous plaques, is stimulated. The arterial wall consists of three layers: the tunica intima (inner layer), the tunica media and the tunica adventitia (outer layer), all shown in Figure 1.1. [10] In healthy conditions, the tunica intima consists of a monolayer epithelial cells, called the endothelium, which are exposed to the circulating blood. The tunica media mainly contains smooth muscle cells and the tunica adventitia is composed of supportive tissue. Normally, the vessel wall is vasoprotective, which means that the endothelium resists the attachment of leukocytes circulating in blood. However, stimuli including dyslipidaemia can activate the endothelium. As a result, the vessel wall becomes more susceptible to the formation of a stenosis. [10]

The progression of atherosclerosis could be divided into three phases, visualized in Figure 1.1. During the first phase, the endothelial cells is activated, which results in the expression of adhesion molecules on the endothelium and the binding of leukocytes. These leukocytes migrate into the intima,

where monocytes can subsequently develop into macrophages, collect lipids and become foam cells. In Figure 1.1 this is shown at ‘Endothelial dysfunction’ and ‘Lipid accumulation’. The second phase is characterized by migration of smooth muscle cells from the tunica media to the tunica intima, proliferation of the smooth muscle cells and production of extracellular matrix molecules including collagen and elastin, shown at ‘Non-calcified plaque’ in Figure 1.1. In some cases, the atherosclerotic plaque ruptures due to a necrotic core, which results in thrombosis. This is the third phase of atherosclerosis and shown in Figure 1.1 at ‘Plaque rupture’. [10]

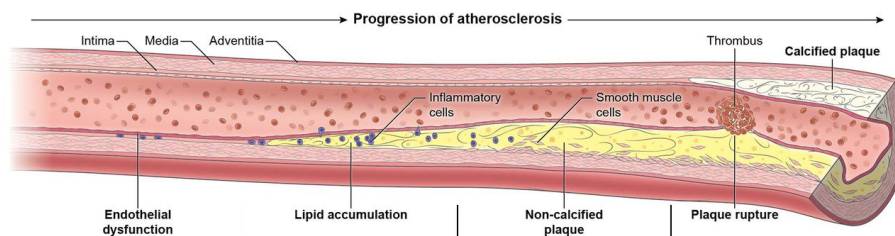


Figure 1.1: The progression of atherosclerosis in three phases. During the first phase (lipid accumulation) the endothelial cells are activated, adhesion molecules expressed, leukocytes migrated into the intima and macrophages developed into foam cells. In the second phase (non-calcified plaque) smooth muscle cells migrate from the tunica media to the tunica intima. During the third phase (plaque rupture) the plaque ruptures and results in thrombosis. [28]

Atherosclerosis is induced by both systemic risk factors (risk factors for PAD) and the local arterial microenvironment. The local arterial microenvironment includes vessel mechanics, matrix composition, arterial hemodynamics and the local presence of soluble factors that maintain atherogenic inflammation. They all play an important role in cell function and thus in the development of atherosclerosis. Current therapies focus on reducing systemic risk factors through medication. Although it is shown that these therapies are successful in reducing cardiovascular events, they do not completely prevent the local progression of atherosclerosis, as is seen in the AFS. Local progression of atherosclerosis could, however, be explained by the arterial hemodynamics. [11]

1.3 Arterial hemodynamics

Every heart cycle, the heart pumps blood through the vascular system. This results in two stresses on the vascular wall: the circumferential stress and

the tangential stress. The circumferential stress is generated by the blood pressure and acts on all layers of the vascular wall. The tangential stress or wall shear stress (WSS) is generated by the flow of viscous blood and acts only on the endothelium. The WSS is defined as

$$\tau(y = 0) = \mu(\dot{\gamma}) \frac{\partial u}{\partial y} \quad (1.1)$$

with τ (shear stress) evaluated at $y = 0$ being the WSS, μ being the dynamic viscosity, $\dot{\gamma}$ being the shear rate, u being the velocity parallel to the wall and y being the radial distance to the wall. Endothelial cells sense the WSS through specialized mecha-nosensors and transform this information into intracellular biochemical signals. The WSS is, therefore, able to influence the endothelial function. [11,12]

The WSS depends on the dynamic blood flow, as it is the derivative of the velocity profile, according to Equation 1.1. In a unidirectional flow, the WSS is high (1 - 1.5 Pa). [13] This results in a vasoprotective phenotype of the endothelial cells, including an elevated nitric oxide production, a low endothelial turnover and limited proinflammatory gene expression. Even when systemic risk factors are present, vascular regions exposed to a high WSS show resistance to progression of atherosclerosis. Low WSS (<0.4 Pa), however, results in an atheroprone phenotype of the endothelial cells, also called endothelial activation, which is the first stage of atherosclerosis. [13] A low WSS can be found at bifurcations, curvatures and branches due to flow separation, changes in flow direction and areas of slow and recirculating flow. Therefore, atherosclerotic plaques tend to form at these locations, as is shown in Figure 1.2. [11,12]

In the AFS, however, 60% to 70% of the stenoses/occlusions occur in the adductor region, a straight and unbranched site, shown in Figure 1.3. [29] Blair et al. (1990) [30] showed that the adductor canal segment of the AFS is not more prone to progression of atherosclerosis than the proximal AFS based on anatomy, as would be expected. It was discovered, however, that adaptive arterial enlargement in the adductor canal was limited. In the proximal AFS an increase in intimal thickening results in a similar increase in artery size, thereby maintaining the normal lumen caliber. Since the space available for adaptive arterial enlargement is limited in the confined adductor canal, see Figure 1.3B, intimal thickening more readily leads to luminal narrowing. This lumen stenosis disturbs the blood flow, thereby making the adductor canal segment of the AFS more susceptible to adverse consequences of atherosclerosis. [29,30]

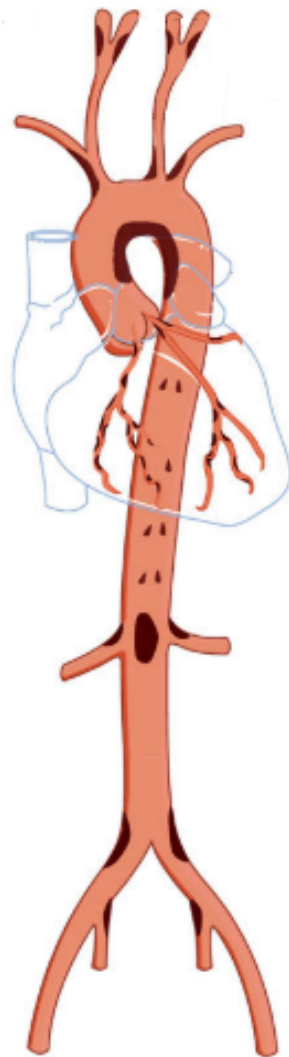


Figure 1.2: Locations in the arterial tree prone to atherosclerosis (shown in dark): curvatures, bifurcations and branches. [11]

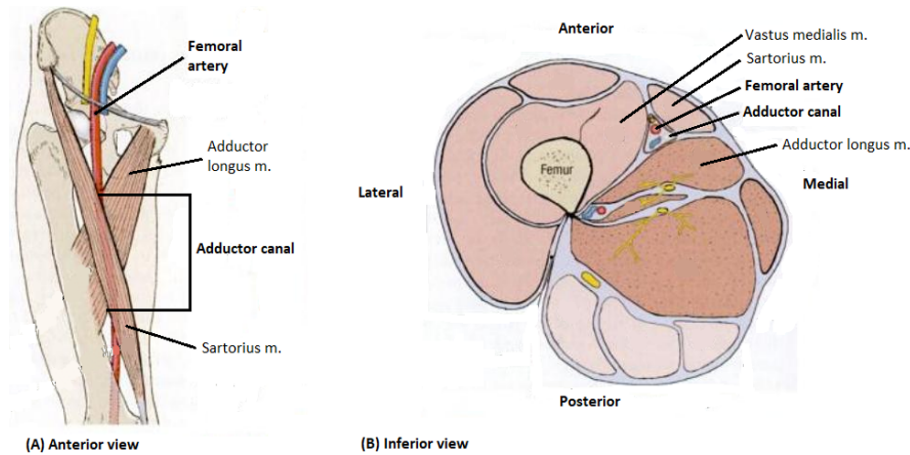


Figure 1.3: The femoral artery situated in the adductor canal. Reproduced from Tank, P.W. et al. (2009). [31]

1.4 Obtaining wall shear stress

A low WSS as a result of a disturbed blood flow could be a useful parameter in the prediction of progression of atherosclerosis or in-stent restenosis in the AFS. The WSS was already measured in-vitro using laser particle image velocimetry (PIV), but this technique cannot be used in-vivo as the patient's tissue is opaque. [32] In-vivo the WSS has been measured with phase-contrast magnetic resonance imaging (PC-MRI) and echo PIV. PC-MRI determines the volumetric flow from which the WSS is calculated, but it is time consuming, relatively expensive and has limited temporal and spatial resolution. [14–17] Ultrasound is seeing rapid developments for achieving vector flow quantification, as it has important advantages in time resolution and cost relative to PC-MRI. [18] Echo PIV is an ultrasound-based technique that, at present, can measure the 2D velocity field in-vivo and calculates the WSS in arterial geometries with high temporal and spatial resolution. [18, 33] Although echo PIV is a promising technique, the quality of the echo PIV measurement still depends on patient characteristics such as plaque composition and obesity. [33] Furthermore, echo PIV only provides a 2D velocity field, while with a 3D velocity field complex flow could be visualized and quantified. [18] Further improvements are necessary to be able to use echo PIV in clinical care. Another method to obtain the WSS is CFD. CFD is able to simulate the complex blood flow, calculate the WSS and analyze the effect of a treatment on the blood flow. [19] It could, therefore, change the endovascular treatment planning and follow-up from a general treatment to a personalized treatment. The CFD simulation process will be elaborated further in Chapter 2.

Computational fluid dynamics



2.1 Introduction

CFD is a field of fluid mechanics that uses numerical analysis to solve fluid problems and obtain simulations of complex flow fields. [34] CFD can be used in several disciplines. In biomedical research, CFD is often used to better understand blood flow dynamics using idealized models or to determine the blood flow in individual patients. To be able to use CFD in individual patients, the inputs of the CFD model need to be patient-specific to simulate the blood flow in patients accurately. Based on the arterial site and the available patient-specific data, several choices in the CFD simulation process can be made. Typically, a CFD simulation can be divided into three phases: preprocessing, solving and postprocessing. [34] In the preprocessing phase, the patient-specific geometry, mesh, boundary conditions and material properties are defined. During the solving phase, the solver settings, for example the number of time steps, time step size and number of iterations, are chosen and the actual simulation is performed. In the last phase, results, such as velocity vectors and the WSS, are visualized. In the following sections the phases of the CFD simulation including the possible choices, are elaborated further. [34]

2.2 Preprocessing

Patient-specific geometry

The first step in the preprocessing phase is the creation of a geometry corresponding to the physical domain in which the flow field will be computed. [34] The 3D patient-specific geometry can be obtained by segmentation of the arterial lumen, most often based on a CTA or MRA scan. Several segmentation techniques are available, which can be broadly classified as manual, semi-automatic and automatic segmentation. [35] Manual segmentation is time consuming and is typically characterized by a limited intra- and inter-operator repeatability and reproducibility. Since deviations in the segmentation affect the simulated blood flow, manual segmentation is less suitable in

a patient-specific CFD simulation. Semi-automatic and automatic segmentation techniques, including machine learning, deformable models and tracking methods, overcome the drawbacks of manual segmentation. [35] However, not one of these techniques is suitable for all possible applications of obtaining the optimal patient-specific geometry and the quality of the obtained segmentation can be severely hampered by noise or other artefacts. It is, therefore, needed to select the optimal segmentation technique based on the anatomical region of interest and the image quality of the used scan. [35]

The *level set method of implicit deformable models* is a semi-automatic segmentation technique that is well-suited for segmentation of complex geometries in both physiological and pathological conditions as they are flexible. [35,36] The segmentation technique focuses on automatic detection of the vessel wall, the user defines the region of interest and a few, easy to report, parameters, namely inflation, smoothing and advection. Since the blood flow only needs to be simulated in a subset of the blood vessels contained in the scan, the user-dependent definition of the region of interest is justified as long as realistic boundary conditions can be applied.

The first step in the *level set method of implicit deformable models*, is determining the initial level set function, for instance by colliding fronts initialization. The user identifies the vessel of interest by placing seed points at the desired start and end of the vessel in the scan, shown in Figure 2.3a as the green and red circles. From these two seed points, independent sound wavefronts propagate with a speed proportional to the local image intensity. As the image intensity decreases towards the vessel wall, the direction of the wave gradually changes and becomes perpendicular to the vessel wall at the lumen boundary. The initial surface is determined as the region between the two seed points where the two wavefronts move in opposite direction. Because of this method, tissue and side branches are excluded from the initial surface as the direction of the wavefronts is in concurrent orientation, shown in Figure 2.1. [36]

The second step in the segmentation technique is evolution of the level set function as a result of image and shape-based forces, called regularization. Regularization is typically required to obtain a smooth and representative final surface. In the regularization step, the amount of inflation, smoothing and advection towards sites with strong changes in image intensity, such as the vessel wall, are determined. In a high-contrast scan, using only the advection term could be sufficient as it shapes the surface to the ridges of the image gradient magnitude. However, smoothing is commonly necessary due

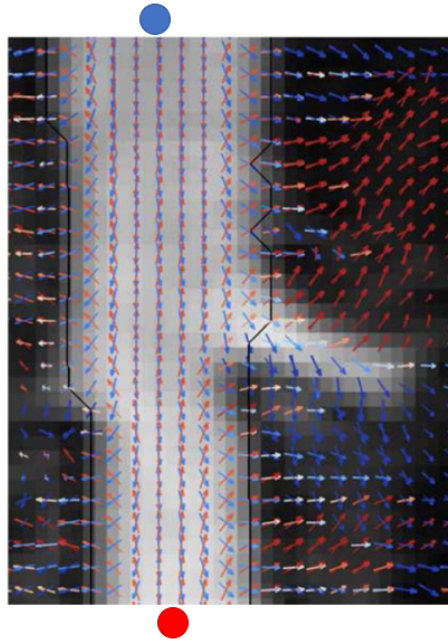


Figure 2.1: Close up of two independent wavefronts, originating from the blue and red seed point, showing opposite directions within the lumen and concurrent orientation at the lumen boundary and side branch. Reproduced from Antiga et al. (2018). [36]

to the combination of a small vessel diameter and insufficient image resolution. Smoothing could result in shrinkage of the surface, which could be compensated for by adjusting the inflation term. [36] In Figure 2.3b the final surface of the level set method of implicit deformable models is shown.

CTA scans could be affected by artifacts. An important artifact is the blooming artifact, caused by beam hardening and partial volume averaging. The blooming artifact causes high density objects, such as stent struts, to seem larger than they actually are, as will be explained further in Chapter 3. The blooming artifacts are most prominent at the proximal and distal radiopaque stent marker as can be seen in Figure 2.3a and b as the sharp, white dots below the segmentation. Since the colliding fronts initialization technique defines the vessel wall at sites with strong changes in image intensity, the vessel lumen is locally narrowed at the location of the proximal and distal stent marker. Therefore, proximal and distal stent markers could be segmented using another segmentation technique, called the *active tubes segmentation technique*. The *active tubes segmentation technique* forms an initial surface by plac-

ing seeds with a radius corresponding to the vessel lumen, called cylinder seed initialization, shown in Figure 2.3c. Regularization is then again used to obtain a smooth and final surface. With this method the lumen diameter at the site of the marker artifact can be estimated as an interpolation between upstream and downstream lumen segments. The result of the combined *level set method of implicit deformable models* and *active tubes segmentation technique* is shown in Figure 2.3d. The effect of the blooming artifact on the visible lumen diameter and the segmentation is elaborated further in Chapter 3.

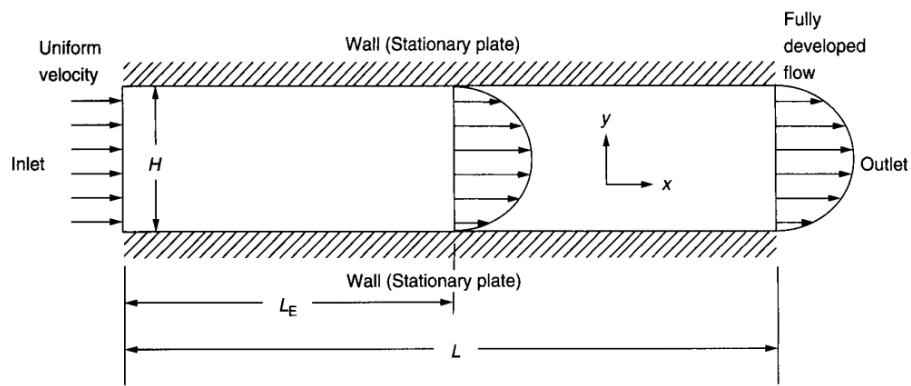


Figure 2.2: Evolution of the flow to a fully developed flow (Hagen-Poiseuille flow). H is the diameter of the vessel, L the length of the vessel and L_E the hydrodynamic entrance length. Reproduced from Tu et al. (2018). [34]

As a final step in the creation of a patient-specific geometry, the hydrodynamic entrance length needs to be taken into account. [34] The hydrodynamic entrance length is the length it takes for the flow to become fully developed. When the flow is fully developed, it is no longer influenced by effects arising from the entrance and flow properties, for example the velocity profile, could be solved. The Hagen-Poiseuille flow is the fully developed flow for steady, laminar flow, shown in Figure 2.2. A fully developed flow at the inlet and outlets of the CFD model is preferred to set realistic boundary conditions, as will be elaborated further in Section 2.2: Boundary conditions.

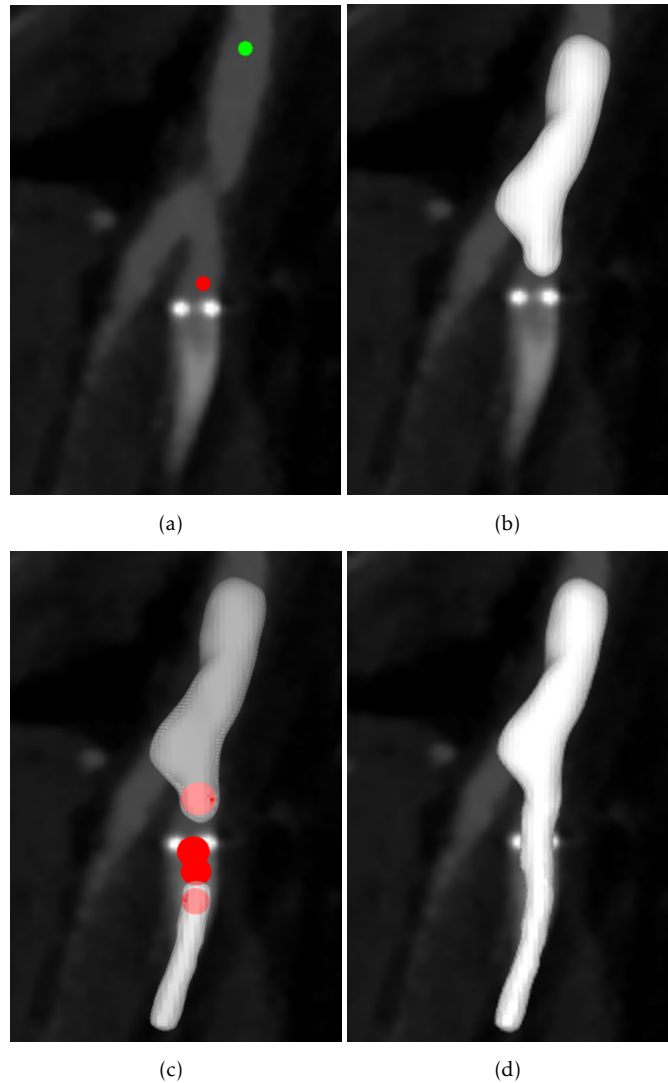


Figure 2.3: Segmentation of the femoral bifurcation. Top: *level set method of implicit deformable models*. Bottom: *active tubes segmentation technique*. (a) Identifying the vessel of interest by placing seeds points (green and red circle) at the desired start and end of the vessel. (b) The final surface obtained after evolution of the level set function. (c) Placing seeds with a radius corresponding to the vessel lumen. (d) The final segmentation, combining the *level set method of implicit deformable models* and *active tubes segmentation technique*.

Mesh

After segmentation of the arterial lumen, the obtained patient-specific geometry needs to be subdivided into a number of smaller, nonoverlapping subdomains. This is done by generating a mesh overlaying the whole geometry. Mesh types can be subdivided into structured and unstructured meshes. A structured mesh contains square-shaped elements in a regular topological pattern. Due to its regular connection to neighbouring elements, the memory storage and connectivity information is efficient and hierarchical, which results in a fast computational time. An unstructured mesh is more flexible than the structured mesh, since it allows tetrahedrals. However, the connection of each element to its neighbours needs to be explicitly stored in the unstructured mesh, as the connection differs for every used element. Computations that use an unstructured mesh are, therefore, longer. A structured mesh is, in general, more accurate than an unstructured mesh. However, similar levels of accuracy could be achieved with an unstructured mesh at the cost of longer computational time, but with a typically reduced segmentation time. [34] Commonly used elements in the mesh are shown in Figure 2.4. [37,38]

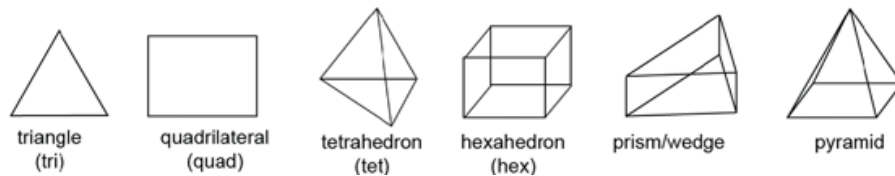


Figure 2.4: Possible elements used in the generation of a mesh. In 2D, the triangle and quadrilateral could be used. In 3D the tetrahedron, hexahedron, prism and pyramid could be chosen. Two tetrahedrons form a pyramid and three tetrahedrons form a prism. [37]

Boundary conditions

After obtaining the patient-specific geometry and the mesh, the effect of the excluded sections of the cardiovascular system on the geometry in question need to be defined by setting boundary conditions. These boundary conditions include the inlet, outlet and the wall of the obtained patient-specific geometry. Realistic boundary conditions are a core component of a CFD simulation, as the CFD outcome is fully determined by the geometry and the applied boundary conditions. [39,40] In the following subsections, the inlet, outlet and wall boundary conditions will be elaborated.

Inlet

The inlet boundary condition is a crucial part of the CFD simulation as it typically governs the flow rate through the model. [40] As the flow field solution will be heavily dependent on the flow rate through the domain, a patient-individualized inlet boundary condition is key for a patient-specific CFD simulation. For the inlet boundary condition, a pressure waveform or a velocity field could be chosen. The pressure waveform is most often not available since it can only be obtained accurately using invasive techniques. The patient-specific velocity field could be derived from a PC-MRI and DUS measurement. Since PC-MRI is often not available and/or very costly in most clinics, DUS is most often used.

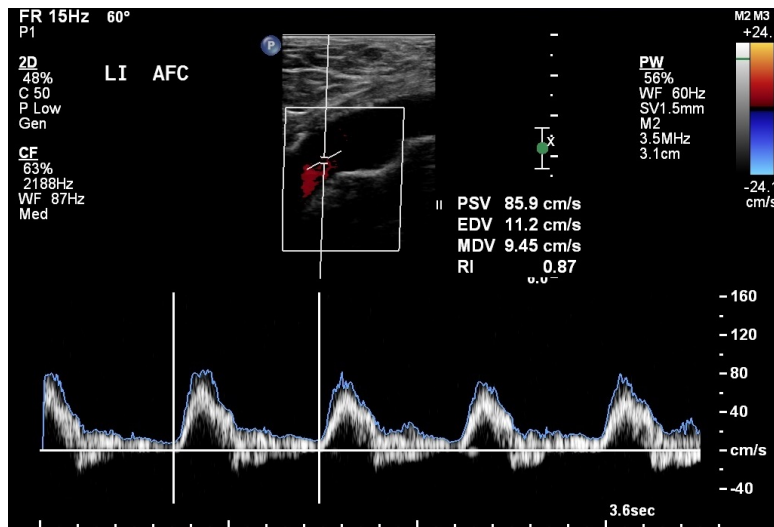


Figure 2.5: Duplex ultrasound measurement in the left *arteria femoralis communis* (AFC). The real-time velocity at the centerline of the vessel is measured.

During a DUS measurement, the real-time velocity at the centerline of the blood vessel is measured, as is shown in Figure 2.5. Since blood flow is pulsatile, the flow rate could be calculated from the velocity through Womersley's theory. [41] This calculation assumes that the inlet flow is fully developed, meaning that the flow is not influenced by effects arising from, for example, a bifurcation. This could be achieved in the segmentation step by taking into account the hydrodynamic entrance length, as mentioned before. The vessel of interest is, however, not always long enough for the flow to become fully developed and this assumption is, therefore, not always met. The calculation of the flow rate using Womersley's theory is shown below. [41]

$$Q(t) = \sum_{k=0}^{\infty} \hat{Q}_k \cdot \exp(ik\omega t) \quad (2.1)$$

In which Q is the volumetric flow rate and \hat{Q} its Fourier coefficients, calculated by

$$\hat{Q}_k = \pi R^2 \hat{u}_k \frac{J_0(i^{3/2}\alpha_k) - \frac{2}{i^{3/2}\alpha_k} J_1(i^{3/2}\alpha_k)}{i^{3/2}\alpha_k - 1} \quad (2.2)$$

In which R is the vessel radius, \hat{u} the Fourier coefficients of the centerline velocity, J_x the Bessel-function of the x -th order and α_k the frequency-dependent Womersley parameter, given by

$$\alpha_k = R \sqrt{\frac{k \cdot \rho \omega}{\mu}} \quad (2.3)$$

In which ρ is the density and μ the dynamic viscosity of blood.

Based on the calculated flow rate, the velocity profile at the inlet could be calculated using a blunt, parabolic or Womersley velocity profile. The optimal velocity profile depends on the flow conditions upstream. [42]

Although the velocity profiles mentioned above could be used as inlet boundary condition, they are still an estimation of the patient's true velocity profile. A relatively new technique to obtain the velocity profile in patients using ultrasound, is high frame rate contrast enhanced PIV, or in short echo PIV. [43] PIV analysis focuses on tracking small groups of particles in subregions of the captured image. By calculating the cross-correlation for each possible displacement, the most likely displacement is found. PIV can be combined with high frame-rate ultrasound imaging and contrast-enhancing microbubbles to visualize the blood flow in patients. By tracking the microbubbles, calculating the cross-correlation and finding the most likely displacement, velocity vectors could be obtained. Although obtaining the velocity profile using echo PIV seems like a promising technique, it still needs to be validated in patients. [43] Furthermore, echo PIV obtains 2D velocity fields, while for CFD 3D velocity fields are necessary. Simplifications are needed to convert these 2D vector fields to 3D vector fields, as will be elaborated further in Chapter 4.

Outlet

The outlet boundary condition represents the influence of the downstream vasculature on the CFD domain. Together with the inlet boundary condition, the outlet boundary condition typically determines the flow rate distribution

throughout the domain. [44] Several boundary conditions could be used for the outlet, including zero pressure, a patient-specific pressure or velocity profile and a Windkessel model. [39] However, not all boundary conditions are as accurate or practical. The zero pressure boundary condition is the simplest boundary condition. It is, however, generally less accurate in geometries containing bifurcations, as the zero boundary condition assumes that the microcirculation in both branches is identical. A patient-specific pressure or velocity profile is more accurate than the zero pressure boundary condition, but the pressure profile is hard to acquire and the velocity profile could cause an ill-posed problem. [45] As the pressure or velocity profile is different for every patient, using a generalized pressure or velocity profile would induce a bias.

A popular outlet boundary condition is the Windkessel model. [39] The Windkessel model is a compact and powerful model that, with only 3 elements, is often able to accurately reproduce a measured flow rate profile at the outlet. The 3-element Windkessel model relates the outflow pressure (P_d) and the flow rate (Q) through an electric circuit analogue, shown in Figure 2.6. [46] The capacitance (C) simulates the wall compliance, and the proximal (R_p) and distal (R_d) resistances mimic the viscous resistance that the blood flow undergoes in vessels. [46]

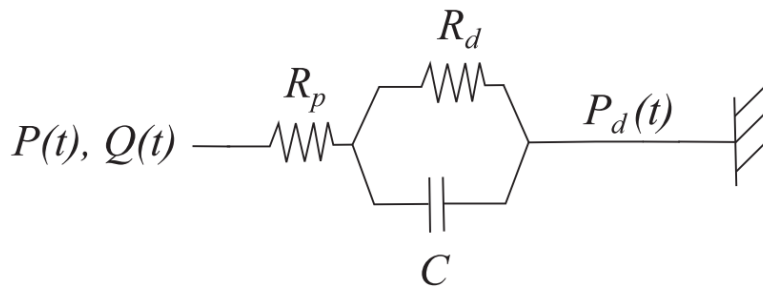


Figure 2.6: 3-element Windkessel model relating the outflow pressure (P_d) and the flow rate (Q) through an electric analogue. The capacitance (C) simulates the wall compliance, and the proximal (R_p) and distal (R_d) resistances mimic the viscous resistance that the blood flow undergoes in vessels. [46]

The values of C , R_p and R_d are modeled quantities that preferentially can be estimated from clinical measurement data. To estimate patient-specific values of these elements accurately, the flow rates, based on the velocities measured with DUS could be used. The first step is to calculate the total resistance (R_t), the sum of R_p and R_d , in the outlets using the mean pressure (\bar{P}) and the mean flow rate (\bar{Q}).

$$R_t = \frac{\bar{P}}{\bar{Q}} \quad (2.4)$$

The second step is to calculate the R_p for the outlets using the measured R_p values for different segments of the artery, obtained by Westerhof et al (1969). [47] The third step is to calculate R_d using the values for R_t and R_p . Then, the total capacitance (C) is calculated through:

$$C = \frac{V_{in}}{\Delta P} \quad (2.5)$$

in which V_{in} is the inflow volume during systole and ΔP is the pulse pressure. Finally the individual contribution of the outlet compliances is tuned to match the measured outlet flow rate profiles in the model. The obtained values of C , R_p and R_d for the outlets are then known and can be used for the Windkessel model.

Wall

For the wall there are two options for the boundary condition: including wall motion and dismissing wall motion. [48,49] Neglecting wall motion, also called a rigid wall, mimics a heavily calcified vessel and is the simplest wall boundary condition as only the vessel lumen needs to be segmented and discretized. This option is quick, but it does not take into account the interaction between blood and the vessel wall. Including wall motion does include the interaction between blood and the vessel wall and the simulations are, therefore, more realistic. However, the vessel lumen and vessel wall need to be segmented individually. Furthermore, the computational time of the model simulating the interaction between the vessel wall and the arterial lumen is much longer than the computational time of the rigid wall model. Comparing both wall boundary conditions shows that the two options have a good agreement in the WSS distribution for the arterial wall. [48,49]

Material properties

To complete the CFD model, material properties need to be defined for blood. When assuming the vessel wall to be rigid, the material properties of the vessel wall are irrelevant. For the material properties of blood, the blood viscosity and blood density need to be defined.

Blood viscosity

Blood is a non-Newtonian fluid with shear-thinning behaviour due to red blood cells. [37] This implies that the viscosity of blood changes under different conditions of shear rate. An increased shear rate occurs in high velocities

in the blood vessel. This causes red blood cells to move towards the center of the blood vessel and orient in the flow direction, reducing the viscosity of blood. For low velocities, the red blood cells are more evenly distributed throughout the blood vessel, increasing the viscosity of blood. [37]

The viscosity of blood is also influenced by the vessel diameter due to shear stresses caused by the vessel wall. [50] In small vessels, 3-8 μm , the diameter of the vessel is similar to the size of red blood cells. This causes the viscosity to increase. In larger vessels, 10-1000 μm , the red blood cells move towards the center of the vessel, leaving the plasma to remain close to the wall. This reduces the blood viscosity and the effect is called the "Fahraeus-Lindquist effect". In large blood vessels, in the order of mm, the effect of shear stresses on red blood cells do not introduce significant non-linear effects and the viscosity is constant in most of the domain. In this case, blood can be considered as a homogeneous fluid with Newtonian properties. In Figure 2.7 the effect of the vessel diameter on the viscosity of blood is shown. [50]

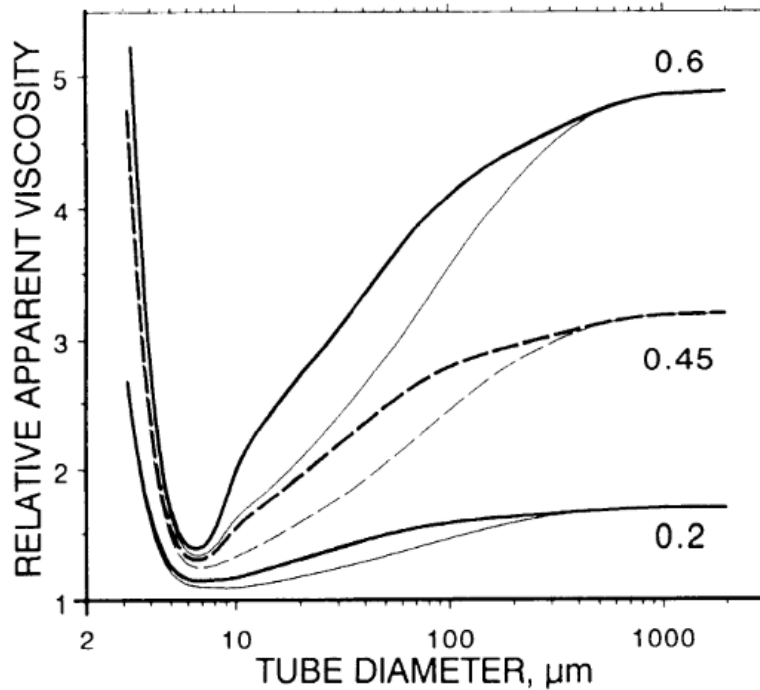


Figure 2.7: Viscosity as a function of the tube diameter. For larger diameters, in the order of mm, the effect of the diameter on the viscosity is constant. [50]

The effect of modelling Newtonian or a non-Newtonian blood on the WSS in large arteries (in the order of mm) has been researched. It was found that the WSS distribution was similar for Newtonian and non-Newtonian blood, but that the WSS magnitude differed 5-10% between the two. This difference in magnitude is smaller than the effect of geometry and boundary conditions on the WSS magnitude. [51]

As a blood viscosity measurement is not part of clinical care and calculation of the viscosity is a good estimation, the dynamic viscosity (μ_{blood}) can be calculated by

$$\mu_{blood} = \mu_{plasma}(1 + 2.5\epsilon + 6.2\epsilon^2) \quad (2.6)$$

in which μ_{plasma} is the viscosity of blood plasma (1.2 mPa.s) and ϵ is hematocrit, a value between 0 and 1. [52] For healthy subjects, hematocrit is in the range of 0.41 - 0.51 for men and 0.36 - 0.47 for women.

Blood density

The density of blood depends on the volume of red blood cells in blood and is approximately 1060 kg/m³ at 37 °C. [37] The density of a fluid is normally influenced by temperature and pressure. However, for liquids in general this effect is small, and for blood the temperature change is minimal, and thus the density is often assumed to be constant. [37]

2.3 CFD solver

After describing the CFD model and the blood properties, the Navier-Stokes equations can be solved. [19] The Navier-Stokes equation for incompressible, Newtonian blood is given by

$$\begin{aligned} \rho \left[\frac{\partial \mathbf{v}}{\partial t} + (\mathbf{v} \cdot \nabla) \mathbf{v} \right] &= \rho \mathbf{g} - \nabla p + \mu \nabla^2 \mathbf{v} \\ \nabla \cdot \mathbf{v} &= 0 \end{aligned} \quad (2.7)$$

in which ρ is the density of blood, v is the velocity of blood, t the time, μ the dynamic viscosity of blood, p the pressure and g the external body force. The first equation is the conservation of momentum and the second equation the conservation of mass. The Navier-Stokes equations need to be discretized to be applied to the mesh points in the CFD model. [37] For the discretization, three methods can be used: the finite difference method, the finite volume

method and the finite element method. The finite difference method is the easiest method. It solves the differential form of the Navier-Stokes equation, but is limited to a structured mesh. Since in arteries an unstructured mesh is most often used, the finite volume method and finite element method are more suitable for this application. [37]

2.4 Postprocessing

After solving the CFD model, the results could be visualized. The most common parameters used to analyze the CFD results, are the velocity profile, the WSS and the time-averaged WSS (TAWSS). Paraview (Kitware, Clifton Park, NY, USA) and Tecplot (Tecplot, Bellevue, WA, USA) could be used to visualize these results. They are able to visualize instantaneous streamlines of the velocity. Derived from the velocity, the WSS and TAWSS could be calculated, showing the magnitude and distribution of the WSS and TAWSS.

2.5 Simulation error

In the previous sections, the accuracy of the CFD simulation was mentioned. Since the CFD simulation is an approximation of reality, errors in the simulation are present. These errors include a numerical error, discretization error and modelling error. The numerical error is introduced by the computation as the data is represented as numbers of finite precision. The numerical error can be reduced by using a stabilized solver and a sufficient number of non-linear iterations and is usually smaller than the discretization and modelling error. [53]

The discretization error is the result of discretizing the geometry into small subdomains, the mesh. The size of the elements of the mesh influences the accuracy of the CFD simulation. Reducing the discretization error can be done by increasing the number of elements in the mesh until the mesh has reached convergence. Convergence has been reached when the difference of the parameter of interest between a mesh and a finer mesh is below a certain threshold. This threshold depends on the parameter of interest and the research question. [53]

The modelling error is introduced by the model and the input measurements, and can be improved by improving the model or increasing the accuracy of input measurements. [53] However, for patient-specific models, it is not always possible to improve the model, since not all patient-specific data is available. The main cause of errors in the CFD simulation are thus the result of mod-

elling errors, including segmentation, boundary conditions and blood properties. In Chapter 4 the effect of uncertainty in these parameters on the CFD simulation, will be investigated.

Blooming artifact: an in-vitro study



3.1 Introduction

CTA is a commonly used imaging technique in the diagnosis and treatment planning of PAD and is often used for the segmentation of blood vessels to obtain a patient-specific geometry. During a CT scan, X-ray is transmitted through and attenuated by the patient, and eventually measured by detectors. [54] The resulting CT image is composed of voxels containing the value of the average X-ray attenuation within the voxel, measured in 'Hounsfield Units' (HU). [55] Since different tissues attenuate the X-ray differently, it is possible to distinguish these tissues in the CT image. A CTA scan is performed to visualize the blood vessels. An iodine contrast agent is administered intravenously to the patient to increase the attenuation value of the vessel lumen. [55,56] The resulting attenuation value is in the range of 200 - 600 HU, while the attenuation value of the surrounding tissue, except for bone, is around 100 HU. [55] Thus, administration of the contrast agent results in a bigger contrast between the vessel lumen and the surrounding tissue and thus, in better visualization of blood vessels.

A quantitative evaluation of CTA images of vessels containing stents, however, is still hard due to artifacts. [57] The most important artifact is blooming, which describes an effect where the stent strut appears to be larger than it actually is, causing an underestimation of the vessel lumen. [58] The blooming artifact could be the result of partial volume averaging and beam hardening. Partial volume averaging could result in blooming since all different attenuation values within a voxel are averaged. High-density objects (stent struts), resulting in high attenuation values, dominate the attenuation value inside the voxel and in neighbouring voxels, resulting in exaggeration of the size of the stent strut. [57] Beam hardening arises when the polychromatic X-ray beam passes through a high-density object causing the lower energy photons of the beam to be absorbed more rapidly. [58] The resulting beam measured by the detectors, contains more higher energy photons than the original beam, which corresponds to a lower attenuation than that would have been measured by a

non-hardened beam. The beam hardening artifact near the edges of an object is smaller than in the center of an object, since the path is smaller. This causes the edges of the object to look brighter and the center of the object to look darker when compared to a non-hardened beam. The higher attenuation values at the edges of stent struts due to beam hardening combined with partial volume averaging cause the stent struts to seem larger than they actually are. As a result, the vessel lumen seems smaller than it actually is.

The effect of the blooming artifact on lumen visibility caused by stents in peripheral arteries has already been investigated in-vitro. [59–61] Kaempf et al. (2012) [60] found that the visible lumen diameter of two frequently used stents in the AFS, the Viabahn and Everflex stent, was 83.3% and 78.6%, respectively. [60] However, these results do not include the lumen visibility when proximal and distal radiopaque stent markers are used. For an Astron stent it was shown that the lumen visibility was 68.3% at the proximal and distal radiopaque stent marker compared to a lumen visibility of 81.2% at stent areas without these markers. [60] Furthermore, the blooming artifact of stent-in-stent placement, a frequently used technique in the AFS, was not investigated. It is known that the blooming artifact is more pronounced in stent-in-stent placement, but the exact effect is still unknown. [58]

Detector-based spectral CT

The attenuation of a X-ray beam (μ) consists of two components: attenuation by Compton scattering (μ_c) and attenuation by photoelectric absorption (μ_p), as is shown in Equation 3.1.

$$\begin{aligned}\mu(x, y, z, E) &= \mu_p(x, y, z, E) + \mu_c(x, y, z, E) = \alpha_p(x, y, z)f_p(E) + \alpha_c(x, y, z)f_c(E) \\ \alpha_p &= \rho Z^{3.8} \\ \alpha_c &= \rho Z\end{aligned}\tag{3.1}$$

With α_x being the characteristic coefficient of the material for photoelectric absorption and Compton scattering, $f_x(E)$ the energy dependency of photoelectric absorption and Compton scattering, ρ the mass density of the material and Z the atomic number. $f_p(E)$ and $f_c(E)$ are universal energy functions which do not depend on the material. α_c and α_p do depend on the material and are normally unknown. [62]

α_c and α_p could be obtained by using detector-based spectral CT. The detector-based spectral CT contains one X-ray tube and two layers of detectors. [63]

The top detector layer absorbs the low-energy photons and the bottom detector layer the high-energy photons. α_c and α_p could be calculated by solving Equation 3.1 for the high and low energies:

$$\begin{aligned}\mu(E_{low}) &= \alpha_p f_p(E_{low}) + \alpha_c f_c(E_{low}) \\ \mu(E_{high}) &= \alpha_p f_p(E_{high}) + \alpha_c f_c(E_{high})\end{aligned}\tag{3.2}$$

As α_p and α_c can be calculated and $f_p(E)$ and $f_c(E)$ are known relationships, virtual monoenergetic images (VMI) at different energies can be constructed. Based on what the viewer would like to see, certain materials can be enhanced or impaired in the CTA reconstruction. A high VMI keV image reconstruction could minimize the absorption of high Z materials, such as stent struts, because Compton scattering is dominant and minimizes the associated beam hardening artifact. At low VMI keV scans, on the other hand, the photoelectric effect is dominant and absorption of high Z is enhanced, possibly resulting in improved contrast between the vessel lumen and surrounding tissues or objects. The optimal energy level settings for reducing the blooming artifact are, however, not yet known, since improved intravascular contrast requires lower energies (40-70 keV), while artifact reduction requires higher energies (>100 keV). [62–64]

The goal of this study is to quantify in-vitro the uncertainty in lumen segmentation that is induced by blooming artifacts by stent markers and stent-in-stent placement. The first aim is to compare the effect of the blooming artifact in conventional and virtual monoenergetic CTA image reconstructions. The second aim is to analyze the effect of the blooming artifact on the segmented in-stent lumen using colliding fronts initialization. It is hypothesized that the blooming artifact is impaired in virtual monoenergetic image reconstructions using high keV levels resulting in an improved visible in-stent lumen and segmented in-stent lumen.

3.2 Methods

Experimental setup

Two Viabahn stents (Gore, Flagstaff, Arizona, USA) were evaluated. The Viabahn stent is a self-expanding, covered (polytetrafluoroethylene) Nitinol stent used for treatment in the AFS. The stent had a nominal diameter of 6 mm, a length of 15 cm and a strut thickness of 150 μm . For the phantom setup, first an acrylic box, inner dimensions 8.5x22x6.5 cm, was designed in Solidworks (2018, SolidWorks Crop, Waltham, Mass USA), shown in Figure 3.1.

Two acrylic pins with a diameter of 5.0 mm corresponding to the dimensions of the AFS were fixed inside the acrylic box. The acrylic box was filled with a Silicone mixture of Sylgard 184 Silicone Elastomer Base and Sylgard 184 Silicone Elastomer Curing Agent in a 10:1 ratio to mimic the surrounding tissue. A vacuum chamber was used to reduce the number of air bubbles in the silicone before pouring. After the silicone was hardened, the pins and box were removed, resulting in a silicone phantom with two hollow tubes, representing two AFSs. The two Viabahn stents were deployed in one of the AFSs with a 10 cm overlap, resulting in one AFS without stents and one AFS with two partly overlapping stents (stent-in-stent).

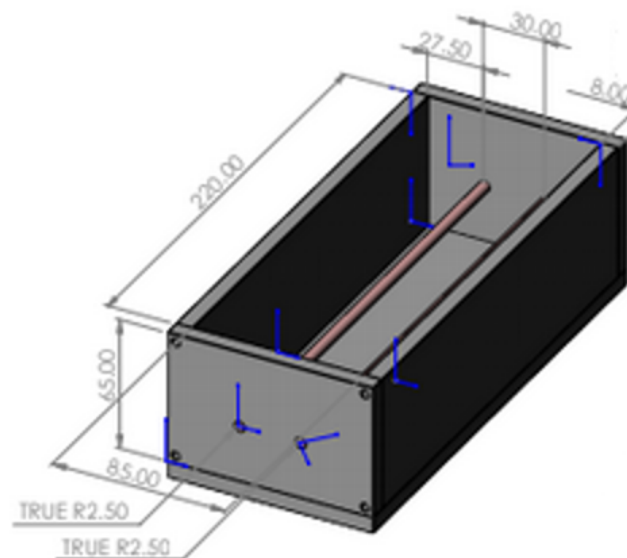


Figure 3.1: Acrylic box, dimensions 220x85x65 mm, containing two pipes, diameter 5 mm, functioning as a mold for the silicone model. The silicone model represents two blood vessels and the surrounding tissue.

Finally, the vessels were filled with Xenetix 300 (Guerbet, Villepinte, France) in a ratio 1:10 with water. Plugs on both ends closed the vessels. The phantom was placed parallel to the z-axis of the CT scanner to mimic the orientation of a subject's AFS inside a CTA-scan.

Scan parameters

Scans were performed on a detector-based spectral CT (IQon Spectral CT, Philips Healthcare, Amsterdam, the Netherlands) with standard scan param-

eters for CTA of the lower limbs: collimation 64 x 0.625 mm, rotation time 0.27 s, pitch 0.6, tube current 125 mA and tube voltage 120 kVp.

Image reconstruction

The conventional images of the vascular phantom were reconstructed with the iDose and iterative model reconstruction (IMR) reconstructions. Furthermore, ten VMI images were reconstructed: 40 keV, 70 - 100 keV in steps of 10 keV and 120 - 200 keV in steps of 20 keV. The iDose and VMI image reconstructions had a slice thickness of 3 mm and the IMR image reconstruction a slice thickness of 0.9 mm. The pixel size for all reconstructions was 0.3223 x 0.3223 mm.

Image analysis

For every image reconstruction, image analysis was performed at five locations:

1. Vessel without stent (L1);
2. One stent (L2);
3. Two overlapping stents (L3);
4. Proximal/distal stent marker, single stent (L4);
5. Proximal/distal stent marker, two overlapping stents (L5).

These analysis locations are visualized in Figure 3.2.

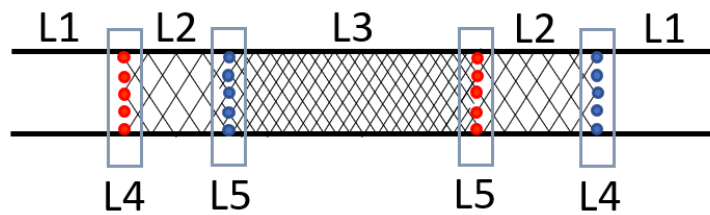


Figure 3.2: Image analysis locations for the in-vitro model. The red and blue dots represent the radiopaque proximal/distal stent markers of the stent grafts. L1: vessel without stent, L2: single stent, L3: double stent, L4: single stent + stent markers, L5: double stent + stent markers.

Image parameters

The obtained images were loaded into MATLAB for objective image analysis. Four parameters were obtained at the analysis locations: the measured lumen diameter as a percentage of the theoretical lumen diameter (PVL), the stent thickness, the contrast-to-noise ratio (CNR) and the signal-to-noise ratio (SNR). First, the intensity profile was determined of a drawn horizontal line in the axial plane, as can be seen in Figure 3.3 as the blue line in the left figure. The visible lumen diameter was measured as the distance between the maximum gradient of the two intensity peaks. The visible lumen diameter was divided by the theoretical lumen diameter (vessel - 2 · strut thickness for single stent, vessel - 4 · strut thickness for double stent) to obtain the PVL. The thickness of the stent struts was determined as the full width at half maximum (FWHM) of the intensity peak, the yellow line in the right figure of Figure 3.3. For L4 and L5, the stent thickness and PVL were determined in one slice as the radiopaque stent markers were only visible in one slice. The stent width and PVL were measured six times and then averaged. For the other analysis locations, the PVL and stent width were measured two times in three consecutive slices and then averaged.

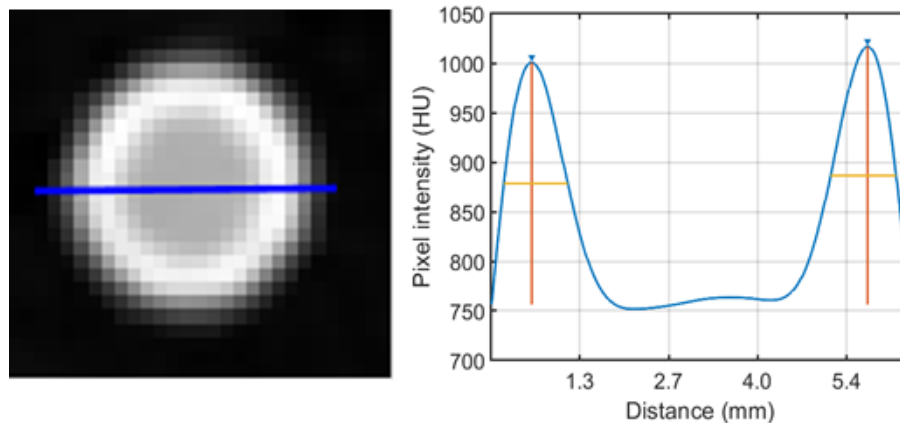


Figure 3.3: Principle of the objective measurement of the visible vessel lumen and the stent strut thickness. Left: axial slice at the double stent location in the 70 keV virtual monoenergetic image reconstruction. The blue line is the horizontal line drawn to determine the pixel intensity profile. Right: the corresponding pixel intensity profile. The blue line shows the intensity profile, the red lines the height of the maximum intensity peaks and the yellow lines the thickness of the stent struts (FWHM).

The CNR and SNR were obtained as objective measurements of the image quality. The CNR and SNR were calculated as follows:

$$\text{CNR} = \frac{\text{HU}_l - \text{HU}_t}{\text{SD}_t} \quad (3.3)$$

$$\text{SNR} = \frac{\text{HU}_l}{\text{SD}_l} \quad (3.4)$$

in which HU_l is the mean pixel intensity of the vessel lumen, HU_t the mean pixel intensity of the surrounding tissue, SD_t the standard deviation of the pixel intensity of the surrounding tissue and SD_l the standard deviation of the pixel intensity of the vessel lumen. The mean and standard deviation of the pixel intensity of the vessel lumen and the surrounding tissue were obtained by placing a rectangular region of interest in the vessel lumen and the surrounding tissue. These regions of interest did not include vessel walls, plaques, stents and blooming artifacts. The mean and standard deviation of these regions of interest were then calculated.

Segmentation

The iDose, IMR and the optimal VMI image reconstruction (largest PVL, smallest stent thickness) were segmented using the *level set method of implicit deformable models* including regularization, explained in Chapter 2, using VMTK-lab (Orobix, Bergamo, Italy). From the obtained segmentation the centerline was determined from which the radius was calculated. The PVL was then calculated for the different analysis locations.

Statistical analysis

Statistical analysis was performed using IBM SPSS statistics 25 (IBM, New York, NY, USA). The difference in PVL, stent thickness, SNR and CNR between each data set was checked for normality using the Shapiro-Wilk test with $p < 0.05$ being significant. In case of a normal distribution, a dependent t-test was performed, otherwise a Wilcoxon signed-rank test was used. The PVL and stent thickness were compared between image reconstructions and analysis locations (pairwise). The SNR and CNR were only compared between the image reconstructions, also pairwise. A p-value of < 0.05 was considered significant.

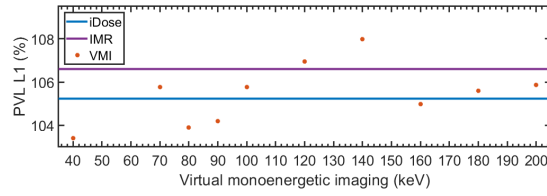
3.3 Results

Image parameters

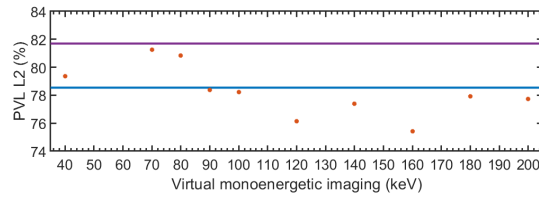
Lumen visibility

The visible lumen as a percentage of the theoretical lumen ranged from 103.41-107.98% for L1, 75.41-81.69% for L2, 70.69-88.30% for L3, 65.18-76.74% for L4 and 64.36-89.18% for L5, as is shown in Figure 3.4. The PVL for every image reconstruction in L1 was higher than 100%, indicating an overestimation of the visible lumen. The PVL of VMI 40 keV was significantly lower and the PVL of VMI 140 keV was significantly higher than the PVL of the iDose image reconstruction ($p < 0.05$). No significant differences were found between the IMR image reconstruction and the iDose and spectral image reconstructions.

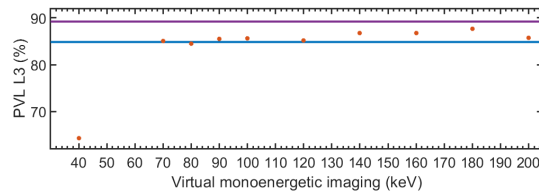
The PVL in L2-L5 were all smaller than 100%, indicating an underestimation of the visible lumen. The PVL at L2 and L4 containing a single stent were significantly lower than the PVL at L3 and L5 containing a double stent ($p < 0.01$) for all image reconstructions. Furthermore, the differences between L2 and L4, and L3 and L5 were significant for all image reconstructions, with L4 being significantly smaller than L2 ($p < 0.01$) and L5 being significantly smaller than L3 ($p < 0.01$). The PVL in the IMR image reconstruction was significantly higher than in the spectral image reconstructions for all analysis locations, except for VMI 70 keV ($p = 0.92$) and 80 keV ($p = 0.46$) at L2 and VMI 180 keV ($p = 0.21$) at L3, and significantly higher than the iDose image reconstruction in analysis locations L2, L4 and L5. The PVL in the iDose image reconstruction was significantly higher compared to the PVL in the spectral image reconstructions in L4 and L5, except for VMI 70 keV ($p = 0.92$) and 80 keV ($p = 0.11$) at L4 and VMI 100 keV at L5 ($p = 0.46$). The PVL in the iDose image reconstruction differed significantly from the spectral image reconstructions at L2 for VMI 40 - 80 keV, VMI 120 keV and VMI 160 keV ($p < 0.05$). For L3, the PVL in the iDose image reconstruction differed significantly compared to the spectral images, except for VMI 80 keV, VMI 120 keV and VMI 200 keV.



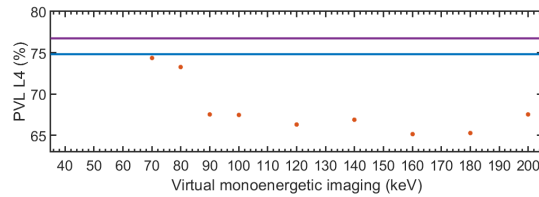
(a) L1: no stent.



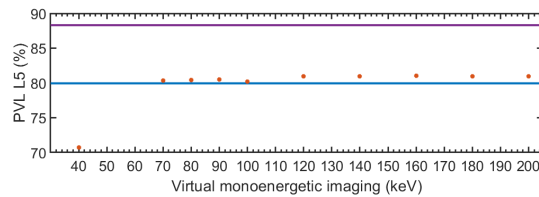
(b) L2: single stent.



(c) L3: double stent.



(d) L4: radiopaque stent marker, single stent.



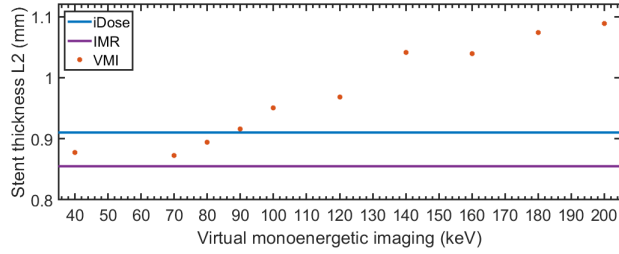
(e) L5: radiopaque stent marker, double stent.

Figure 3.4: Measured visible lumen as a percentage of the theoretical lumen for analysis locations L1 - L5 for the iDose, IMR and several virtual monoenergetic image reconstructions.

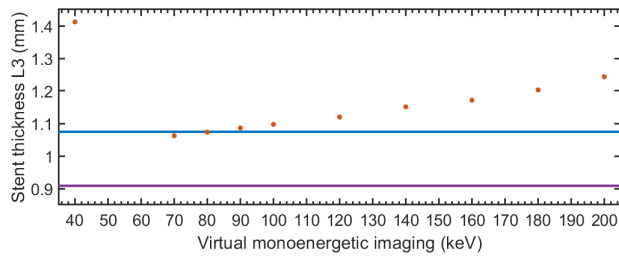
Stent thickness

The measured stent thickness ranged from 0.85 - 1.09 mm at L2 and 0.77 - 1.10 mm at L4 for the single stent (theoretical stent thickness 0.150 mm) and from 0.91 - 1.41 mm at L3 and 0.96 - 1.29 mm at L5 for the double stent (theoretical stent thickness 0.300 mm), as is shown in Figure 3.5. The measured stent thickness for L3 and L5 (double stent) was significantly higher than the measured stent thickness for L2 and L4 (single stent) ($p < 0.01$) for all image reconstructions. The measured stent thickness in L3 was significantly higher than the measured stent thickness in L5 ($p < 0.01$), but no significant difference was found between L2 and L4 ($p = 0.80$). The differences between the IMR image reconstruction and the spectral image reconstructions at all analysis locations were significant ($p < 0.05$), except for VMI 40 keV at L2 ($p = 0.11$). The stent thickness in the iDose image reconstruction was significantly higher than in the VMI 70 keV image reconstruction at L2 and L4 and was significantly lower at L2 for VMI 100 keV - 200 keV and at L4 for VMI 140 keV - 200 keV ($p < 0.05$). For L3, the iDose image reconstruction differed significantly for VMI 40 keV and 120 keV - 200 keV ($p < 0.05$) and for L5, the iDose image reconstruction differed significantly compared to all spectral image reconstructions. The measured stent thickness for the IMR image reconstruction was significantly higher than the iDose image reconstruction for L2, L3, L4 and L5.

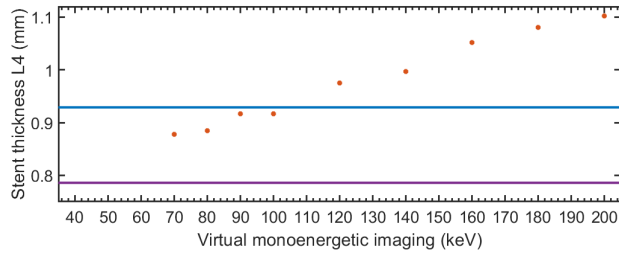
The measured stent thickness gradually increased with an increasing keV level, as can be seen in Figure 3.5. At L3, L4 and L5, all differences in measured stent thickness between the keV levels were significant, except for VMI 70 keV compared to 80 keV ($p = 0.46$) and 90 keV compared to 100 keV ($p = 0.92$) at L4 and VMI 100 keV compared to 120 keV ($p = 0.11$) and VMI 180 keV compared to 200 keV ($p = 0.92$) at L5. At L2, VMI 40 keV compared to 70 keV ($p = 0.92$), VMI 100 keV compared to 120 keV ($p = 0.11$), VMI 140 keV compared to 160 keV ($p = 0.92$) and VMI 180 keV compared to 200 keV ($p = 0.11$) were not significant, the other sets were.



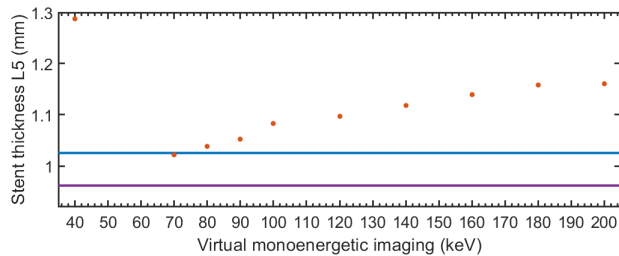
(a) L2: single stent.



(b) L3: double stent.



(c) L4: radiopaque stent marker, single stent.



(d) L5: radiopaque stent marker, double stent.

Figure 3.5: Measured stent thickness (mm) for analysis location L2 - L5 in the iDose, IMR and several virtual monoenergetic image reconstructions.

Image quality

The SNR and CNR decreased as the VMI energy level increased, as can be seen in Figure 3.6. There was a significant difference in SNR between the VMI keV levels ($p < 0.05$) except for VMI 80 keV compared to VMI 90 keV, VMI 160 keV compared to VMI 180 keV and VMI 180 keV compared to 200 keV. The differences in CNR between the VMI keV levels were all significant ($p < 0.05$). The SNR of VMI 40 - 70 keV were significantly higher than the SNR of the iDose and IMR image reconstructions ($p = 0.043$) and the SNR of VMI 120 - 200 keV were significantly lower than the iDose and IMR image reconstructions ($p = 0.043$). The CNR of VMI 40-70 keV were significantly higher than the CNR of the iDose image reconstruction ($p = 0.043$) and the CNR of VMI 100-200 keV were significantly lower than the iDose image reconstruction ($p = 0.043$). The CNR of VMI 40 keV was significantly higher than the CNR of the IMR image reconstruction ($p = 0.043$) and the CNR of VMI 90 - 200 keV were significantly lower than the CNR of the IMR image reconstruction ($p = 0.043$).

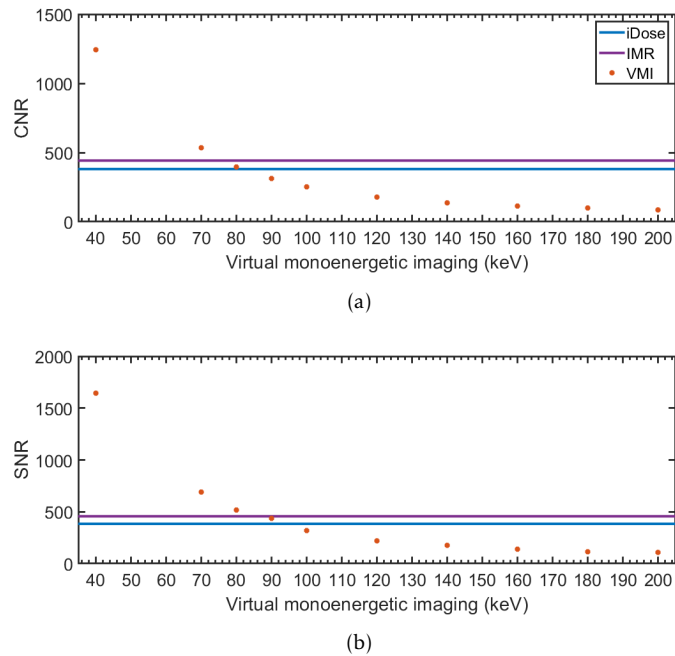


Figure 3.6: The contrast-to-noise ratio (CNR) and signal-to-noise ratio (SNR) for the iDose, IMR and several virtual monoenergetic image reconstructions.

Segmentation

The segmentation and PVL of image reconstructions VMI 70 keV, iDose and IMR are shown in Figures 3.7, 3.8 and 3.9, respectively. Two interruptions in the segmentation can be observed, which were caused by air bubbles in the vessel lumen (black asterisks). The mean diameter and standard deviation for L1, L2 and L3 for the IMR, iDose and VMI 70 keV are shown in Table 3.1. A significant difference was found between all analysis location between the iDose and 70 keV VMI image reconstruction. For L1 70 keV VMI was significantly higher ($p = 0.012$), for L2 70 keV VMI was significantly higher ($p < 0.01$) and for L3 iDose was significantly higher ($p < 0.01$). The PVL in the IMR image reconstruction was significantly larger than the iDose and 70 keV VMI image reconstructions for all analysis locations ($p < 0.01$). The mean PVL values obtained in the three reconstructions were all significantly lower than the measured PVL in the corresponding CTA image reconstruction.

Table 3.1: The diameter (mm) for analysis locations L1 - L3 for the segmentation of the IMR, iDose and VMI 70keV image reconstructions, shown as mean \pm standard deviation.

	Diameter (mm)		
	IMR	iDose	VMI 70 keV
L1	94.47 \pm 4.31	75.44 \pm 8.69	80.64 \pm 6.85
L2	75.99 \pm 5.62	69.99 \pm 5.99	73.51 \pm 4.08
L3	80.22 \pm 0.98	74.73 \pm 3.42	70.35 \pm 1.57

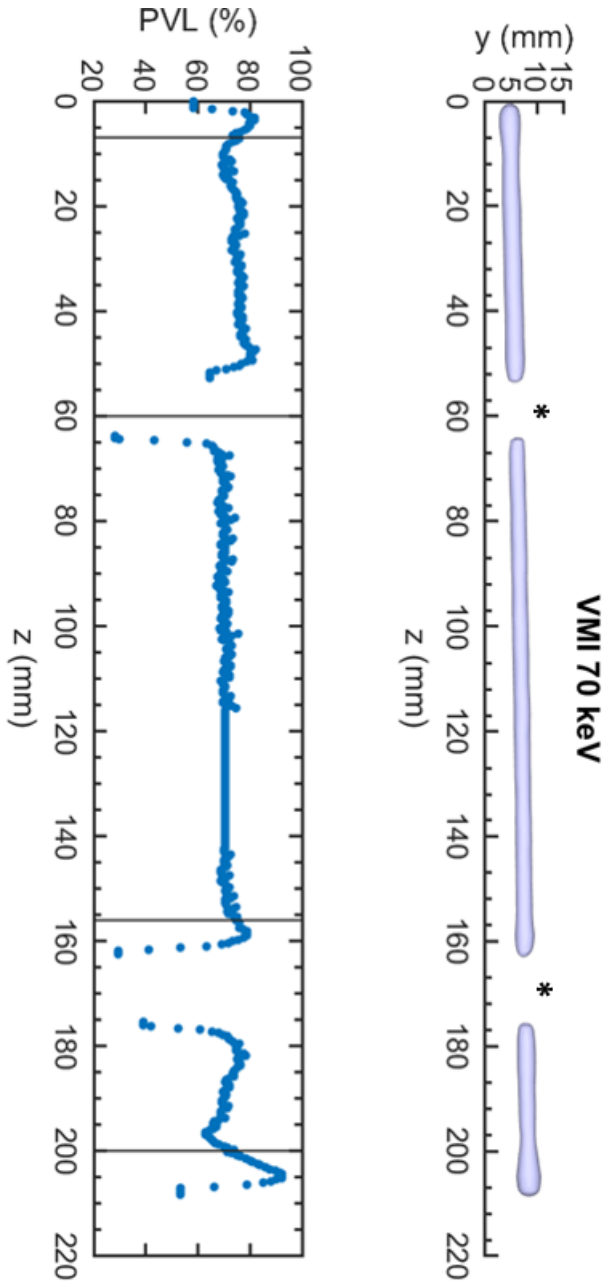


Figure 3.7: The segmentation (top) and segmented lumen as a percentage of the theoretical lumen (bottom) for the VMI 70 keV image reconstruction. The vertical black lines indicate the radiopaque stent markers and the black asterisks air bubbles in the contrast.

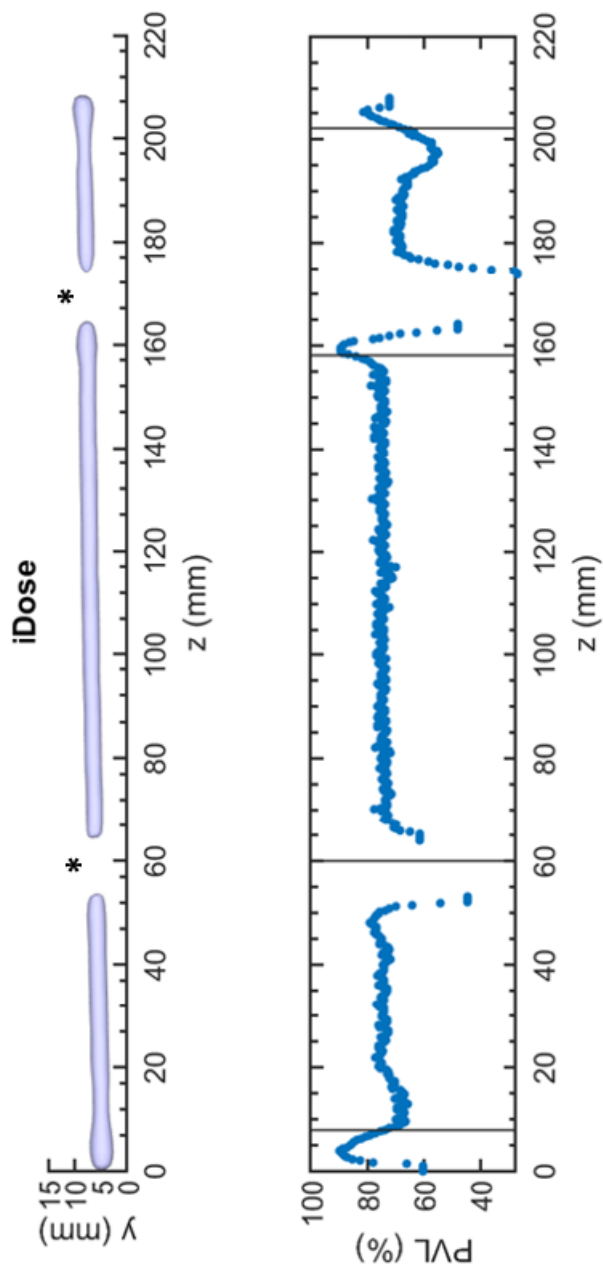


Figure 3.8: The segmentation (top) and segmented lumen as a percentage of the theoretical lumen (bottom) for the iDose image reconstruction. The vertical black lines indicate the radiopaque stent markers and the black asterisks air bubbles in the contrast.

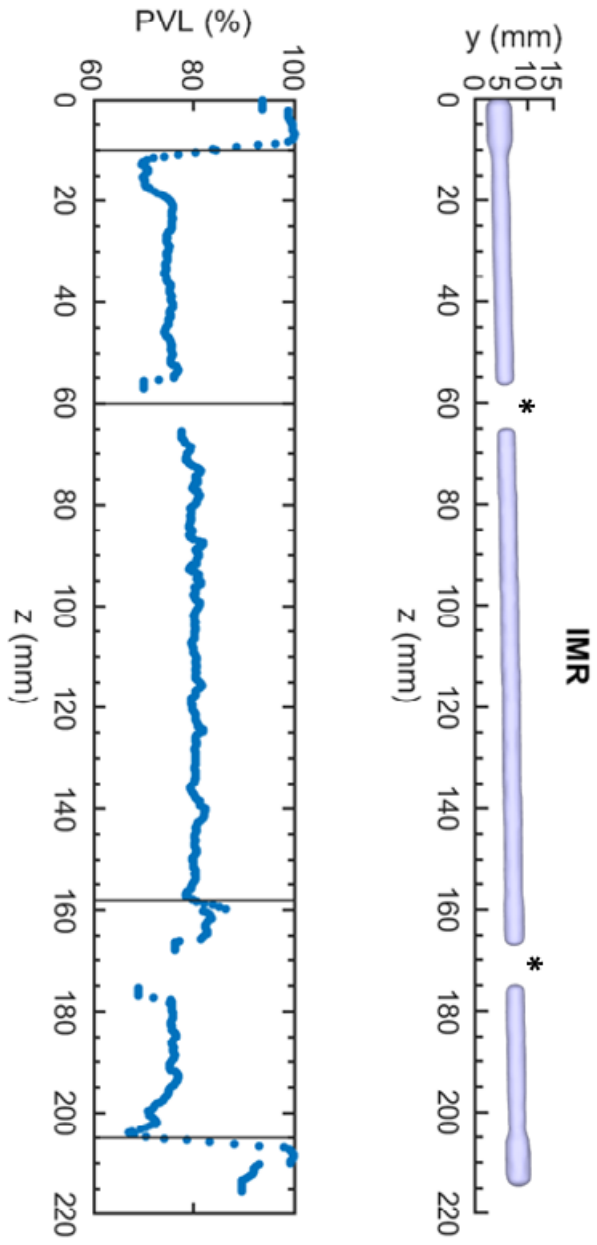


Figure 3.9: The segmentation (top) and segmented lumen as a percentage of the theoretical lumen (bottom) for the IMR image reconstruction. The vertical black lines indicate the radiopaque stent markers and the black asterisks air bubbles in the contrast.

3.4 Discussion

The effect of the blooming artifact on the visible in-stent lumen in conventional and virtual monoenergetic CTA image reconstructions, and on the segmented arterial lumen using the *level set method of implicit deformable models* was investigated.

CTA image reconstruction

Contrary to expectations, this study showed that the blooming artifact showed the largest reduction in the IMR image reconstruction, a conventional image reconstruction. The measured stent thickness in the IMR image reconstruction was significantly lower than the spectral and iDose image reconstructions for all analysis locations (L2- L5), except for VMI 40 keV at L2. Furthermore, the PVL measured in the IMR image reconstruction was significantly higher compared to most of the spectral image reconstructions and the iDose image reconstruction. As, due to the blooming artifact, the apparent strut thickness is increased and the visible in-stent lumen is reduced, the results of this study imply that the blooming artifact is smaller in the IMR image reconstruction compared to the iDose and spectral image reconstructions. The other conventional image reconstruction, iDose, did not perform better than all spectral image reconstructions. The measured stent thickness in the VMI 70 keV image reconstruction was, in general, significantly smaller than the measured stent thickness in the iDose image reconstruction. When comparing the PVL in the iDose image reconstruction to the spectral image reconstructions, highly varying results were observed and no clear trend was seen.

Furthermore, it was hypothesized that the blooming artifact was reduced more in the VMI image reconstructions using high keV levels compared to the VMI image reconstructions using low keV levels. However, the measured stent thickness showed the opposite trend: the measured stent thickness gradually increased with an increasing keV level (70 keV - 200 keV). The measured stent thickness in the VMI 40 keV image reconstruction did not fit in this trend and was in analysis location L3 and L5 significantly larger than the measured stent thickness in the other spectral image reconstructions. A decreasing PVL with increasing keV level corresponding to the trend of the measured stent thickness, was observed in analysis locations L2 and L4. The PVL measured in the VMI 40 keV image reconstruction in analysis locations L3 and L5 was also significantly smaller than the PVL in the other spectral image reconstructions. The PVL measured in the other spectral image reconstructions (70 keV - 200 keV), however, did not decrease with an increasing keV level.

The inconsistency between the hypothesis and the results could be the result of the two mechanisms influencing the amount of blooming in the CTA scan: the beam hardening artifact and partial volume averaging. The first mechanism, the beam hardening artifact, could be reduced using VMI image reconstructions with high keV levels, as stated in Section 3.1. However, increasing the keV level is at the expense of the image quality. [64] This effect was seen in the SNR and CNR results: the SNR and CNR generally decreased significantly with increasing keV level steps. The attenuation of the used iodinated contrast increased with a decreasing keV level as the keV level reached the k-edge of iodine (33 keV). [65] The image quality in the VMI 40 keV image reconstruction was, thus, significantly better than the image quality in the VMI 200 keV image reconstruction. However, the VMI 40 keV image reconstruction was more influenced by beam hardening than the VMI 200 keV image reconstruction, resulting in a significantly higher measured stent thickness. Because of this trade off between the beam hardening artifact reduction and image quality, the optimal spectral image reconstruction is somewhere in between the 40 keV and 200 keV, benefiting from the optimal balance between artifact reduction and image quality. In this study, the optimal spectral image reconstruction was around 70 keV, as the measured stent thickness was smallest in this spectral image reconstruction.

The second mechanism, partial volume averaging, is the result of averaging all different attenuation values within a voxel, causing high attenuation values to dominate the final attenuation value of the voxel. The effect of partial volume averaging could be reduced by improving the spatial resolution since the spatial resolution determines the size of the voxel. The spatial resolution can be improved by reducing the pixel size and slice thickness, amongst others. In this study, the slice thickness of the IMR image reconstruction was smaller than in the other image reconstructions, namely 0.9 mm instead of 3 mm. Although, the CNR and SNR for the IMR image reconstruction were significantly lower than the CNR and SNR in the VMI 70 keV image reconstruction, the measured stent thickness in the IMR image reconstruction was significantly lower. The results of this study do, therefore, imply that partial volume averaging has a larger impact on the amount of blooming in the CTA scan than the beam hardening artifact, which caused the IMR image reconstruction to be the optimal image reconstruction to minimize the blooming artifact in the CTA scan.

The amount of blooming in conventional and spectral image reconstructions has already been investigated. Halpern et al. (2009) [66] studied the effect of blooming on the visible in-stent lumen in a coronary phantom using a single-

source dual-energy CT system. The FWHM was obtained to determine the strut thickness and the visible in-stent lumen. No significant differences between the conventional, spectral containing low keV levels or spectral containing high keV levels image reconstructions were found. However, the spectral image reconstruction containing high keV levels performed significantly better than the conventional and spectral containing low keV levels image reconstruction when the visible in-stent lumen and strut thickness were measured by two independent observers. Zhang et al. (2019) [64], who studied the blooming artifact caused by stents in the lower extremities in the iDose and VMI image reconstructions, also measured the in-stent visible lumen by two independent observers. They found a significantly higher measured in-stent lumen for VMI 80 keV - 150 keV compared to the measured in-stent lumen for the iDose image reconstruction. A subjective image quality score, including attenuation, noise and stent-related artifacts, was also assessed and the score was significantly higher between 70 keV - 90 keV compared to the iDose image reconstruction. Combining the measured in-stent lumen and the image quality resulted in an optimal VMI image reconstruction at 90 keV.

It is surprising that the objective and subjective measurements provide contradicting results and the question arises whether these results could be compared. Subjective results by Halpern and Zhang suggest that using spectral images with high keV levels improves the visible in-stent lumen and strut thickness. [64,66] However, objective measurements, FWHM method for strut thickness and visible in-stent lumen by Halpern and FWHM method for strut thickness and maximum gradient method for visible in-stent lumen in this study, did not find significant improvements when using spectral images with high keV levels. Especially for the maximum gradient method it is surprising that it shows contradicting results, since it was designed to represent a subjective measurement. It was thought that an observer would choose the maximal difference between pixel intensities as the interface between the vessel lumen and the stent strut. However, these results imply that the parameters analyzed using subjective measurements, differ from the parameters using objective measurements. This could also explain the higher optimal VMI keV level found by Zhang, VMI 90 keV, compared to the optimal VMI keV level found in this study, VMI 70 keV. [64]

Segmentation

The PVL based on the segmentation showed similar results as the results obtained in the CTA image reconstruction analysis. The PVL measured in the IMR segmentation was significantly larger than the PVL measured in the other segmentations, indicating that the segmentation was less affected by the

blooming artifact in the IMR image reconstruction. The PVL measured in the VMI 70 keV segmentation was significantly higher than the iDose segmentation in two out of three analysis locations, indicating that the VMI 70 keV reconstruction performs slightly better than the iDose image reconstruction. This was also seen in the CTA image reconstruction analysis. The segmentation of the optimal CTA image reconstruction, IMR, had mean PVL values of 94.5%, 76.0% and 80.2% for analysis locations L1, L2 and L3, respectively. The maximum deviation of the true lumen was, thus, 23%.

The mean PVL values of analysis locations L1, L2 and L3 in the segmentations were significantly smaller than measured in the CTA scan. This was probably caused by the proximal/distal radiopaque stent markers. In the centerline data obtained from the segmentation, it was not clear what data points belonged to the radiopaque stent markers. It was, therefore, chosen to divide the segmentation into three analysis locations, L1, L2 and L3, instead of five. The data of the radiopaque stent markers was automatically included in the other analysis locations. The effect of the radiopaque stent markers, reducing the diameter of the segmented lumen, was, therefore, also included in the mean of the other analysis locations.

Although it was not possible to determine the exact location of the radiopaque stent markers in the centerline data, the approximate location was known: L4 around 10 and 210 mm, L5 around 60 and 160 mm. Based on this information, it was found that the effect of the radiopaque stent markers on the segmented arterial lumen was most prominent in analysis location L4 (radiopaque stent marker, single stent) for all three segmentations. The segmentation based on the IMR image reconstruction showed an underestimation in PVL of 33% at approximately 210 mm, thus near the proximal/distal radiopaque stent marker of the single stent. Surprisingly, the effect of the radiopaque stent marker in analysis location L5 (radiopaque stent marker, double stent) was not observed in this analysis. In the transition of double stent to single stent, the PVL remained constant and then increased. It could be possible that the radiopaque stent marker of stent 1 was positioned between the stent struts of stent 2. L5 was then not a radiopaque stent marker with a double stent, but with a single stent. As the PVL was calculated using the theoretical diameter of a double stent, the PVL could be overestimated. It could also be possible that the blooming artifact caused by the radiopaque stent marker did not stand out, because the single and double stent also caused a blooming artifact.

Limitations

The PVL measured in the CTA reconstructions and segmentations for the single stent analysis locations was, surprisingly, significantly lower than or similar to the PVL for the double stent analysis locations. As in case of the double stent location the stent strut layer is doubled, it was thought that the blooming artifact would be more prominent in these analysis locations. A likely cause for this discrepancy is the insufficient image resolution of the CTA reconstructions. The pixel size in the CTA reconstructions was 0.3223 mm, while the stent strut was 0.150 mm. This means that both a single stent (0.150 mm) and a double stent (0.300 mm) could be detected in only one pixel and thus result a similar attenuation in the CTA scan. Furthermore, the strut thickness of the single stent would always be overestimated as being two times the real size as the CTA scan cannot distinguish the single stent struts. Since the single stent strut is always overestimated, the visible in-stent lumen is always underestimated. Due to the resolution, it is possible that the single stent strut is relatively more overestimated than the double stent struts, resulting in a similar measured stent thickness. The theoretical in-stent lumen for the single and double stent do, however, differ, which could have resulted in a smaller PVL in the single stent locations compared to the double stent locations.

Furthermore, the theoretical in-stent lumen used to calculate the PVL was based on an ideal situation in which the stents were placed perfectly to the vessel wall. However, it could be that the stents were not completely unfolded during stent placement, especially the proximal and distal parts of the stent. It is also possible that the pressure of the double stent was higher than expected, causing the lumen diameter of the vessel to increase. Both cases result in uncertainty in the theoretical lumen. Uncertainty also arose from the determination of analysis locations L4 and L5. The radiopaque stent markers for each analysis location were only visible in one slice. It was, therefore, harder to draw a representative line used to determine the intensity profile.

Future perspectives

For future research it would be recommended to study the effect of the blooming artifact on the visible in-stent lumen and segmented arterial lumen using optical coherence tomography (OCT). [67] OCT is an intravascular imaging modality that uses near-infrared light and obtains cross-sectional images of the vessel lumen. It is able to detect the vessel lumen and stent struts with high resolution (axial 12 - 14 μm , lateral 20 - 40 μm), which is ten times as small as the pixel size in the used CTA reconstructions. The improved resolution could reduce the blooming artifact by minimizing partial volume av-

eraging. [66] Furthermore, the resolution would be sufficient to distinguish individual stent struts and be able to compare the blooming artifact caused by single and double stents. Finally, OCT could give more insight in the positioning of the stent to the vessel wall and provide a better theoretical in-stent lumen diameter.

It would also be interesting to compare the subjective and objective measurement techniques for the PVL and stent thickness. Comparing the used objective techniques in this study to the subjective technique in the study by Zhang et al. (2019) [64] by performing one study combining both methods, could provide more insight in the effect of using a VMI image reconstruction with high keV levels on the blooming artifact. Furthermore, in case the subjective and objective methods are not comparable, it could provide more insight in the differences between both methods and could possibly improve future methods. Moreover, it would be recommended to theoretically analyze the effect of the contrast, stent struts and stent markers on the CTA scan to be able to understand the results of the conventional and spectral image reconstructions better.

This study emphasized the balance between artifact reduction, image quality and partial volume averaging on the blooming artifact in the CTA scan. VMI image reconstructions can be used to minimize the beam hardening artifact, but this effect is minimal with insufficient image quality and image resolution. The blooming artifact was most prominent near the proximal/distal radiopaque stent marker causing a vessel narrowing at the stent marker in the segmentation. [68] Using this segmentation in a patient-specific CFD simulation would probably adversely affect the CFD solution as the segmentation contains a false vessel narrowing. To know the effect of uncertainty in geometry on the CFD solution, uncertainty quantification could be performed, see Chapter 4. Furthermore, the geometrical error could be corrected using the *active tubes segmentation technique* (Chapter 2), but the feasibility of this technique has not yet been established. Therefore, more research is needed to find the optimal image reconstruction and segmentation technique to minimize the blooming artifact and optimize the visible in-stent lumen. The optimized visible in-stent lumen could eventually be used to improve the diagnosis and treatment of PAD and reduce the uncertainty in the patient-specific geometry used in CFD.

3.5 Conclusion

The conventional IMR image reconstruction reduced the blooming artifact caused by stent struts more than the conventional iDose and virtual monoenergetic image reconstructions. This is most likely caused by the reduced slice thickness compared to the other image reconstructions, thereby reducing partial volume averaging and thus the blooming artifact. The underestimation of the visible lumen was with 33% most prominent near the proximal/distal radiopaque stent markers. Conventional IMR and virtual monoenergetic image reconstructions with similarly reduced pixel size or slice thickness should be compared using subjective and objective measurement methods.

Uncertainty quantification

4

4.1 Introduction

Arterial hemodynamics play an important role in the local development and progression of atherosclerosis. [11, 12] Disturbed flow, as is seen near bifurcations, branches and curvatures, resulting in a low WSS (<0.4 Pa), causes the endothelium to become more susceptible to atherosclerosis. [13] Visualizing the blood flow and flow-derived parameters in patients could provide a better understanding of the development and progression of atherosclerotic plaques. The complex blood flow could be simulated using CFD. [19, 44] With CFD flow parameters that are hard to acquire in patients, such as the WSS, can be obtained and the effect of changes due to a pathology or treatment on the blood flow can be simulated. However, for clinically feasible CFD simulations, simplifications are inevitable to reduce the complexity of the computational model and to compensate for the lack of (adequate) patient-specific data needed as input to the CFD model. These uncertainties in the inputs of the CFD model can affect the CFD solution. [19, 44]

Input parameters that could affect the accuracy of the CFD solution include the geometry, blood properties and boundary conditions. The distribution and magnitude of the WSS are highly sensitive to uncertainties in the geometry, which could induce a change in TAWSS in the order of 37% to 48%. [44, 69–71] These changes in TAWSS magnitude and distribution are much higher than the changes due to uncertainty in the inlet and outlet boundary condition, which are in the order of 10% and 15–23%, respectively. [44, 72–75] Uncertainty in the wall boundary condition and blood viscosity also induce changes in the TAWSS magnitude, 30% and 10%, respectively, but do not significantly change the TAWSS distribution. [44, 48, 49, 51] As these input parameters could all influence the accuracy of the CFD solution, it is important to know the uncertainty in the input parameters and to quantify the sensitivity of the CFD solution to these uncertainties to be able to set appropriate input parameters.

The AFS is a common anatomical site for the development of atherosclerotic plaques, which are often treated with stents. [3–5] In about 20% of the patients, however, an in-stent restenosis occurs within one year after intervention. [8,9] Being able to visualize blood flow dynamics in these patients could provide a better understanding and an improved prediction of stent failure. The objective of this study is to analyze the effect of uncertainty in the geometry and inlet boundary condition on the CFD solution in the stented AFS. In Chapter 3 it was shown that uncertainty in geometry caused by the blooming artifact of stent struts was most prominent near proximal/distal radiopaque stent markers. Uncertainty in geometry was, therefore, studied by varying the vessel diameter near these proximal/distal stent markers. In Chapter 2 two methods to obtain a velocity profile as the inlet boundary condition were elaborated: an analytical Womersley velocity profile and an experimentally measured echo PIV velocity profile. Both inlet velocity profiles were compared to analyze the effect of uncertainty in the inlet boundary condition on the CFD solution.

4.2 Method

The current study is a continuation of a previous study by our group (CCMO nr: 2018-4355), investigating the feasibility of femoral blood flow quantification in and around stented lesions using echo PIV.

Study population

Two patients who recently (<6 weeks) received endovascular treatment of a lesion in the AFS with a bare metal or covered stent were studied. Exclusion criteria included uncontrolled hypertension, severe pulmonary disease and clinically unstable cardiac disease. **Patient 1** received two self-expanding stent grafts (Gore Viabahn, distal 250x6 mm and proximal 150x6 mm). Patient 1 already had one bare metal stent (length 60 mm). The overlap between the bare metal and the distal Viabahn stent was 35 mm and the overlap between the two Viabahn stents was 80 mm. **Patient 2** received two self-expanding stent grafts (Medtronic Everflex, distal 100x6 mm and proximal 200x6 mm). The overlap between the stent grafts was 50 mm.

Measurements

Apart from routine clinical care, study procedures included additional measurements to obtain the patient-specific data necessary for the CFD simulation. Around the time of the surgery the hematocrit was measured. Three to seven weeks after stent placement, a CTA scan, DUS measurement and echo

PIV measurement of the femoral bifurcation were obtained. The measurement locations for the DUS and echo PIV measurement are shown in Figure 4.1. Both the DUS and echo PIV measurement were performed in the AFC (1), AFP (3) and AFS (pre (4) and post stent (5)). The echo PIV measurement also included a measurement in the femoral bifurcation (2).

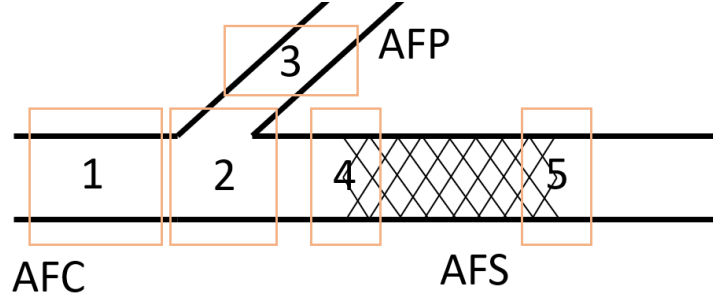


Figure 4.1: Measurement locations in the femoral bifurcation: (1) AFC, (2) femoral bifurcation, (3) AFP, (4) AFS pre stent and (5) AFS post stent.

CFD model

The post-operative IMR CTA image reconstruction was used to segment the femoral bifurcation using VMTKLab. The *level set method of implicit deformable models* including regularization was used to reconstruct the 3D patient-specific geometry of the patient. For the proximal/distal radiopaque stent markers the *active tubes segmentation technique* was used. An unstructured mesh containing tetrahedals was created using the open-source software SimVascular (SimTK, Stanford, USA). [76] A three-layer prismatic boundary layer was added to more accurately resolve the boundary layer with high velocity gradients. The convergence of the mesh was checked using the 95th percentile of the TAWSS. The TAWSS was measured on the vessel wall along the first few centimeters of the proximal AFS, including the proximal stent marker, and the 95th percentile was calculated. This calculated 95th percentile of the TAWSS was compared to the 95th percentile of a mesh containing twice as many elements. The mesh was considered converged when the difference between the calculated 95th percentile of the TAWSS of the mesh and the finer mesh was less than 5%.

At the inlet a Womersley velocity profile, derived from DUS measurements as mentioned in Chapter 2, was imposed. A 3-element Windkessel model was chosen as outlet boundary condition. The values for R_p , C and R_d in the AFS and AFP were set to match the DUS measurements at these locations as

well. For the wall boundary condition a rigid wall with a no-slip condition was set. Blood was assumed to be Newtonian as the diameter of the femoral arteries is large. Furthermore, the blood density was assumed constant and the blood flow incompressible. The simulations were performed with Simvascular, which uses a finite element code. For every simulation, first a steady simulation was performed to optimize the convergence towards a periodic solution for the pulsatile simulation. At least five cardiac cycles were simulated in the pulsatile simulation to reach a periodic solution and only the last cardiac cycle was used in the analysis.

Uncertainty quantification

The effect of uncertainty in the geometry and inlet boundary condition on the accuracy of the CFD solution were studied. The CFD model as described above, was used, but the geometry and inlet boundary condition were varied, as is elaborated below.

Geometry

Patient 1 was selected to analyze the effect of uncertainty in the geometry on the CFD solution. The parameter settings used in the CFD simulation of all cases of patient 1 are shown in Table 4.1.

Table 4.1: Parameter settings for the CFD simulation of patient 1.

	Blood properties	AFC	AFS	AFP
Hematocrit	3.85×10^{-1}			
Dynamic viscosity ($\text{g mm}^{-1} \text{s}^{-1}$)	3.50×10^{-3}			
Fluid density (g mm^{-3})	1.06×10^{-3}			
Kinematic viscosity ($\text{mm}^2 \text{s}^{-1}$)	3.26			
Diameter (mm)		7.00	6.00	5.00
R_p ($\text{g mm}^{-4} \text{s}^{-1}$)			3.92×10^{-2}	7.18×10^{-2}
C ($\text{mm}^4 \text{s}^2 \text{g}^{-1}$)			4.51×10^{-1}	3.00×10^{-1}
R_d ($\text{g mm}^{-4} \text{s}^{-1}$)			4.13	3.65

As in Chapter 3 it was found that the uncertainty in geometry is most prominent at proximal/distal stent markers, the vessel diameter at the first proxi-

mal stent marker in the segmentation of patient 1 was varied. Based on the standard segmentation of patient 1, two situations were modeled: underestimation and overestimation of the vessel diameter. First, the initializations for under- and overestimation were created using *active tubes initialization* (Chapter 2). For the overestimation situation, the radius of the seed included the vessel lumen and the stent struts, visualized in Figure 4.2 with the orange circle. For the underestimation situation, the radius of the seed excluded the stent struts (blue circle in Figure 4.2). Based on these initializations, several segmentations with different vessel diameters at the proximal stent marker were created by adjusting the amount of curvature smoothing (value between 0 and 1). An increased curvature resulted in a decreased lumen diameter. The cases investigated in this study, their diameter at the proximal stent marker and the diameter difference between the case and the standard segmentation, are shown in Table 4.2. The segmentations represent a set of scenarios of extreme under- and overestimation found in Chapter 3 (S1 and S4) and a more realistic range of under- and overestimation in the order of pixel size errors (S2 and S3).

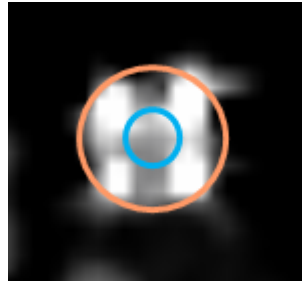


Figure 4.2: Underestimation (blue) and overestimation (orange) of the vessel lumen at the proximal radiopaque stent marker.

Table 4.2: The segmented vessel diameters at the proximal radiopaque stent marker for the standard segmentation and the under- and overestimation cases. ΔD is the difference in diameter between the standard segmentation and the case.

	Case S1	Case S2	Standard	Case S3	Case S4
Diameter proximal marker (mm)	2.82	3.70	4.44	5.12	6.16
ΔD (mm [%])	-1.62 (36.5%)	-0.70 (16.7%)	-	0.68 (16.0%)	1.74 (38.7%)

Inlet boundary condition

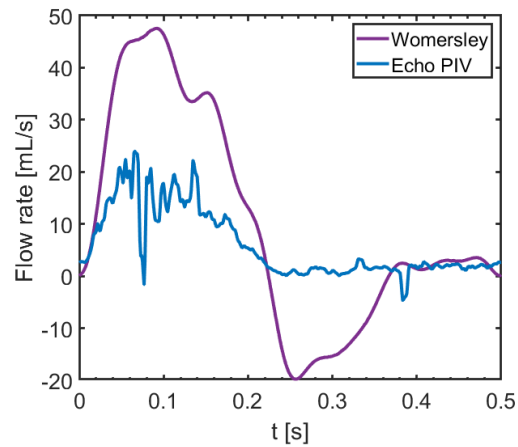
Patient 2 was selected to analyze the effect of the inlet velocity profile on the CFD solution. The parameter settings used in the CFD simulation of all cases of patient 2 are shown in Table 4.3. At the inlet two velocity profiles were imposed: an analytical Womersley’s velocity profile based on the flow rate measured with DUS and an experimentally measured echo PIV velocity profile. Several steps were taken to transform the echo PIV data to a usable inlet velocity profile for the CFD simulation. The two major transformations were the conversion of the 2D longitudinal echo PIV data to a 3D axial velocity field and fitting the echo PIV data to the grid points used in SimVascular. A 3D velocity field was obtained by converting the data to a polar coordinate system and linearly interpolate along the theta-coordinate. Then bilinear interpolation was used to obtain velocity data at the grid points used in Simvascular. Temporal smoothing of the echo PIV data was performed to remove measurement errors. A detailed description of the steps taken to transform and smooth the echo PIV data is provided in Appendix A.

Table 4.3: Parameter settings for the CFD simulation of patient 2.

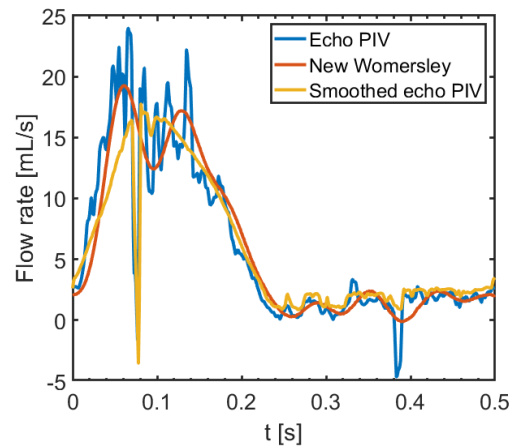
	Blood properties	AFC	AFS	AFP
Hematocrit	4.10×10^{-1}			
Dynamic viscosity ($\text{g mm}^{-1} \text{s}^{-1}$)	3.70×10^{-3}			
Fluid density (g mm^{-3})	1.06×10^{-3}			
Kinematic viscosity ($\text{mm}^2 \text{s}^{-1}$)	3.47			
Diameter (mm)		8.00	5.00	5.00
R_p ($\text{g mm}^{-4} \text{s}^{-1}$)			5.31×10^{-2}	7.18×10^{-2}
C ($\text{mm}^4 \text{s}^2 \text{g}^{-1}$)			8.95×10^{-2}	4.47×10^{-1}
R_d ($\text{g mm}^{-4} \text{s}^{-1}$)			4.43	2.14

The flow rates of the Womersley simulation and original echo PIV simulation are shown in Figure 4.3a. As the difference in flow rates between the simulations was large, a third simulation was performed: a Womersley inlet velocity profile with the flow rate based on the echo PIV measurement. The original flow rate profile of the echo PIV data was used, as smoothing of the echo PIV data was not successful, shown in Figure 4.3b. Finally, three simulations were performed: Womersley simulation with flow rate based on DUS measurement

(Womersley simulation), Womersley simulation with flow rate based on echo PIV measurement (new Womersley simulation) and echo PIV simulation with flow rate based on echo PIV measurement (echo PIV simulation).



(a)



(b)

Figure 4.3: Top: (a) Flow rate for the Womersley and echo PIV simulations. Bottom (b) Flow rate for the echo PIV, new Womersley and smoothed echo PIV simulation.

Data analysis

The data of the CFD simulations were imported in Tecplot and Paraview. Tecplot was used to create velocity streamlines during different moments of the cardiac cycle: peak systole, systolic deceleration and peak backflow, shown in Figure 4.4. The TAWSS over one cardiac cycle was calculated (Equation 4.1) and visualized as a contour of the geometry. Using Tecplot, the differences in TAWSS distribution, especially low TAWSS (<0.4 Pa) were reported. To obtain differences in TAWSS magnitude (global and local), Paraview was used. The 95th percentile of the global and local TAWSS and the percentage of regions of low TAWSS were calculated.

$$\text{TAWSS} = \frac{1}{T} \int_0^T |\tau_w| dt \quad (4.1)$$

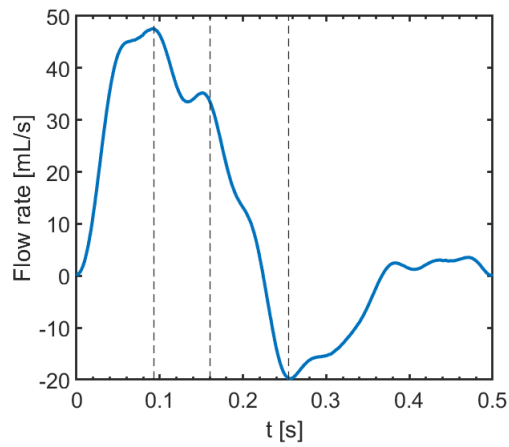


Figure 4.4: The flow rate during one cardiac cycle. The dotted lines indicate the time instances for which velocity streamlines are visualized: peak systole, systolic deceleration and peak backflow.

4.3 Results

Uncertainty quantification - geometry

The patient-specific geometry and the TAWSS over one cardiac cycle for the standard simulation of patient 1 are shown in Figure 4.6. The radiopaque stent markers and the direction of the stent graft are indicated with the arrows. The AFC showed some changes in lumen diameter due to plaques. Regions of low TAWSS were seen especially in the AFC, around the femoral bifurcation and distal to the bare metal stent. The TAWSS over one cardiac cycle around the femoral bifurcation for all cases of patient 1 is shown in Figure 4.7. The differences in lumen diameter around the first proximal radiopaque stent marker (black arrow) between the cases is evident. The distribution of low TAWSS (<0.4 Pa) for all cases was similar, except for the proximal AFS. In the extreme lumen underestimation case (case S1) a new stroke of low TAWSS was seen distal to the radiopaque stent marker. This region of low TAWSS was not seen in the more realistic lumen underestimation case (case S2). For the overestimation cases (case S3 and case S4) a region of low TAWSS was observed proximal to the radiopaque stent marker. This region was larger for case S4. The total geometry and TAWSS for case S1 - S4 are shown in Appendix B.

The velocity streamlines for all cases of patient 1 are visualized during peak systole (Figure 4.8), systolic deceleration (Figure 4.9) and peak backflow (Figure 4.10). During peak systole, low velocities and flow recirculations were seen at the inner side of the curved AFC and higher velocities (120 - 180 cm/s) at the outer side of the curved AFC. The higher velocities entered the inner side of the femoral bifurcation and flowed through the AFS and AFP. Flow recirculations at the outer side of the femoral bifurcation and extending into the proximal AFS at the outer side of the femoral bifurcation were observed in all cases. The higher velocities entered the AFS at the inner side of the bifurcation. In case S3 and especially case S4 these higher velocities moved into the vessel enlargement at the proximal radiopaque stent marker, causing a flow split: higher velocities flowed further downstream of the AFS and flow recirculations developed proximal to the maximum of the vessel enlargement. This was not seen in the standard simulation or in the lumen underestimation cases. High velocities (160 - 200 cm/s) in and distal to the vessel narrowing at the proximal radiopaque stent marker were observed in case S1 during peak systole and systolic deceleration. Due to a flow deceleration distal to the vessel narrowing, flow recirculations developed distal to the vessel narrowing at the outer side of the femoral bifurcation. The regions of flow recirculation and low velocities increased during systolic deceleration and peak backflow. The velocity streamlines at all highlighted regions of Figure 4.6 for the standard

simulation and the cases are shown in Appendix B.

TAWSS comparisons

The area of low TAWSS (<0.4 Pa) was similar for all cases of patient 1 for the total segmentation, the AFC (Figure 4.5a) and distal to the bare metal stent (Figure 4.5c). In the proximal AFS (Figure 4.5b), the region of low TAWSS was two times as large for case S3 and almost ten times as large for case S4 compared to the standard simulation of patient 1. The 95th percentile of the TAWSS measured globally and locally was similar for all cases, except for case S1 in the proximal AFS, which was twice as large as the other cases. The percentage of areas with a TAWSS <0.4 Pa and the 95th percentile for the different cases and locations are reported in Table 4.4.

Table 4.4: The distribution of regions of low TAWSS (<0.4 Pa) and the 95th percentile for the standard simulation of patient 1 and cases S1, S2, S3 and S4. The distribution is given for the total segmentation (global), the AFC, the proximal AFS and distal to the bare metal stent.

	Case S1	Case S2	Standard	Case S3	Case S4
Global (%)	3.35	3.49	3.13	3.42	3.65
95th percentile	5.73	5.35	5.59	5.61	5.62
AFC (%)	10.49	9.68	9.37	10.85	9.38
95th percentile	5.26	4.63	4.31	5.24	4.55
Proximal AFS (%)	1.72	2.44	1.28	3.93	10.13
95th percentile	13.00	6.78	6.33	5.70	5.52
Distal to stent (%)	10.06	10.16	9.33	10.14	10.57
95th percentile	3.80	3.92	4.07	4.09	4.22

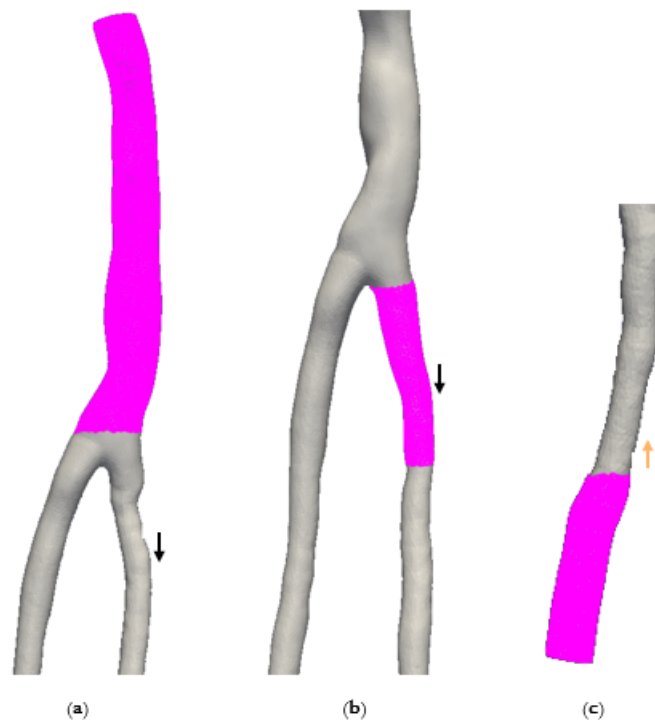


Figure 4.5: The selected regions in the AFC (a), the proximal AFS (b) and distal to the bare metal stent (c) to determine the local percentage TAWSS < 0.4 Pa. The arrows indicate the radiopaque stent marker and the direction of the stent graft.

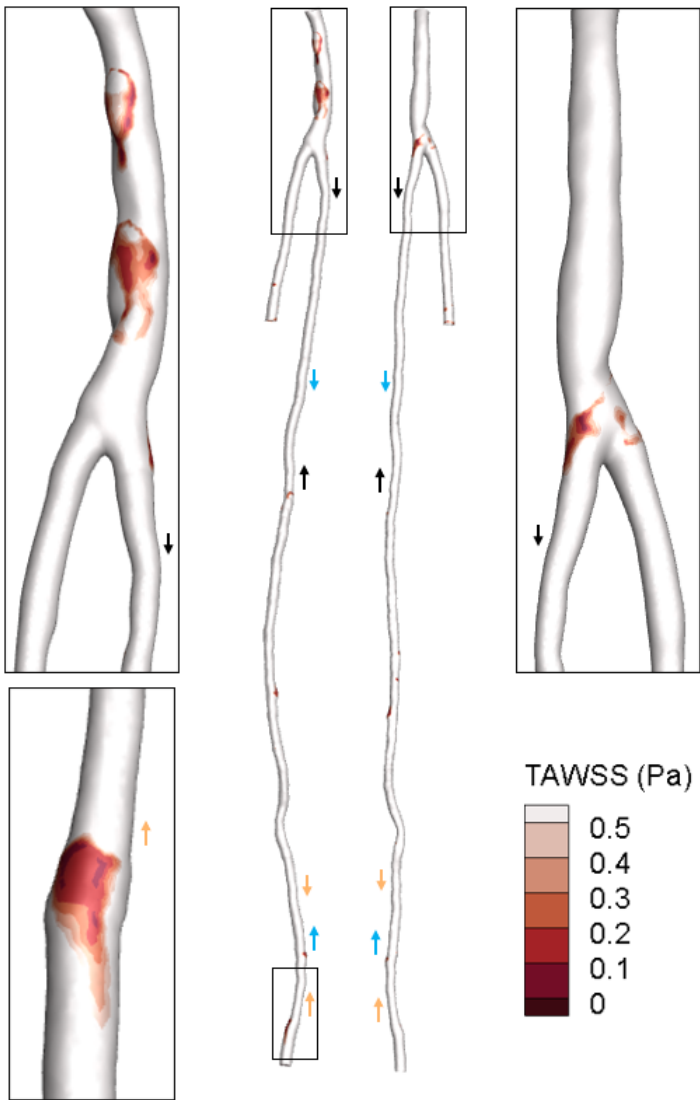


Figure 4.6: The TAWSS over one cardiac cycle for the standard simulation of patient 1. The proximal and distal stent markers of the three stents are indicated with the arrows: black for the proximal Viabahn stent, blue for the distal Viabahn stent and orange for the bare metal stent.

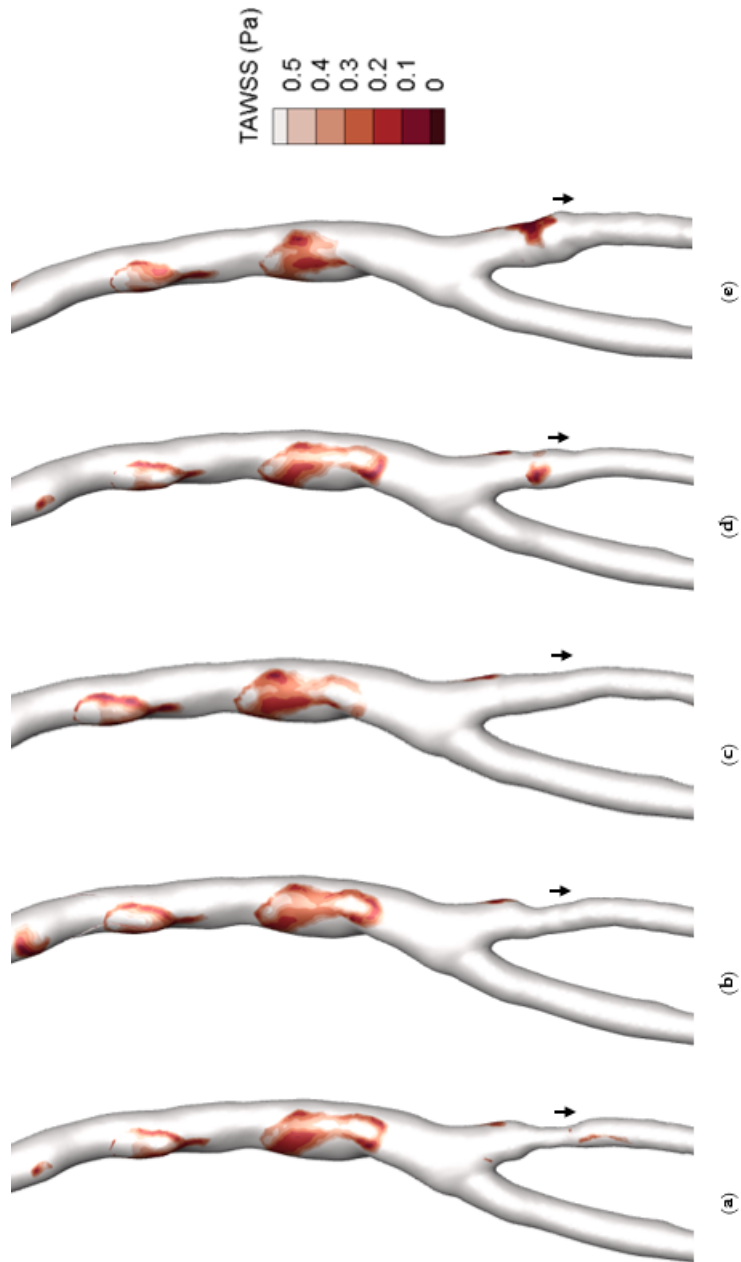


Figure 4.7: The TAWSS over one cardiac cycle in the femoral bifurcation for (a) case S1, (b) case S2, (c) standard simulation of patient 1, (d) case S3 and (e) case S4. The proximal stent marker is indicated with the black arrow.

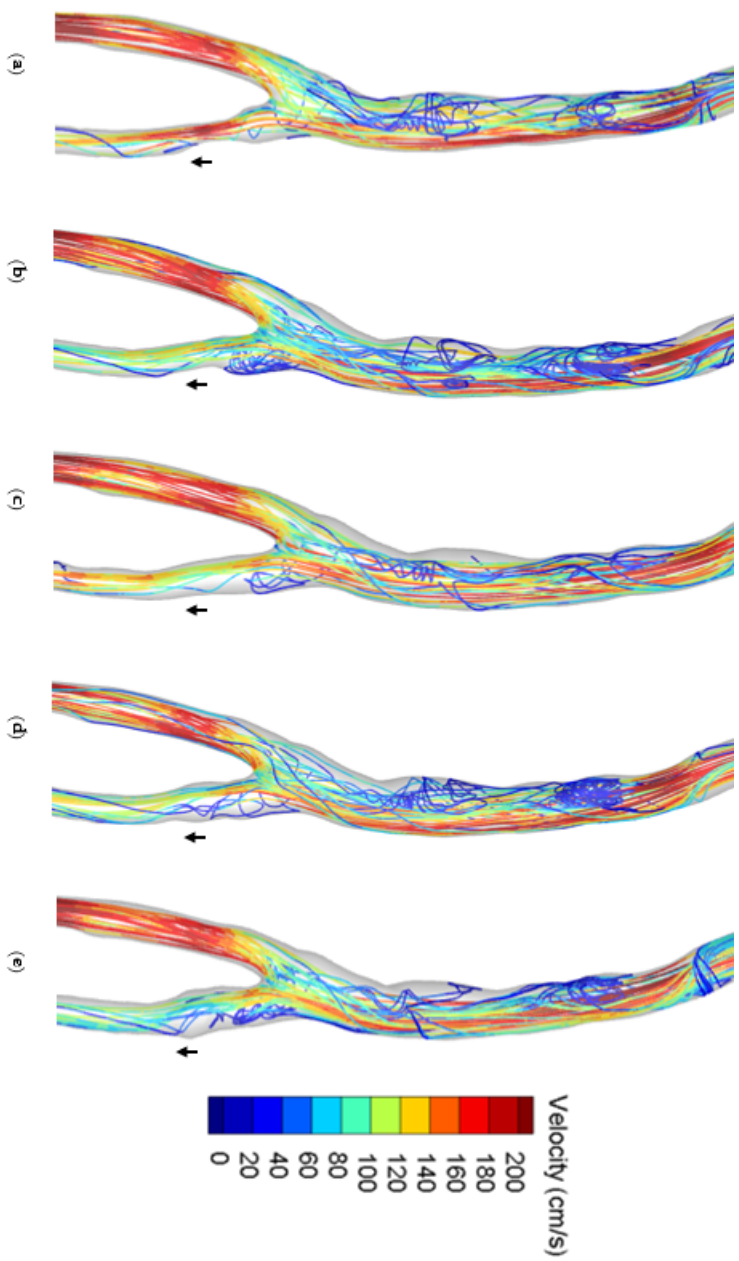


Figure 4.8: Velocity streamlines during peak systole for all cases: (a) case S1, (b) case S2, (c) standard simulation, (d) case S3 and (e) case S4. The proximal stent marker is indicated with the black arrow.

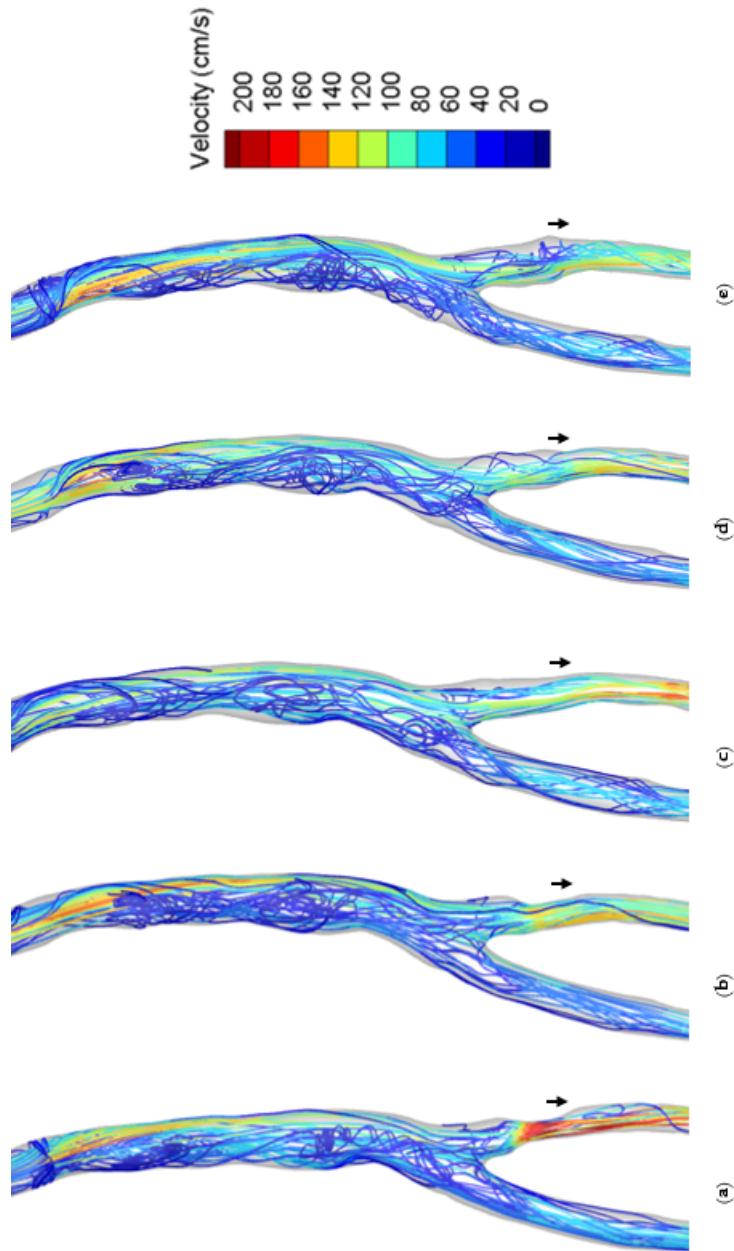


Figure 4.9: Velocity streamlines during systolic deceleration for all cases: (a) case S1, (b) case S2, (c) standard simulation, (d) case S3 and (e) case S4. The proximal stent marker is indicated with the black arrow.

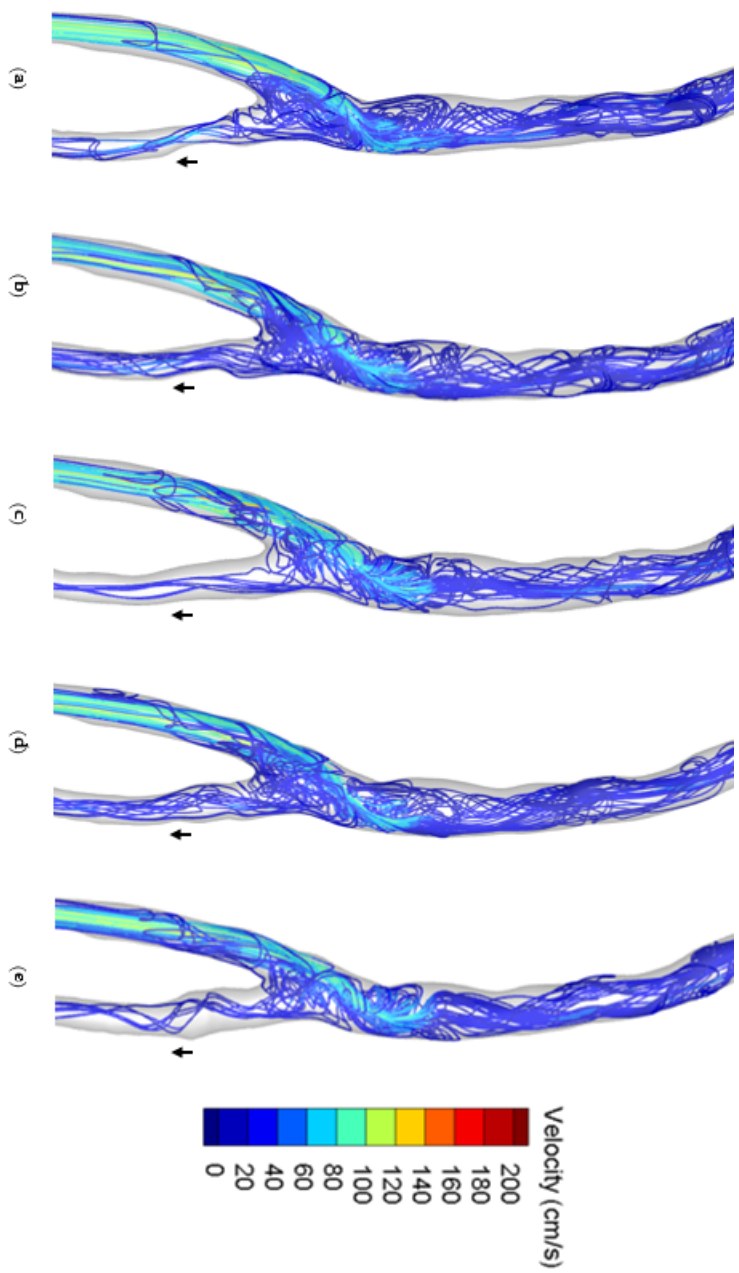


Figure 4.10: Velocity streamlines during peak backflow for all cases: (a) case S1, (b) case S2, (c) standard simulation, (d) case S3 and (e) case S4. The proximal stent marker is indicated with the black arrow.

Uncertainty quantification - inlet velocity profile

The segmentation and TAWSS over one cardiac cycle for patient 2 with Womersley inlet velocity profile are shown in Figure 4.12. All femoral arteries showed diameter changes due to plaques. Segmentation of the AFP, approximately 3 cm distal from the bifurcation, was not possible due to a major narrowing of the vessel lumen. The AFP was extended manually to still be able to simulate a fully developed flow in the AFP. Regions of low TAWSS were seen in the AFC, proximal in the AFP, proximal in the AFS and downstream of the AFS around diameter changes and stent struts and distal to the distal stent. The TAWSS over one cardiac cycle around the femoral bifurcation for all simulations of patient 2 is shown in Figure 4.13. The areas of low TAWSS increased when comparing the new Womersley (Figure 4.13b) and the echo PIV simulation (Figure 4.13c) to the Womersley simulation (Figure 4.13a). The distribution of low TAWSS in the new Womersley simulation and the echo PIV simulation was similar in the proximal AFS and differed in the AFC. The total geometry and TAWSS for the new Womersley and echo PIV simulation are shown in Appendix C.

The velocity streamlines for all cases of patient 2 are visualized during peak systole (Figure 4.14), systolic deceleration (Figure 4.15) and peak backflow (Figure 4.16). The differences in velocity magnitude between the Womersley simulation on the one hand and the new Womersley simulation and the echo PIV simulation on the other hand is striking. The Womersley simulation reaches a velocity of 120 cm/s in the AFC and the other simulations a velocity of approximately 80 cm/s. During peak systole in the Womersley simulation high velocities entered the inner side of the bifurcation and flowed further into the AFP and AFS at the inner side of the bifurcation. In the proximal AFS flow recirculations developed at the outer side of the bifurcation. A similar flow pattern was seen during systolic deceleration in the Womersley simulation, but also in the new Womersley simulation and the echo PIV simulation. Furthermore, areas of flow recirculations increased in all cases, and especially in the echo PIV simulation at the right side of the AFC. During peak backflow more flow recirculations and lower velocities were observed. The velocity streamlines around the bifurcation visualized in another direction for the different simulations are shown in Appendix C

TAWSS comparisons

The areas of low TAWSS increased by a factor of at least two in all locations when comparing the new Womersley simulation and the echo PIV simulation

to the Womersley simulation. Furthermore, the percentage of low TAWSS was higher in the new Womersley simulation compared to the echo PIV simulation in the AFC (Figure 4.11a), but similar in the AFS (Figure 4.11b). The 95th percentile for the Womersley simulation was higher than the other simulations in all locations. The percentage of areas with a low TAWSS and the 95th percentile for the different simulations and locations are reported in Table 4.5.

Table 4.5: The distribution of regions of low TAWSS (<0.4 Pa) and the 95th percentile for the Womersley, Womersley based on echo PIV flow rate and echo PIV simulation of patient 2. The distribution is given for the total segmentation (global), the AFC and the proximal AFS.

	Womersley	New Womersley	echo PIV
Global (%)	8.61	21.4	18.3
95th percentile	6.86	2.62	2.79
AFC (%)	15.2	48.1	33.7
95th percentile	4.92	1.59	1.81
Proximal AFS (%)	15.9	39.2	37.7
95th percentile	4.41	1.40	1.59

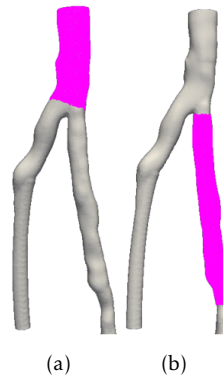


Figure 4.11: The selected regions in the AFC (a) and the proximal AFS (b) to determine the local percentage TAWSS <0.4 Pa.

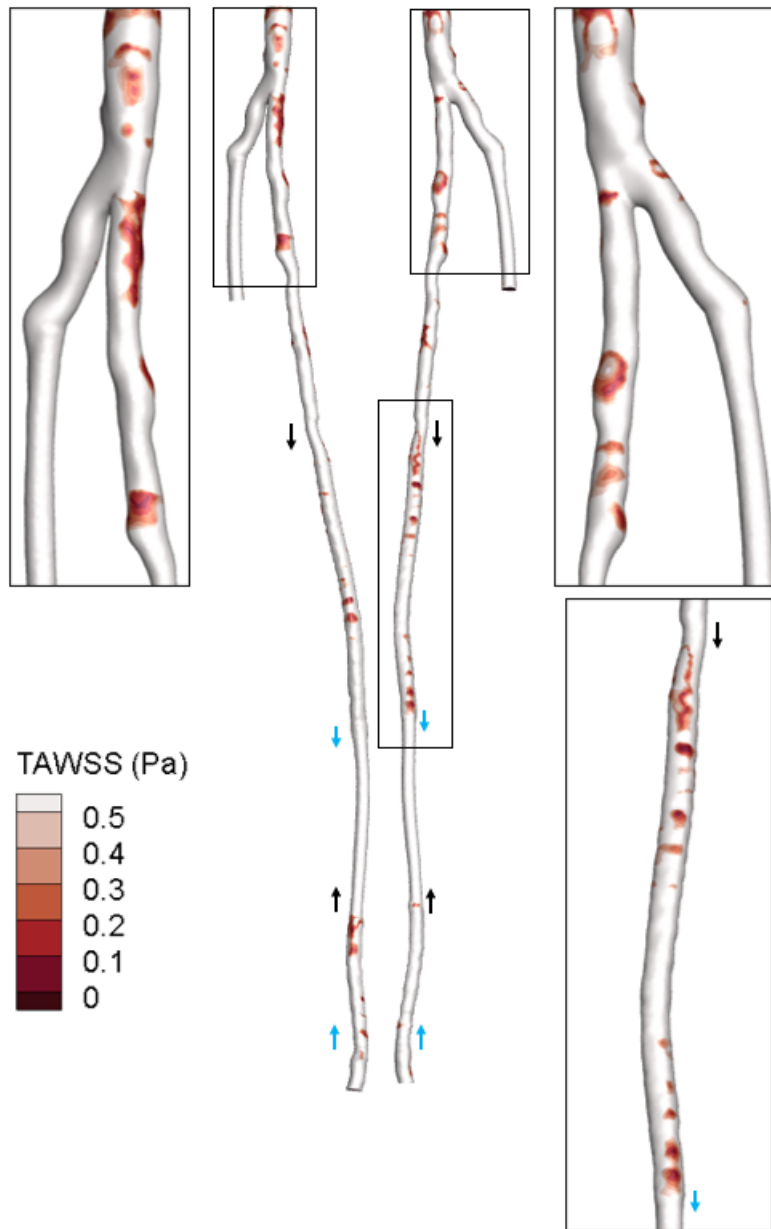


Figure 4.12: The TAWSS over one cardiac cycle for patient 2 using a Womersley inlet velocity profile. The proximal and distal stent markers and the direction of the stents are indicated with the arrows: black for the proximal Everflex stent and blue for the distal Everflex stent.

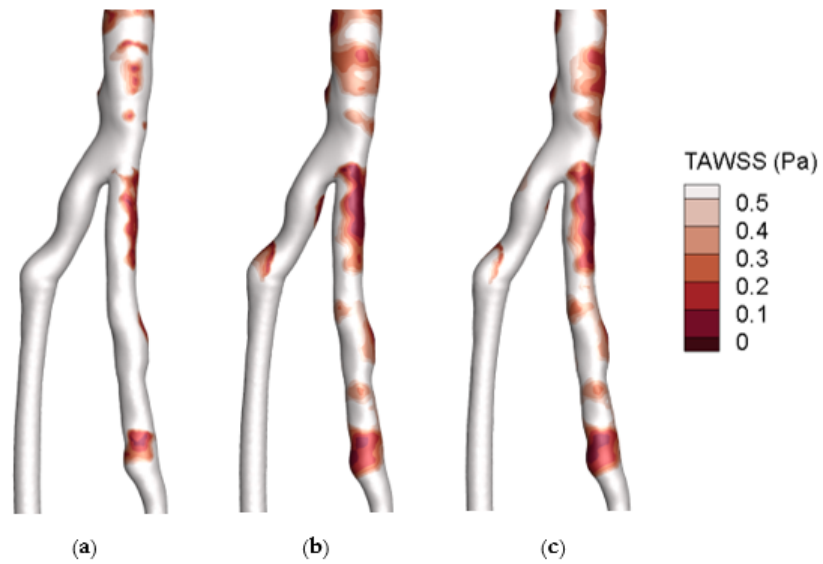


Figure 4.13: The TAWSS over one cardiac cycle in the femoral bifurcation for patient 2: (a) Womersley, (b) new Womersley and (c) echo PIV.

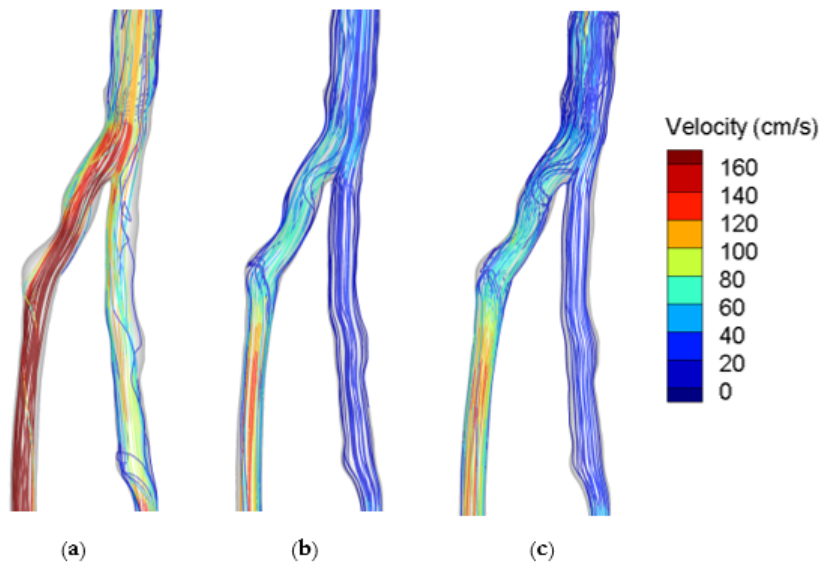


Figure 4.14: Velocity streamlines during peak systole for patient 2: (a) Womersley, (b) new Womersley and (c) echo PIV.

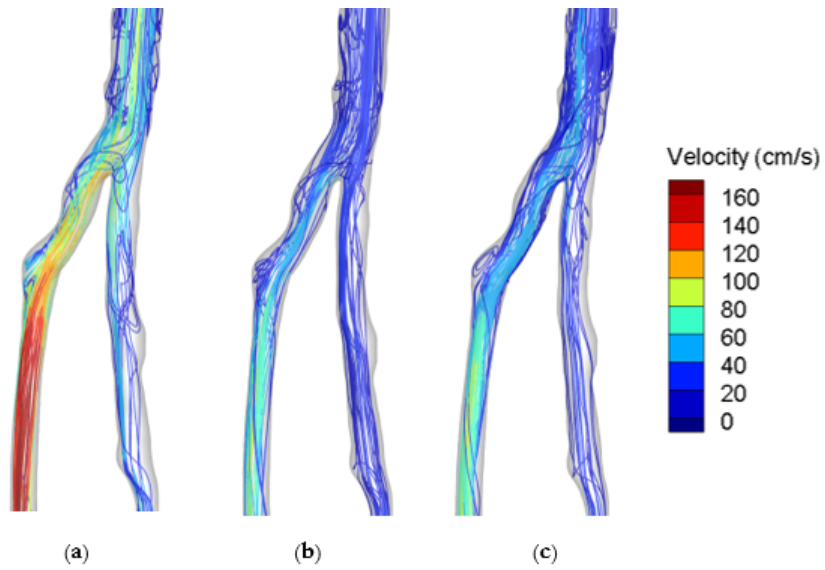


Figure 4.15: Velocity streamlines during systolic deceleration for patient 2: (a) Womersley, (b) new Womersley and (c) echo PIV.

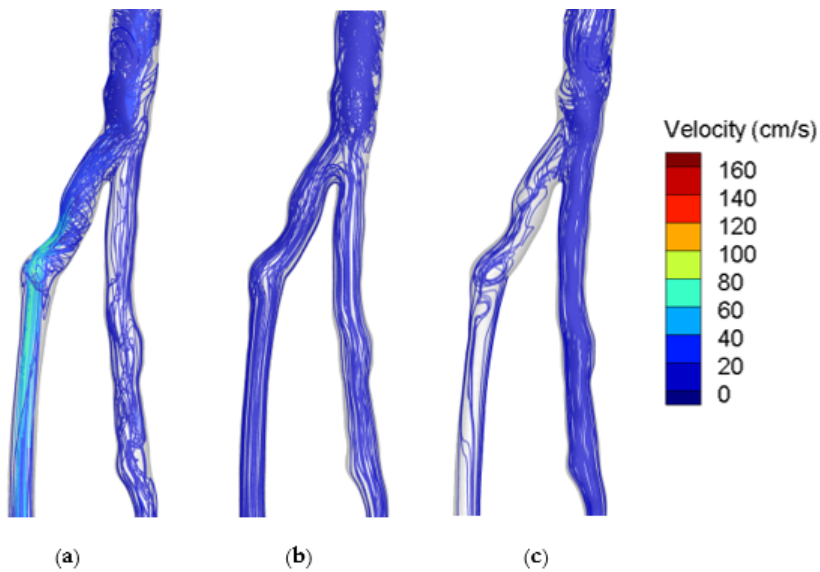


Figure 4.16: Velocity streamlines during peak backflow for patient 2: (a) Womersley, (b) new Womersley and (c) echo PIV.

4.4 Discussion

The goal of this study was to investigate the effect of uncertainty in the geometry and inlet velocity profile on the CFD solution. Uncertainty in the geometry was induced by varying the vessel diameter at the first proximal radiopaque stent marker. As inlet boundary condition, a Womersley velocity profile with a DUS based flow rate, a Womersley velocity profile with an echo PIV based flow rate and an echo PIV velocity profile with an echo PIV based flow rate were compared.

Uncertainty in geometry

Varying the vessel diameter at the proximal stent marker of the proximal stent did influence the magnitude and distribution of the TAWSS. However, this influence was only seen around the proximal marker of the proximal stent. The percentage of regions of low TAWSS (<0.4 Pa) were similar between the cases for the global, AFC and distal to distal stent calculations. Significant differences were seen in the proximal AFS. The percentage of low TAWSS was higher for all cases compared to the standard simulation of patient 1. The region of low TAWSS was three and ten times as large for case S3 and case S4, respectively, when comparing to the standard simulation. The local differences caused by varying the vessel diameter at the proximal stent marker were also visible in the TAWSS and velocity streamlines plots. In both overestimation cases (S3 and S4) an increased region of low TAWSS was observed proximal to the vessel enlargement at the proximal stent marker. It was seen that the higher velocities in the AFC entered the inner side of the bifurcation, causing the higher velocities to enter the AFS at the inner side of the bifurcation. These higher velocities moved into the vessel enlargement, causing a flow split: the higher velocities flowed further downstream of the AFS and flow recirculations developed proximal to the vessel enlargement. As the proximal AFS at the inner side of the bifurcation was smoother in the standard simulation of patient 1 and in the underestimation cases (S1 and S2), this flow split was not seen in these cases. High velocities of 160 - 200 cm/s were seen in the vessel narrowing at the proximal stent marker of case S1. Due to a flow deceleration distal to the vessel narrowing, flow recirculations developed distal to the vessel narrowing. The regions with low velocities and flow recirculations, thus, corresponded to the regions of low TAWSS.

Although the changes in blood flow patterns were limited to the area around the proximal stent marker, these locally changed blood flow patterns could be of great importance when CFD is used in clinical care. Regions of low TAWSS are associated with the development and progression of atherosclero-

sis, which could eventually result in PAD. [13] To be able to use the simulated TAWSS and blood flow patterns to predict the progression of PAD and stent failure or determine the optimal treatment and/or follow-up, the CFD solution should be reliable. In this study, especially the difference in CFD solution in the proximal AFS between the standard simulation and case S4 was striking as the region of low TAWSS increased by a factor of ten. This could result in a different clinical decision. However, as mention before, case S1 and case S4 are extreme cases and case S2 and case S3 represent the possible deviations in a patient-specific geometry better. The regions of low TAWSS in the AFS increased by a factor of two and three for cases S2 and S3, respectively. Furthermore, the TAWSS for the global calculation differed approximately 10% from the standard simulation. This value is lower than found by Thomas et al. (2003) [77] who studied the reproducibility of image-based CFD and discovered a difference of approximately 37% in the TAWSS due to geometric differences. The discrepancy between the results could arise from the induced differences between the studied geometries. In this study, uncertainty in the geometry was only induced at the proximal stent marker of the proximal stent and the other parts of the geometry were identical. In the study by Thomas, seven geometries were created based on different scan settings. It is likely that the scan settings influenced the total geometry, instead of locally as in this study, which could explain the higher difference found by Thomas. Whether the local differences in TAWSS found in cases S2 and S3 are significant to result in a different clinical decision could not be concluded from this study.

Uncertainty in inlet boundary condition

For the uncertainty in inlet boundary condition, two parameters were changed: the velocity profile and the flow rate. The effect of the flow rate on the CFD solution was evident. The percentage of the region of low TAWSS for the new Womersley simulation, based on the lower echo PIV flow rate, was 21.4%, while the percentage for the Womersley simulation was 8.61%. The distribution of the regions of low TAWSS was similar for both simulations, but the regions grew for the new Womersley simulation. Furthermore, lower velocities were seen in the new Womersley simulation compared to the Womersley simulation. During peak systole, this resulted in different flow patterns in the AFS. In the Womersley simulation, the higher velocities entered the inner side of the bifurcation, causing flow separation in the proximal AFS. Higher velocities moved further through the AFS and flow recirculations developed in the proximal AFS at the outer side of the bifurcation. In the new Womersley simulation, the flow in the proximal AFS was more structured. During systolic deceleration a similar flow separation was also seen in the new Wom-

ersley simulation. Based on these simulations it could be concluded that the flow rate affects the CFD solution globally by influencing flow patterns and the WSS magnitude.

Differences in inlet velocity profile affected the CFD solution as the TAWSS magnitude and distribution differed. The differences in TAWSS were mostly seen in the AFC. The percentage of low TAWSS was higher in the new Womersley simulation (49.1%) compared to the echo PIV simulation (33.7%). Furthermore, the distribution of these regions differed between the cases: in the echo PIV simulation a large region of low TAWSS was visible at the right side of the AFC, which was not seen in the new Womersley simulation. Differences were also observed during systolic deceleration. Low velocities in the AFC were seen in both simulations, but the regions of flow recirculation differed. In the echo PIV simulation, a large region of flow recirculation at the right side of the AFC was seen, while flow recirculations in the new Womersley circulation were localized at the left side of the AFC. The differences in the AFS between both cases were minimal. The percentage of low TAWSS in the new Womersley simulation was higher than the echo PIV simulation, 39.2% compared to 37.7%, but this difference was not significant. Furthermore, when comparing the TAWSS magnitude and distribution, and velocity streamlines in the proximal AFS, no clear differences were visible. The results of these simulations, therefore, imply that the influence of the inlet velocity profile is limited to the AFC.

When comparing the effect of the flow rate and inlet velocity profile on the CFD solution, these results imply that the flow rate affects the CFD solution more. The global difference caused by a difference in flow rate was 250%, while the difference caused by the inlet velocity profile were 14.5%. Campbell et al. (2012) [78], who studied the effect of inlet velocity profiles on CFD simulations, also found that the flow rate influenced the CFD solution more than the inlet velocity profile. They also stated that the impact of the geometry on the CFD solution is larger than the influence of the inlet velocity profile. The results of this study do not enhance this statement, as the effect of the geometry in this study was 10% compared to an effect of 14.5% caused by the inlet velocity profile. Furthermore, different patients were used for the geometry and inlet velocity profile analysis and the results of these analyses are, therefore, hard to compare as the different patient-specific geometries and flow rates influence the results found in this study. Based on the results of this study, it cannot be concluded whether the differences in flow rate and inlet velocity profile affect the clinical decision. However, it is implied that the flow rate affects the CFD solution globally, which could make it more difficult

to detect rightly simulated regions of low TAWSS when using a non patient-specific flow rate.

Limitations

An important limitation in this study is the number of patients and cases simulated. As mentioned before two patients were studied, but only one per main analyses: uncertainty in geometry and uncertainty in inlet velocity profile. The effect of uncertainty in geometry and inlet velocity profile observed in this study could be patient-specific and drawing thorough conclusions based on these results is, therefore, difficult. Selecting two to four more patients with different geometries (difference in amount of calcification, bifurcation angle and stent placement) and different velocity profiles and flow rates could overcome this limitation. Furthermore, the cases simulated in this study were limited. In this study only uncertainty in one stent marker was analyzed while more stent markers were present in the CTA image and could affect the segmentation. The overall effect of the radiopaque stent markers on the CFD solution could be underestimated. Simulating uncertainty in different stent markers in one simulation could provide more insight in the total effect of uncertainty in geometry caused by the blooming artifact.

Another limitation is the limited quality of the echo PIV data. The echo PIV data of patient 1 only contained two to four data points per axial slice, thereby only covering a quarter to a half of the axial slice. Retrieving a full inlet velocity profile without many assumptions was, therefore, not possible. Furthermore, large differences in the flow rates obtained with the DUS and echo PIV measurements were observed (factor of two during peak systole). As seen in this study, the CFD solution is sensitive to changes in the flow rate. It is, therefore, important to use a flow rate closest to the patient's true flow rate. Further research is needed to understand the differences in flow rate between the two measurements and determine the optimal flow rate for the patient-specific simulation. Moreover, the original echo PIV data was noisy, probably due to limited bubble visibility causing the velocity vectors to be wrongly determined. Especially the drop in the flow rate at 0.08 s seems to be a measurement error and smoothing of the data could be necessary. In this study, temporal smoothing of the original echo PIV velocity data was not adequate, since the drop at 0.08 s was still present in the smoothed flow rate data. Spatial smoothing and smoothing of the angles of the velocity vectors could possibly result in smoother flow rate data. However, it is important to maintain a flow rate close to the patient-specific flow rate as because of smoothing the flow rate during peak systole decreases, which influences the CFD solution.

Future perspectives

For future research it would be recommended to further study the effect of uncertainty in geometry and inlet boundary condition as well as other input parameters. Furthermore, a study comparing the CFD solutions before and after intervention using different velocity profiles could provide more insight in whether it is necessary to simulate the patient's true velocity profile to observe the effect of an intervention. If, for example, the difference in CFD solution between before and after intervention using a Womersley and echo PIV velocity profile is similar, using a patient-specific velocity profile may not be necessary to demonstrate the effect of the intervention. Moreover, this study could not conclude whether the differences in CFD solution due to uncertainty in geometry and inlet velocity profile would result in a different clinical decision. To be able to do this, boundaries in which the differences in CFD solution are clinically acceptable, are needed. These boundaries could be obtained by investigating the effect of differences in input parameters on the CFD solution and the clinical decision based on these CFD solutions.

When the effect of the geometry and inlet boundary condition on the CFD solution and clinical decision making are known, the CFD method should be further improved. Adverse effects arising from uncertainty in the geometry need to be prevented by improving the imaging modality or segmentation method. Furthermore, the echo PIV measurements and analysis need to be improved to be able to use echo PIV in a more diverse group of patients and obtain a more reliable flow rate. If these challenges are overcome, the next step would be to investigate the added value of the CFD solution in the clinical care of patients diagnosed with PAD.

4.5 Conclusion

This study showed that uncertainty in geometry near radiopaque stent markers results in local changes in TAWSS magnitude and distribution. The region of low TAWSS in the proximal AFS increased with a factor two for case S2 and factor three for case S3. The global difference compared to the standard simulation was approximately 10%. The largest difference in locally measured TAWSS was found for case S4 (overestimation of the vessel lumen) with an increased region of factor ten. Uncertainty in the inlet velocity profile caused local differences in TAWSS magnitude and distribution in the AFC of 30%, resulting in a global difference of 14.6%. The effect of uncertainty in the flow rate was larger, global difference up to 250%, but only the TAWSS magnitude was affected. To be able to draw thorough conclusions regarding the effect of

CHAPTER 4. UNCERTAINTY QUANTIFICATION

uncertainty in the geometry and inlet boundary condition on the CFD solution, more patients and cases need to be analyzed.

Future perspectives

5

This thesis emphasized the importance of using an appropriate geometry, inlet velocity profile and flow rate as both input parameters influence the CFD solution. Uncertainty in geometry is mainly caused by the quality of the used image reconstruction and segmentation technique. [68] An inadequate image resolution (pixel size and slice thickness) increases the partial volume averaging effect and thus the blooming artifact, as was seen in the in-vitro study in Chapter 3. Reducing the uncertainty in the geometry by reducing the blooming artifact could be achieved by using OCT instead of CTA. The spatial resolution of OCT is ten times as high as the spatial resolution of CTA, making it possible to distinguish individual stent struts and obtain a more detailed patient-specific geometry. [67] OCT could also be used to investigate the feasibility of using the *active tubes segmentation technique* to correct for the geometric error caused by the proximal/distal radiopaque stent markers, suggested in Chapter 3, by comparing an OCT-based segmentation and CTA-based segmentation with active tubes segmentation. As the feasibility of OCT in the lower extremities is still limited, a study investigating the feasibility of OCT in the femoral arteries should be performed primarily to the applications mentioned above.

The results of this thesis showed the effect of uncertainty in the geometry and inlet boundary condition on the CFD solution, but no thorough conclusions could be drawn regarding the effect of the uncertainty on the clinical decision making. The observed changes in CFD solution could not be categorized as no clear boundaries or decision tree was available. To know whether differences in CFD solution are significant, a study investigating which parameters determine the clinical decision (a region of low TAWSS [<0.4 Pa] is or is not 'at risk') needs to be conducted. However, the TAWSS itself is most likely also an important parameter in the development of PAD, but the added value of TAWSS calculated by CFD in the prediction of PAD has not yet been proven. A study comparing the calculated TAWSS and clinical outcome of patients (presence of restenosis) could provide new insights necessary to create clear boundaries or a decision tree for the CFD solution combining the calculated

TAWSS and possibly other parameters. Follow-up of the patients studied in this research could provide initial results on this matter.

When the CFD method is improved, the CFD solution is reliable and CFD-calculated flow parameters are found to correlate to the development of atherosclerosis, CFD could eventually be used in clinical care. CFD could be used to simulate the effect of stent placement on the blood flow, resulting in patient-specific treatment planning. Furthermore, the risk of developing a restenosis could be predicted, which could influence the follow-up of the patient. Especially when the duration of the CFD process is reduced, CFD could be routinely used in clinical care.

Conclusion

This thesis emphasized the importance of setting appropriate input parameters in the CFD model. Uncertainty in geometry caused by the blooming artifact of stent struts was quantified in an in-vitro model of the AFS. Analysis showed that the blooming artifact showed the largest reduction in the conventional IMR image reconstruction when compared to the iDose and spectral VMI image reconstructions. Uncertainty in the segmented lumen caused by the blooming artifact was most prominent near proximal/distal radiopaque stent markers resulting in an in-stent lumen underestimation of 33%. Uncertainty in the geometry near these markers caused local changes in the CFD solution. Overestimation of the lumen diameter of approximately 33% resulted in an increased region of low TAWSS of a factor ten in the proximal AFS. Over- and underestimation of approximately 16% caused an increased region of low TAWSS of a factor three and two, respectively, in the AFS, resulting in a global difference of approximately 10%. Uncertainty in inlet velocity profile induced local changes in the CFD solution of 30% in the AFC, resulting in a global difference of 14.6%. The effect of uncertainty in the geometry and inlet velocity profile on the global CFD solution were significantly smaller than the effect of the flow rate on the global CFD solution (up to 250%). To be able to draw thorough conclusions regarding the effect of uncertainty in the geometry and inlet boundary condition on the CFD solution, more patients and cases need to be analyzed.

Bibliography

- [1] C.A. Kalbaugh, A. Kucharska-Newton, L. Wruck, J.L. Lund, E. Selvin, K. Matsushita, L.G.S. Bengtson, G. Heiss, and L. Loehr. Peripheral artery disease prevalence and incidence estimated from both outpatient and inpatient settings among medicare fee-for-service beneficiaries in the Atherosclerosis Risk in Communities (ARIC) study. *Journal of the American Heart Association*, 6(5), 2017.
- [2] A. Dua and C.J. Lee. Epidemiology of Peripheral Arterial Disease and Critical Limb Ischemia. *Techniques in Vascular and Interventional Radiology*, 19(2):91–95, 2016.
- [3] T. Zeller. Current state of endovascular treatment of femoro-popliteal artery disease. *Vascular Medicine*, 12:223–234, 2007.
- [4] K. Marmagkiolis, A. Hakeem, N. Choksi, M. Al-Hawwas, M.M.R. Edupuganti, M.A. Leesar, and M. Cilingiroglu. 12-month primary patency rates of contemporary endovascular device therapy for femoro-popliteal occlusive disease in 6,024 patients: Beyond balloon angioplasty. *Catheterization and Cardiovascular Interventions*, 84(4):555–564, 2014.
- [5] M.D. Gerhard-Herman, H.L. Gornik, C. Barrett, N.R. Barshes, M.A. Corriere, D.E. Drachman, L.A. Fleisher, F.G.R. Fowkes, N.M. Hamburg, S. Kinlay, R. Lookstein, S. Misra, and et al. 2016 AHA/ACC Guideline on the Management of Patients With Lower Extremity Peripheral Artery Disease: Executive Summary. *Circulation*, 135:e686–e725, 2017.
- [6] V. Aboyans, J. Ricco, M.E.L. Bartelink, M. Björk, M. Brodmann, T. Cohnert, J. Collet, M. Czerny, M. De Carlo, S. Debus, and Et Al. 2017 ESC Guidelines on the Diagnosis and Treatment of Peripheral Arterial Diseases, in collaboration with the European Society for Vascular Surgery (ESVS). *European Heart Journal*, 39(9):763–816, 2018.
- [7] R. Doshi, K.H. Changal, R. Gupta, J. Shah, K. Patel, R. Desai, P. Meraj, M.A. Syed, and A.M. Sheikh. Comparison of Outcomes and Cost of Endovascular Management Versus Surgical Bypass for the Management of

- Lower Extremities Peripheral Arterial Disease. *American Journal of Cardiology*, 122(10):1790–1796, 2018.
- [8] U. Bildirici, M. Aktas, E. Dervis, and U. Celikyurt. Mid-Term Outcomes of Stent Overlap in Long Total Occluded Lesions of Superficial Femoral Artery. *Medical Science Monitor*, 23:3130–3135, 2017.
- [9] L. Razzouk, S. Aggarwal, F. Gorgani, and A. Babaev. In-Stent Restenosis in the Superficial Femoral Artery. *Annals of Vascular Surgery*, 27(4):510–524, 2013.
- [10] P. Libby, P.M. Ridker, and G.K. Hansson. Progress and challenges in translating the biology of atherosclerosis. *Nature*, 473(7347):317–325, 2011.
- [11] A. Yurdagul, A. Finney, M.D. Woolard, and A.W. Orr. The Arterial Microenvironment: The Where and Why of Atherosclerosis. *Biochemical Journal*, 473(10):1281–1295, 2016.
- [12] K. Cunningham and A. Gotlieb. The role of shear stress in the pathogenesis of atherosclerosis. pages 9–23, 2005.
- [13] W.W. Nichols, M.F. O’Rourke, and C. Vlachopoulos. *McDonald’s Blood Flow in Arteries: Theoretical, experimental and clinical principles*. 2011.
- [14] A. Harloff and M. Markl. In vivo wall shear stress patterns in carotid bifurcations assessed by 4D MRI. *Perspectives in Medicine*, 1(1-12):137–138, 9 2012.
- [15] J. Szajer and K. Ho-Shon. A comparison of 4D flow MRI-derived wall shear stress with computational fluid dynamics methods for intracranial aneurysms and carotid bifurcations — A review. *Magnetic Resonance Imaging*, 48:62–69, 5 2018.
- [16] M. Markl, W. Wallis, and A. Harloff. Reproducibility of flow and wall shear stress analysis using flow-sensitive four-dimensional MRI. *Journal of Magnetic Resonance Imaging*, 33(4):988–994, 2011.
- [17] W.V. Potters, P. van Ooij, H. Marquering, E. VanBavel, and A.J. Nederveen. Volumetric arterial wall shear stress calculation based on cine phase contrast MRI. *Journal of Magnetic Resonance Imaging*, 41(2):505–516, 2014.
- [18] P. Gates, A. Gurung, L. Mazzaro, K. Aizawa, S. Elyas, W. Strain, A. Shore, and R. Shandas. Measurement of Wall Shear Stress Exerted by Flowing Blood in the Human Carotid Artery: Ultrasound Doppler Velocimetry

BIBLIOGRAPHY

- and Echo Particle Image Velocimetry. *Ultrasound in Medicine & Biology*, 44(7):1392–1401, 7 2018.
- [19] N. Paliwal, R.J. Damiano, N.A. Varble, and V.M. Tutino. Methodology for Computational Fluid Dynamic Validation for Medical Use : Application to Intracranial Aneurysm. *Journal of Bio*, 139(December), 2017.
- [20] E.R. Mohler and M.R. Jaff. *Peripheral Artery Disease*. Wiley, Hoboken, 2nd edition, 2017.
- [21] S.M. Conte and P.R. Vale. Peripheral Arterial Disease. *Heart, Lung and Circulation*, 27(4):427–432, 2018.
- [22] L. Portier, C. Abi Khalil, K. Mohameddi, and R. Roussel. Use and Utility of Ankle Brachial Index in Patients with Diabetes. *Eur J Vasc Endovasc Surg*, 41:110–116, 2011.
- [23] J.W. Olin, C.J. White, E.J. Armstrong, D. Kadian-Dodov, and W.R. Hiatt. Peripheral Artery Disease. *Journal of the American College of Cardiology*, 67(11):1338–1357, 2016.
- [24] R.W. Sprengers, K.J.M. Janssen, F.L. Moll, M.C. Verhaar, and Y. van der Graaf. Prediction rule for cardiovascular events and mortality in peripheral arterial disease patients: Data from the prospective Second Manifestation of ARterial disease (SMART) cohort study. *Journal of Vascular Surgery*, 50:1369–77, 2009.
- [25] M.M.P.J. Reijnen, L.A. van Walraven, W.M. Fritschy, M.M.A. Lensvelt, C.J. Zeebregts, M.S. Lemson, O.R.M. Wikkeling, L. Smeets, and S. Holewijn. 1-Year Results of a Multicenter Randomized Controlled Trial Comparing Heparin-Bonded Endoluminal to Femoropopliteal Bypass. *Jacc-Cardiovascular interventions*, 10(22):2320–2331, 2017.
- [26] M.R. Jaff, C.J. White, W.R. Hiatt, G.R. Fowkes, J. Dormandy, M. Razavi, J. Reekers, and L. Norgren. An Update on Methods for Revascularization and Expansion of the TASC Lesion Classification to Include Below-the-Knee Arteries: A Supplement to the Inter-Society Consensus for the Management of Peripheral Arterial Disease (TASC II). *Journal of Endovascular Therapy*, 22:657–671, 2015.
- [27] L. Garcia, M.R. Jaff, C. Metzger, G. Sedillo, A. Pershad, F. Zidar, R. Patlola, R.G. Wilkins, A. Espinoza, A. Iskander, G.S. Khammar, Y. Khatib, R. Beasley, S. Makam, R. Kovach, S. Kamat, L.R. Leon, W.R. Eaves, J.J.

- Popma, L. Mauri, D. Donohoe, C.C. Base, and K. Rosenfield. Wire-Interwoven Nitinol Stent Outcome in the Superficial Femoral and Proximal Popliteal Arteries: Twelve-Month Results of the SUPERB Trial. *Circulation: Cardiovascular Interventions*, 8(5):1–8, 2015.
- [28] J.W. Groenendyk and N.N. Mehta. Applying the ordinal model of atherosclerosis to imaging science: a brief review. *Open Heart*, 5:e000861, 2018.
- [29] J. Chi, B. Chiu, X. Liu, J. Wang, N. Balu, C. Yuan, and J. Xu. Assessment of femoral artery atherosclerosis at the adductor canal using 3D black-blood MRI. *Clinical Radiology*, 68:213–221, 2013.
- [30] J. Blair, S. Glagov, and C. Zarins. Mechanism of superficial femoral artery abductor canal stenosis. *Surg Forum*, 41:359–360, 1990.
- [31] P.W. Tank and J.C.B. Grant. *Dissector*. Lippincott Williams & Wilkins, Philadelphia, 14 edition, 2009.
- [32] S.P. Overeem, J.P.M. de Vries, J.T. Boersen, C.H. Slump, M.M.P.J. Reijnen, M. Versluis, and E. Groot Jebbink. Haemodynamics in Different Flow Lumen Configurations of Customised Aortic Repair for Infrarenal Aortic Aneurysms. *European Journal of Vascular and Endovascular Surgery*, 57(5):709–718, 5 2019.
- [33] F. Zhang, C. Lanning, L. Mazzaro, A.J. Barker, P.E. Gates, W.D. Strain, J. Fulford, O.E. Gosling, A.C. Shore, N.G. Bellenger, B. Rech, J. Chen, J. Chen, and R. Shandas. In vitro and preliminary in vivo validation of echo particle image velocimetry in carotid vascular imaging. *Ultrasound in Medicine & Biology*, 37(3):450–464, 2011.
- [34] J. Tu, G. Yeoh, and C. Liu. *Computational Fluid Dynamics: A Practical Approach*. Butterworth-Heinemann, Oxford, 3 edition, 2018.
- [35] S. Moccia, E. De Momi, S. El Hadji, and L.S. Mattos. Blood vessel segmentation algorithms — Review of methods, datasets and evaluation metrics. *Computer Methods and Programs in Biomedicine*, 158:71–91, 2018.
- [36] L. Antiga, M. Piccinelli, L. Botti, B. Ene-Iordache, A. Remuzzi, and D.A. Steinman. An image-based modeling framework for patient-specific computational hemodynamics. *Medical & Biological Engineering & Computing*, 46:1097, 2008.
- [37] J. Tu, K. Inthavong, and K. Wong. Generation of Computational Mesh for Haemodynamics Analysis. In *Computational Hemodynamics - Theory, Modelling and Applications*, pages 155–181. Springer, Dordrecht, 2015.

BIBLIOGRAPHY

- [38] F. Moukalled, L. Mangani, and M. Darwish. The Finite Volume Mesh. In *The Finite Volume Method in Computational Fluid Dynamics. Fluid Mechanics and Its Applications*, pages 137–171. Springer, Cham, 2016.
- [39] S. Pirola, Z. Cheng, O.A. Jarral, D.P. O’Regan, J.R. Pepper, T. Athanasiou, and X.Y. Xu. On the choice of outlet boundary conditions for patient-specific analysis of aortic flow using computational fluid dynamics. *Journal of Biomechanics*, 60:15–21, 7 2017.
- [40] P. Xu, X. Liu, H. Zhang, D. Ghista, D. Zhang, C. Shi, and W. Huang. Assessment of boundary conditions for CFD simulation in human carotid artery. *Biomechanics and Modeling in Mechanobiology*, 17(6):1–17, 2018.
- [41] P.M. McGah, J.D. Nerva, R.P. Morton, M.C. Barbour, M.R. Levitt, P.D. Mourad, L.J. Kim, and A. Aliseda. In Vitro Validation of Endovascular Doppler-derived Flow Rates in Models of the Cerebral Circulation. *Physiological Measurement*, 36(11):2301–2317, 2015.
- [42] V.M. Pereira, O. Brina, A. Marcos Gonzales, A.P. Narata, P. Bijlenga, K. Schaller, K.O. Lovblad, and R. Ouared. Evaluation of the influence of inlet boundary conditions on computational fluid dynamics for intracranial aneurysms: A virtual experiment. *Journal of Biomechanics*, 46(9):1531–1539, 5 2013.
- [43] C.H. Leow, E. Bazigou, R.J. Eckersley, A.C.H. Yu, P.D. Weinberg, and M.X. Tang. Flow velocity mapping using contrast enhanced high-frame-rate plane wave ultrasound and image tracking: Methods and initial in vitro and in vivo evaluation. *Ultrasound in Medicine and Biology*, 41(11):2913–2925, 2015.
- [44] U. Morbiducci, D. Gallo, D. Massai, F. Consolo, R. Ponzini, L. Antiga, C. Bignardi, M.A. Deriu, and A. Redaelli. Outflow conditions for image-based hemodynamic models of the carotid bifurcation: Implications for indicators of abnormal flow. *Journal of Biomechanical Engineering*, 132(9):1–11, 2010.
- [45] I.E. Vignon-Clementel, C.A. Figueroa, K.E. Jansen, and C.A. Taylor. Outflow boundary conditions for 3D simulations of non-periodic blood flow and pressure fields in deformable arteries. *Computer Methods in Biomechanics and Biomedical Engineering*, 13(5):625–640, 2010.
- [46] A. Boccadifuoco, A. Mariotti, S. Celi, N. Martini, and M.V. Salvetti. Impact of uncertainties in outflow boundary conditions on the predictions of hemodynamic simulations of ascending thoracic aortic aneurysms. *Computers & Fluids*, 165:96–115, 3 2018.

-
- [47] N. Westerhof, F. Bosman, C.J. De Vries, and A. Noordergraaf. Analog studies of the human systemic arterial tree. *Journal of Biomechanics*, 2(2):121–143, 1969.
- [48] S. Park, S. Lee, O.K. Lim, I. Min, M. Nguyen, Y.B. Ko, K. Yoon, and D.C. Suh. Computational Modeling with Fluid-Structure Interaction of the Severe M1 Stenosis Before and After Stenting. *Neurointervention*, 8(1):23, 2013.
- [49] P.K. Siogkas, A.I. Sakellarios, T.P. Exarchos, K. Stefanou, D.I. Fotiadis, K. Naka, L. Michalis, N. Filipovic, and O. Parodi. Blood flow in arterial segments: rigid vs. deformable walls simulations. *Journal of the Serbian Society for Computational Mechanics*, 5(1):69–77, 2011.
- [50] A.R. Pries, D. Neuhaus, and P. Gaehtgens. Blood viscosity in tube flow: dependence on diameter and hematocrit. *American journal of physiology. Regulatory, integrative and comparative physiology*, 263(6 Pt 2):1770–8, 1992.
- [51] H. Gharahi, B. Zambrano, D. Zhu, J. Demarco, S. Baek, and E. Lansing. measured with magnetic resonance imaging. 8(1):40–60, 2017.
- [52] G.K. Batchelor. The effect of Brownian motion on the bulk stress in a suspension of spherical particles. *Journal of Fluid Mechanics*, 83:97–117, 1977.
- [53] R.D. Cook, D.S. Malkus, M.E. Plesha, and R.J. Witt. Introduction. In *Concepts and applications of finite element analysis*, pages 1–4. John Wiley & Sons, Hoboken, 4 edition, 2002.
- [54] E. Seeram. *Computed Tomography: Physical Principles, Clinical Applications and Quality Control*. Elsevier Health Sciences, Amsterdam, 2015.
- [55] D. Mukherjee and S. Rajagopalan. *CT and MR Angiography of the Peripheral Circulation: Practical Approach with Clinical Protocols*. CRC Press, Boca Raton, 2007.
- [56] C. Yuan, T.S. Hatsukami, and M. Mossa-Basha. *Vessel Based Imaging Techniques: Diagnosis, Treatment, and Prevention*. Springer Nature, New York City, 2019.
- [57] P. Li, L. Yang, R. Wang, J. Hsieh, Z. Sun, Z. Fan, and J.A. Leipsic. Blooming Artifact Reduction in Coronary Artery Calcification by A New Deblooming Algorithm: Initial Study. *Nature*, 8, 2018.
- [58] A.H. Mahnken. CT Imaging of Coronary Stents: Past, Present, and Future. *ISRN Cardiology*, 2012.

BIBLIOGRAPHY

- [59] M. Köhler, M.C. Burg, A.C. Bunck, W. Heindel, H. Seifarth, and D. Maintz. Dual-Source CT Angiography of Peripheral Arterial Stents: In Vitro Evaluation of 22 Different Stent Types. *Radiology Research and Practice*, 2011:7, 2011.
- [60] M. Kaempf, D. Ketelsen, R. Syha, S. Sixt, S. Mangold, C. Thomas, C.D. Claussen, M. Heuschmid, and K. Brechtel. CT angiography of various superficial femoral artery stents: An in vitro phantom study. *European Journal of Radiology*, 81:1584 – 1588, 2012.
- [61] J. Boos, P. Kröpil, R.S. Lanzman, J. Aissa, C. Schleich, G. Antoch, and C. Thomas. Stent Lumen Visibility in Single-energy CT Angiography: Does Tube Potential Matter? *Academic Radiology*, 23(6):752–759, 2016.
- [62] E. Coche. Spectral CT Clinical Case Collection, 2019.
- [63] N. Rassouli, M. Etesami, A. Dhanantwari, and P. Rajiah. Detector-based spectral CT with a novel dual layer technology: principles and applications. *Insights Imaging*, 8(6):589–598, 2017.
- [64] D. Zhang, Y. Xie, Y. Wang, N. Guo, Y. Wang, Z. Jin, and H. Xue. Initial Clinical Experience of Virtual Monoenergetic Imaging Improves Stent Visualization in Lower Extremity Run-Off CT Angiography by Dual-Layer Spectral Detector CT. *Academic Radiology*, 2010(1):1–8, 2019.
- [65] S. Sudarski, P. Apfaltrer, J.W. Nance, D. Schneider, M. Meyer, S.O. Schoenberg, C. Fink, and T. Henzler. Optimization of keV-settings in abdominal and lower extremity dual-source dual-energy CT angiography determined with virtual monoenergetic imaging. *European Journal of Radiology*, 82(10):e574–e581, 2013.
- [66] E. Halpern, D. Halpern, J. Yanof, S. Amin-Spector, D. Fischman, G. Aviram, and J. Sosna. Is Coronary Stent Assessment Improved with Spectral Analysis of Dual Energy CT? *Academic Radiology*, 16(10):1241–1250, 2009.
- [67] C. Chiastra, S. Migliori, F. Burzotta, G. Dubini, and F. Migliavacca. Patient-specific modeling of stented coronary arteries reconstructed from optical coherence tomography: Towards a widespread clinical use of fluid dynamics analyses. *Journal of Cardiovascular Translational Research*, 11(2):156–172, 2017.
- [68] M. Colombo, M. Bologna, M. Garbey, S. Berceci, Y. He, J. Rodriguez Matas, F. Migliavacca, and C. Chiastra. Computing patient-specific hemodynamics in stented femoral artery models obtained from

- computed tomography using a validated 3D reconstruction method. *Medical Engineering and Physics*, (xxxx), 2019.
- [69] S. Sankaran and A.L. Marsden. A Stochastic Collocation Method for Uncertainty Quantification and Propagation in Cardiovascular Simulations. *Journal of Biomechanical Engineering*, 133(3), 2011.
- [70] D. Nolte and C. Bertoglio. Reducing the impact of geometric errors in flow computations using velocity measurements. *Int J Numer Meth Biomed Engng*, 35, 2019.
- [71] K. Valen-Sendstad and Et Al. Real-World Variability in the Prediction of Intracranial Aneurysm Wall Shear Stress: The 2015 International Aneurysm CFD Challenge. *Cardiovasc Eng Technol*, 9(4):544–564, 2018.
- [72] K.R. Moyle, L. Antiga, and D.A. Steinman. Inlet Conditions for Image-Based CFD Models of the Carotid Bifurcation: Is it Reasonable to Assume Fully Developed Flow? *Journal of Biomechanical Engineering*, 128(3):371, 2006.
- [73] Y. Hoi, B.A. Wasserman, E.G. Lakatta, and D.A. Steinman. Carotid Bifurcation Hemodynamics In Older Adults: Effect Of Measured vs. Assumed Flow Waveform. *Journal of Biomechanical Engineering*, 132(7), 2010.
- [74] A. Marzo, P. Singh, P. Reymond, N. Stergiopoulos, U. Patel, and R. Hose. Influence of inlet boundary conditions on the local haemodynamics of intracranial aneurysms. *Computer Methods in Biomechanics and Biomedical Engineering*, 12(4):431–444, 2009.
- [75] J.G. Myers, J.A. Moore, M. Ojha, K.W. Johnston, and C.R. Ethier. Factors Influencing Blood Flow Patterns in the Human Right Coronary Artery. *Annals of Biomedical Engineering*, 29(2):109–120, 2001.
- [76] A.W. Updegrave, J.L. Merkow, A.L. Marsden, and S.C. Shadden. Simvascular - An open source pipeline for cardiovascular simulation. *Annals of Biomedical Engineering*, 2016.
- [77] J.B. Thomas, J.S. Milner, B.K. Rutt, and D.A. Steinman. Reproducibility of image-based computational fluid dynamics models of the human carotid bifurcation. *Annals of Biomedical Engineering*, 31(2):132–141, 2003.
- [78] I.C. Campbell, J. Ries, S.S. Dhawan, A.A. Quyyumi, W.R. Taylor, and J.N. Oshinski. Effect of Inlet Velocity Profiles on Patient-Specific Computational Fluid Dynamics Simulations of the Carotid Bifurcation. *Journal of Biomechanical Engineering*, 134(5), 2012.

Velocity profile based on echo PIV measurements

The echo PIV measurements were performed in the longitudinal plane, as is shown in Figure A.1. For the echo PIV data to be used as inlet boundary condition in SimVascular, the echo PIV data needed to be translated to a 3D velocity profile in an axial slice. Furthermore, the obtained 3D velocity data needed to be fitted to the grid points used in Simvascular. The steps to achieve these goals are elaborated further in the following sections.

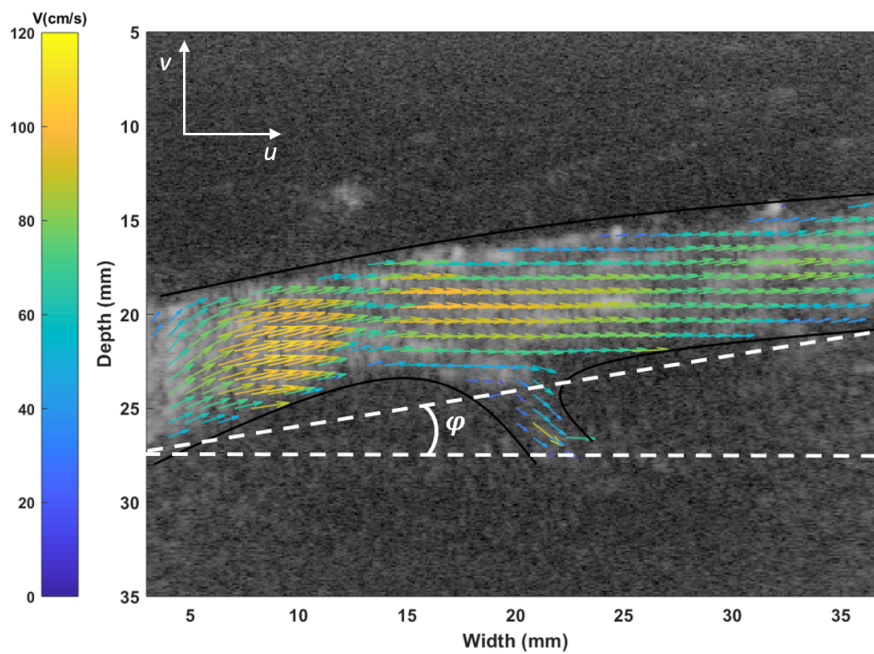


Figure A.1: Velocity vectors in the AFC based on echo PIV measurements.

A.1 Longitudinal to axial echo PIV velocity profile

First, the coordinate system, shown in Figure A.1, was rotated in such a way that u was parallel to the direction of the main velocity component, in this case parallel to the vessel wall. The angle (ϕ) between u and the vessel wall was determined, as is shown in Figure A.1, and the rotated velocity components (u' and v') were calculated using the rotating matrix, shown in Equation A.1.

$$\begin{bmatrix} u' \\ v' \end{bmatrix} = \begin{bmatrix} \cos(\phi) & -\sin(\phi) \\ \sin(\phi) & \cos(\phi) \end{bmatrix} \begin{bmatrix} u \\ v \end{bmatrix} \quad (\text{A.1})$$

Second, the longitudinal velocity data was translated to axial velocity data. One column containing the velocity data of u' and v' (from now on accent is left out) was chosen from the longitudinal velocity data, preferably corresponding anatomically to the segmented inlet. The column was split in the middle, now the center of the blood vessel, into u_0/v_0 and $u_{180}/-v_{180}$. Based on the vector containing the locations of u and v , the vector r , the radius of the blood vessel containing the locations of u_0/v_0 and $u_{180}/-v_{180}$, was determined. Using r and a self-defined angle (θ), the velocity data was rotated and interpolated over 180° in steps of θ : u_0/v_0 to $u_{180}/-v_{180}$ and $u_{180}/-v_{180}$ to u_0/v_0 . An axial velocity profile was the result.

A.2 Echo PIV fitted to grid SimVascular

First, the echo PIV xy-plane was superimposed on the SimVascular xy-plane by translating the center of both planes to xy-coordinate (0,0). The radius of the echo PIV plane was rescaled in such a way that the maximum radius was equal to the smallest radius of the SimVascular plane minus ΔR . The ΔR was added as echo PIV is not able to measure accurately near the vessel wall and the velocity at the vessel wall is always zero. When the echo PIV plane was superimposed on the SimVascular plane, three situations were identified:

1. Grid points at the vessel wall;
2. Grid points within the radius of the echo PIV plane;
3. Grid point between the vessel wall and the radius of the echo PIV plane.

The different situations are visualized in Figure A.3.

APPENDIX A. VELOCITY PROFILE BASED ON ECHO PIV MEASUREMENTS

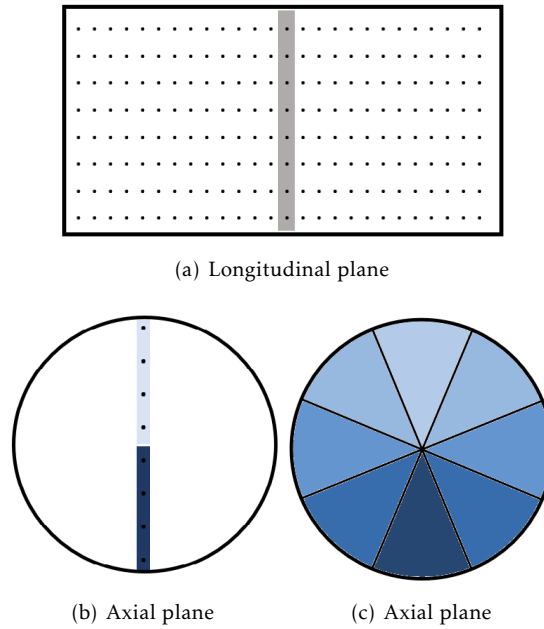


Figure A.2: Process of obtaining an axial velocity field of a longitudinal velocity field. (a) Longitudinal view of a blood vessel. The black dots indicate velocity data and the grey rectangle shows the selected velocity column to rotate. (b) Axial view of a blood vessel. The selected velocity column is shown again, but is divided into two separate columns (dark blue and light blue). (c) Axial view of a blood vessel. The velocity data of the two columns is interpolated over a certain angle (θ), resulting in a velocity field in the axial plane.

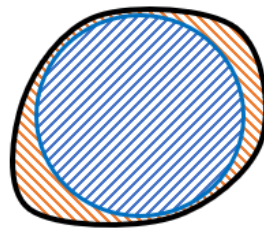


Figure A.3: Axial view of a blood vessel. The black line represents the Sim-Vascular plane and the blue line the echo PIV plane. Three regions can be identified. Grid points at the vessel wall (black line), grid points within radius of the echo PIV plane (blue region) and grid points between the vessel wall and radius of the echo PIV plane (orange region).

The velocity in x-, y- and z-direction for the grid points at the vessel wall was always zero. For the other grid points, bilinear interpolation was used to obtain the velocity components:

$$f(\theta, r) = \frac{1}{(\theta_2 - \theta_1)(r_2 - r_1)} \begin{bmatrix} \theta_2 - \theta & \theta - \theta_1 \end{bmatrix} \begin{bmatrix} f(Q_{11}) & f(Q_{12}) \\ f(Q_{21}) & f(Q_{22}) \end{bmatrix} \begin{bmatrix} r_2 - r \\ r - r_1 \end{bmatrix} \quad (\text{A.2})$$

Δr and $\Delta \theta$ were constant for the grid points within the radius of the echo PIV plane. The rectangle between which the r and θ of the grid point fell (P), shown in Figure A.4, was found and by solving Equation A.2 u and v of the grid point was interpolated.

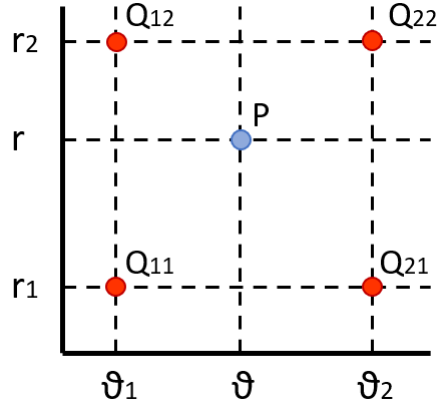


Figure A.4: Bilinear interpolation. The red dots indicate the known data points and the blue dot the unknown data point, obtained with bilinear interpolation.

For the grid points between the echo PIV plane and vessel wall it was harder to perform bilinear interpolation. As the plane of SimVascular, which depends on the patient-specific geometry, was not a perfect circle, Δr was not constant anymore. Therefore, for every grid point between the vessel wall and the echo PIV plane the closest points on the vessel wall were identified and the mean r of these points was calculated. The mean r was then used to create nodes at the desired angles and create the rectangle necessary for bilinear interpolation.

A.3 2D to 3D velocity profile

The obtained 2D velocity profile was translated to a 3D velocity profile in x -, y - and z -direction. The z -axis was perpendicular to the axial plane and was therefore equal to u . v was split into a x - and y -component, calculated using trigonometry. Finally, a 3D echo PIV velocity profile was obtained. This velocity profile did, however, assume that the axial plane was perpendicular to the z -axis defined in SimVascular. The normal of the axial plane was determined, the angle between the normal and the x -axis and y -axis defined by SimVascular was calculated and the velocity vectors were rotated in such a way that the z -axis defined by Simvascular was perpendicular to the axial plane.

A.4 Smoothing

Temporal smoothing was performed on the original echo PIV data points, the grey rectangle in Figure A.2a. Robust local regression was used to remove outliers from the smoothed data. The resulting smoothed magnitude of the velocity vectors of one echo PIV data point is shown in Figure A.5a. The flow rate obtained from the smoothed echo PIV data still showed a drop around 0.08 s, see Figure A.5c. This could result from the fast change in the angle of the velocity vectors of the original echo PIV data around 0.08 s, see Figure A.5b. Another explanation could be that only temporal smoothing and no spatial smoothing was performed

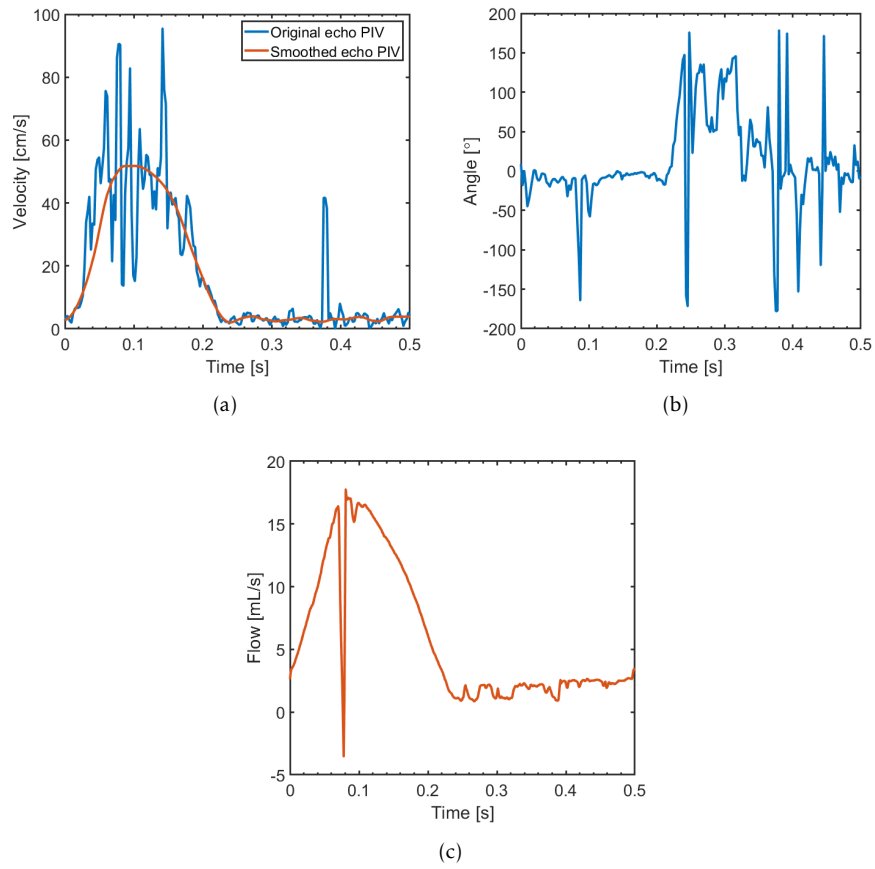


Figure A.5: Smoothing of the echo PIV data. (a) The magnitude of the velocity vector for the original and smoothed echo PIV data. (b) The angle of the velocity vector for the original echo PIV data. (c) The flow rate for the smoothed echo PIV data.

Uncertainty in patient-specific geometry

B.1 Standard simulation of patient 1

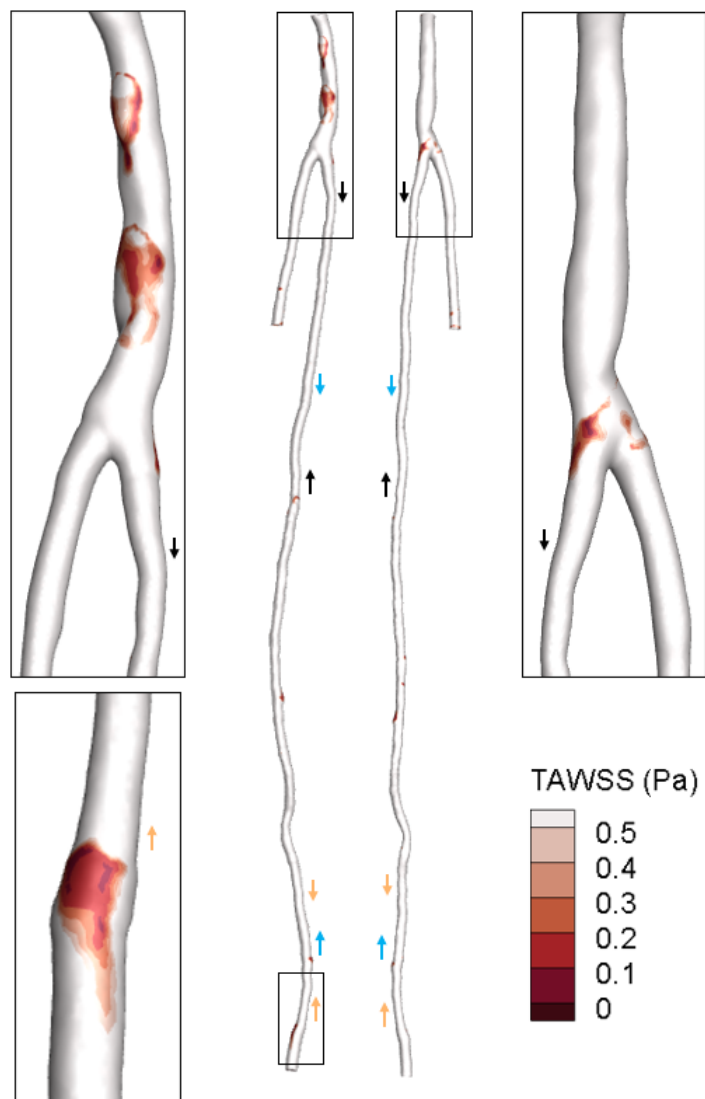


Figure B.1: The TAWSS over one cardiac cycle for the standard simulation of patient 1. The proximal and distal stent markers of the three stents are indicated with the arrows: black for the proximal Viabahn stent, blue for the distal Viabahn stent and orange for the bare metal stent.

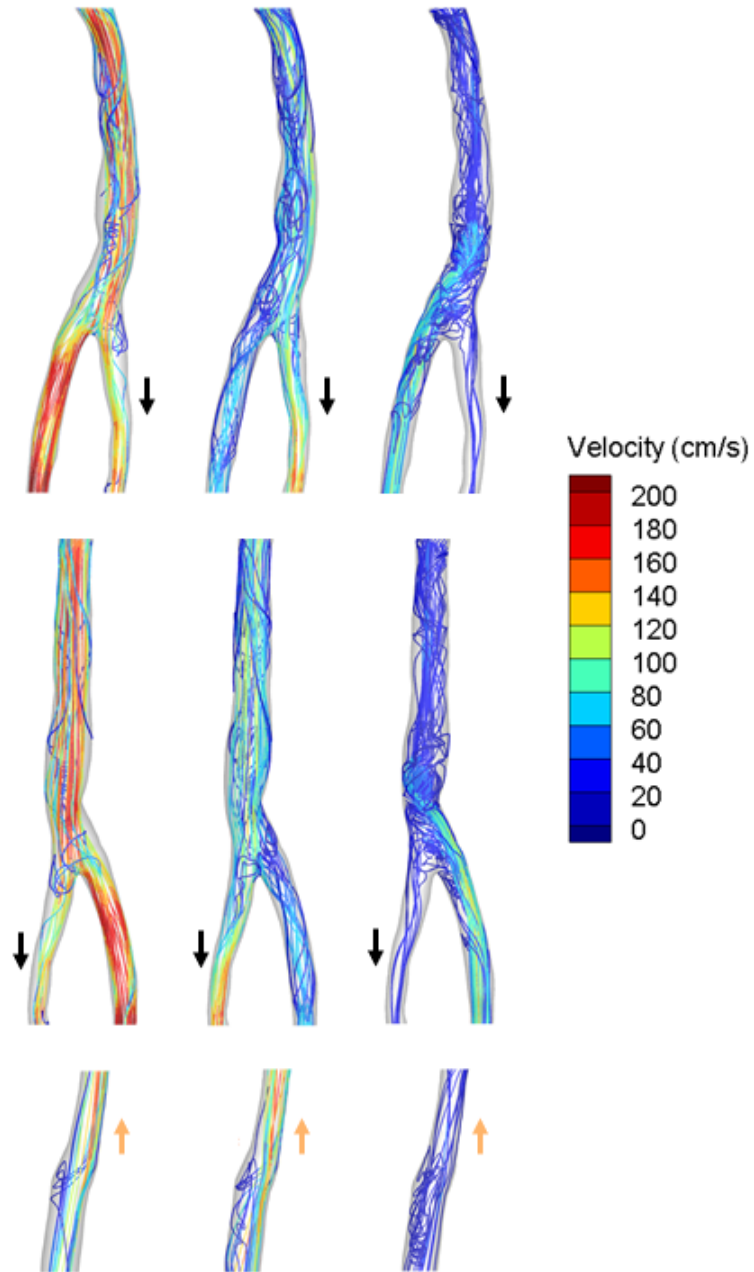


Figure B.2: Velocity streamlines during peak systole (left), systolic deceleration (middle) and peak backflow (right) for the highlighted regions of the standard simulation of patient 1.

B.2 Case S1

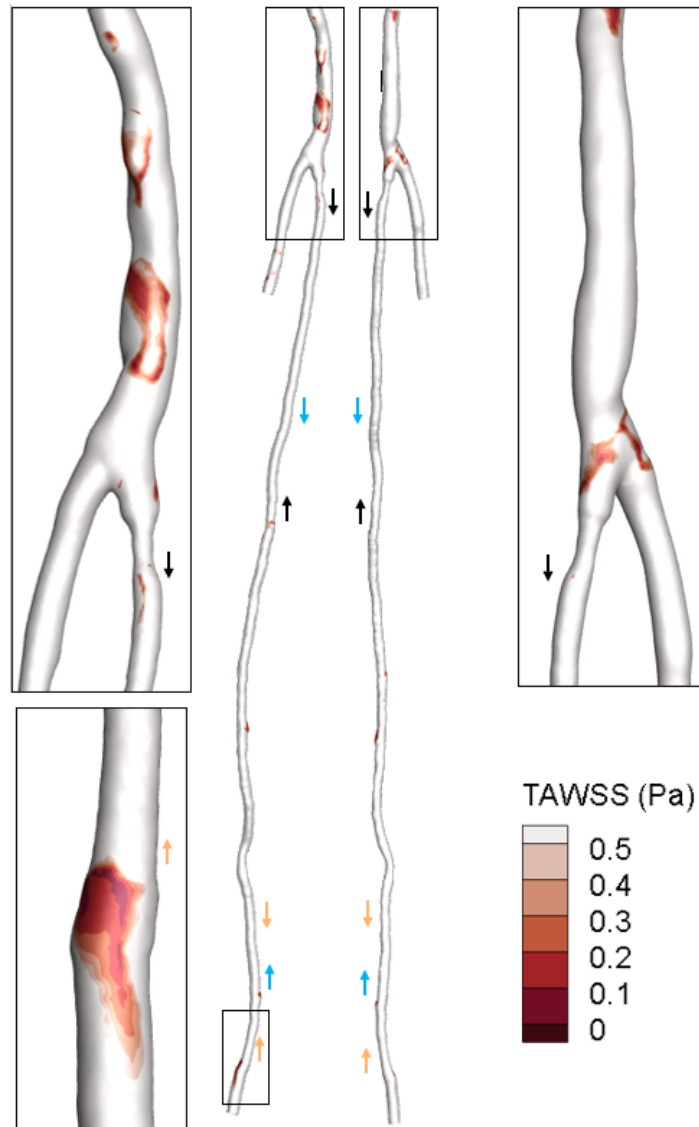


Figure B.3: The TAWSS over one cardiac cycle for patient 1 case S1 (underestimation of vessel lumen). The proximal and distal stent markers of the stent are indicated: black for the proximal Viabahn stent, blue for the distal Viabahn stent, and orange for the bare metal stent. The decreased diameter at the proximal stent marker of the proximal Viabahn is clearly visible.

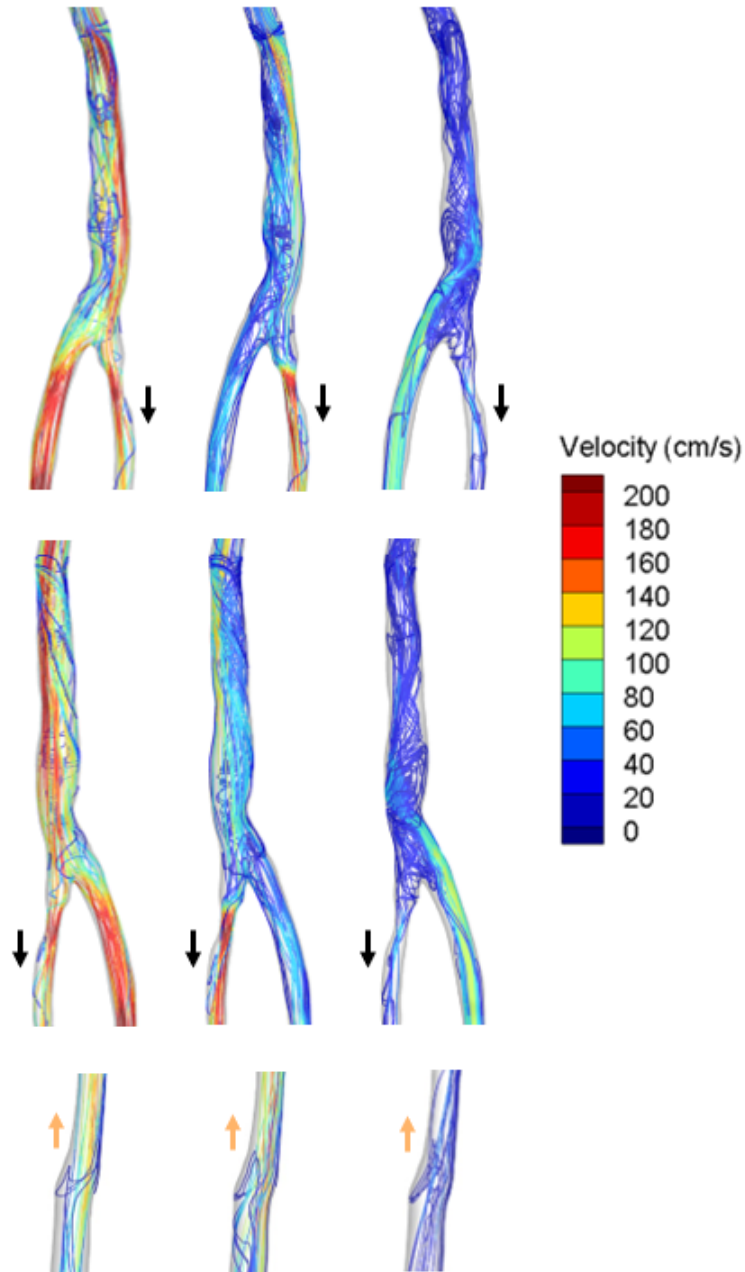


Figure B.4: Velocity streamlines during peak systole (left), systolic deceleration (middle) and peak backflow (right) for the highlighted regions of patient 1 case S1 (underestimation of vessel lumen).

B.3 Case S2

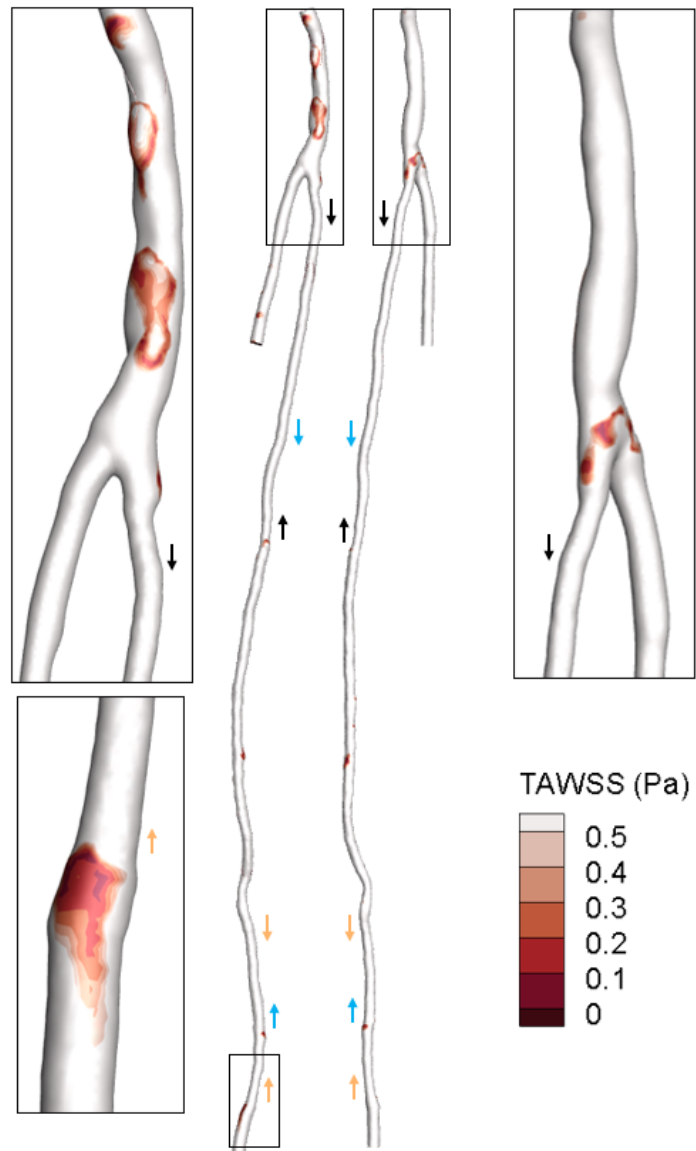


Figure B.5: The TAWSS over one cardiac cycle for patient 1 case S2 (underestimation of vessel lumen). The proximal and distal stent markers of the stent are indicated: black for the proximal Viabahn stent, blue for the distal Viabahn stent and orange for the bare metal stent. The decreased diameter at the proximal stent marker of the proximal Viabahn is visible.

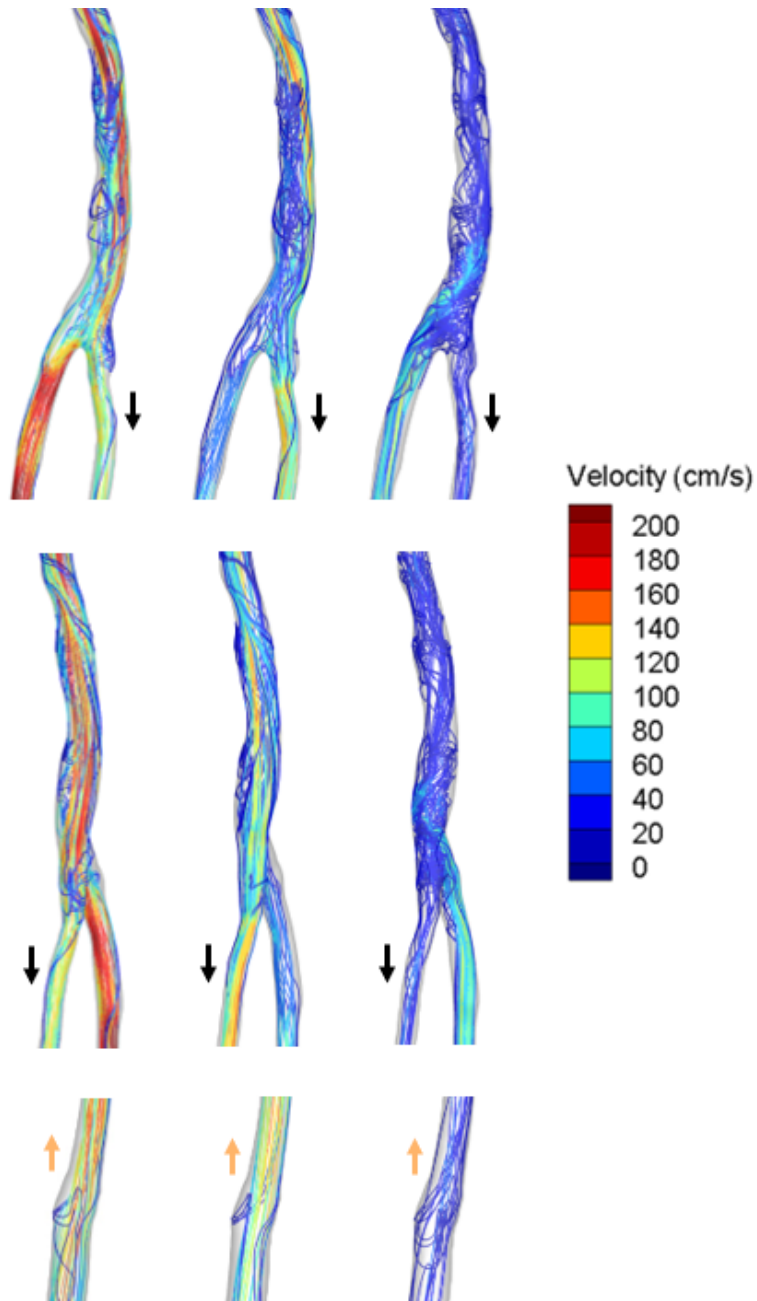


Figure B.6: Velocity streamlines during peak systole (left), systolic deceleration (middle) and peak backflow (right) for the highlighted regions of patient 1 case S2 (underestimation of vessel lumen).

B.4 Case S3

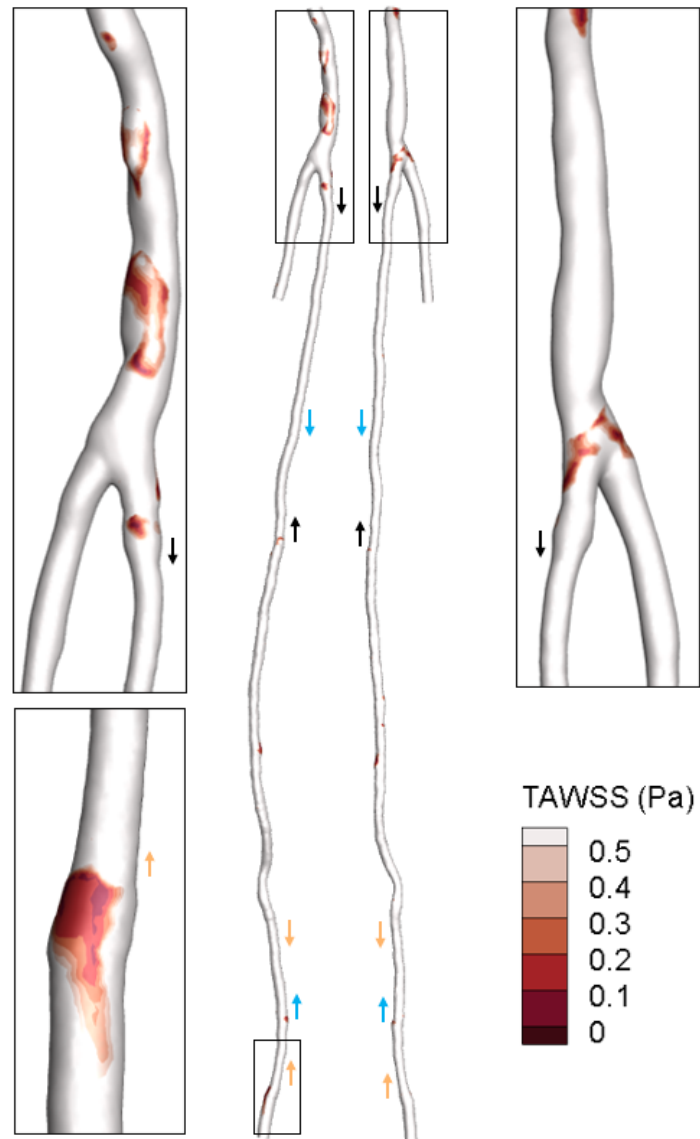


Figure B.7: The TAWSS over one cardiac cycle for patient 1 case S3 (overestimation of vessel lumen). The proximal and distal stent markers of the stent are indicated: black for the proximal Viabahn stent, blue for the distal Viabahn stent and orange for the bare metal stent. The increased diameter at the proximal stent marker of the proximal Viabahn is visible.

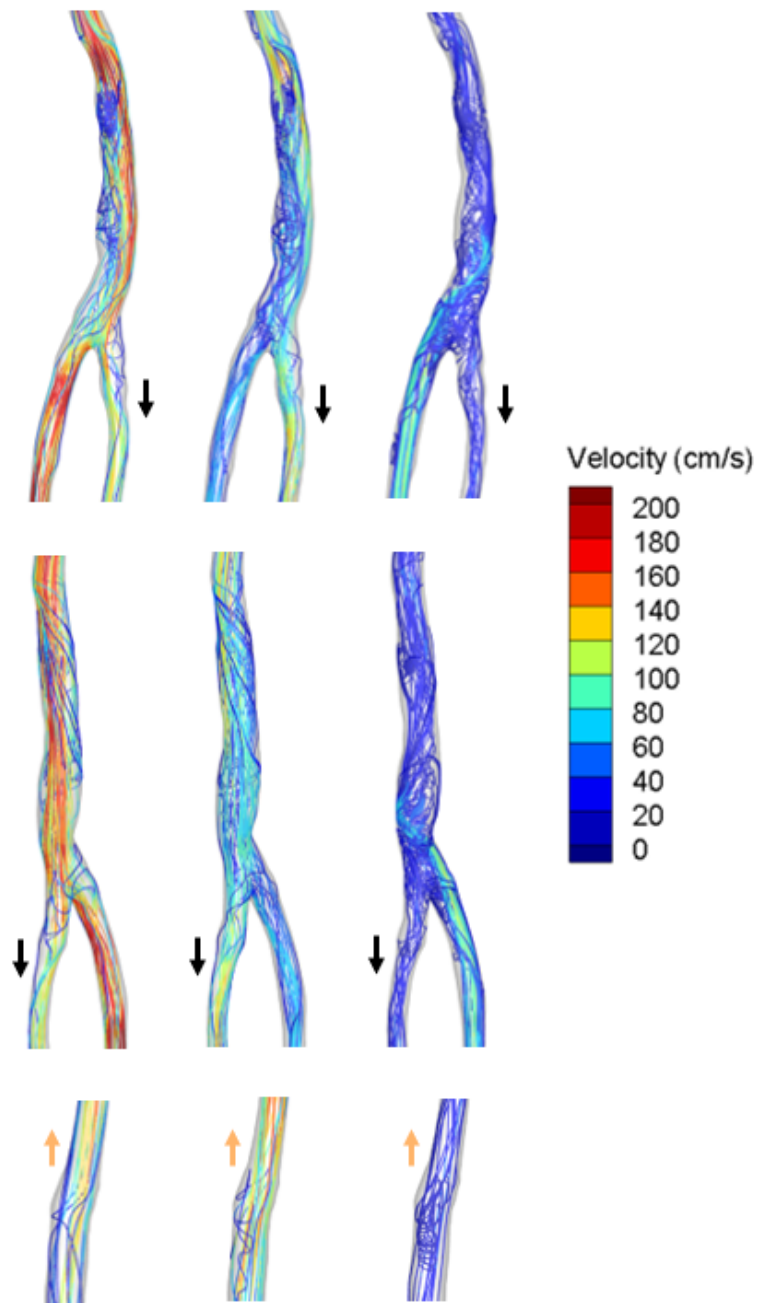


Figure B.8: Velocity streamlines during peak systole (left), systolic deceleration (middle) and peak backflow (right) for the highlighted regions of patient 1 case S3 (overestimation of vessel lumen).

B.5 Case S4

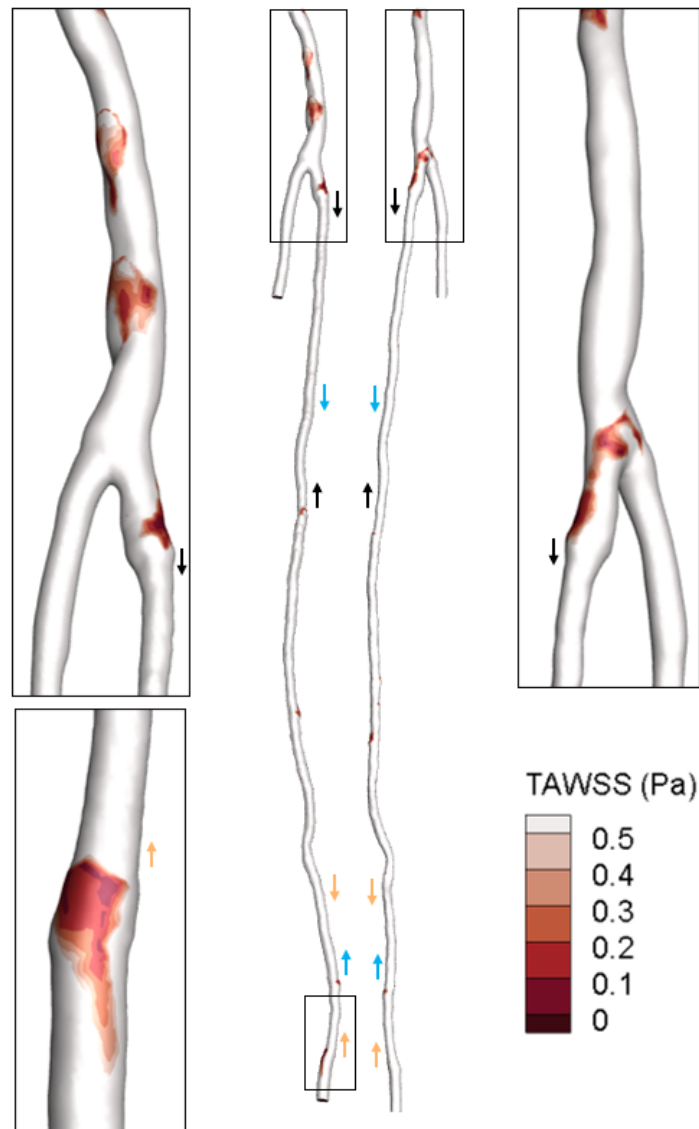


Figure B.9: The TAWSS over one cardiac cycle for patient 1 case S4 (overestimation of vessel lumen). The proximal and distal stent markers of the stent are indicated: black for the proximal Viabahn stent, blue for the distal Viabahn stent and orange for the bare metal stent. The increased diameter at the proximal stent marker of the proximal Viabahn is clearly visible.

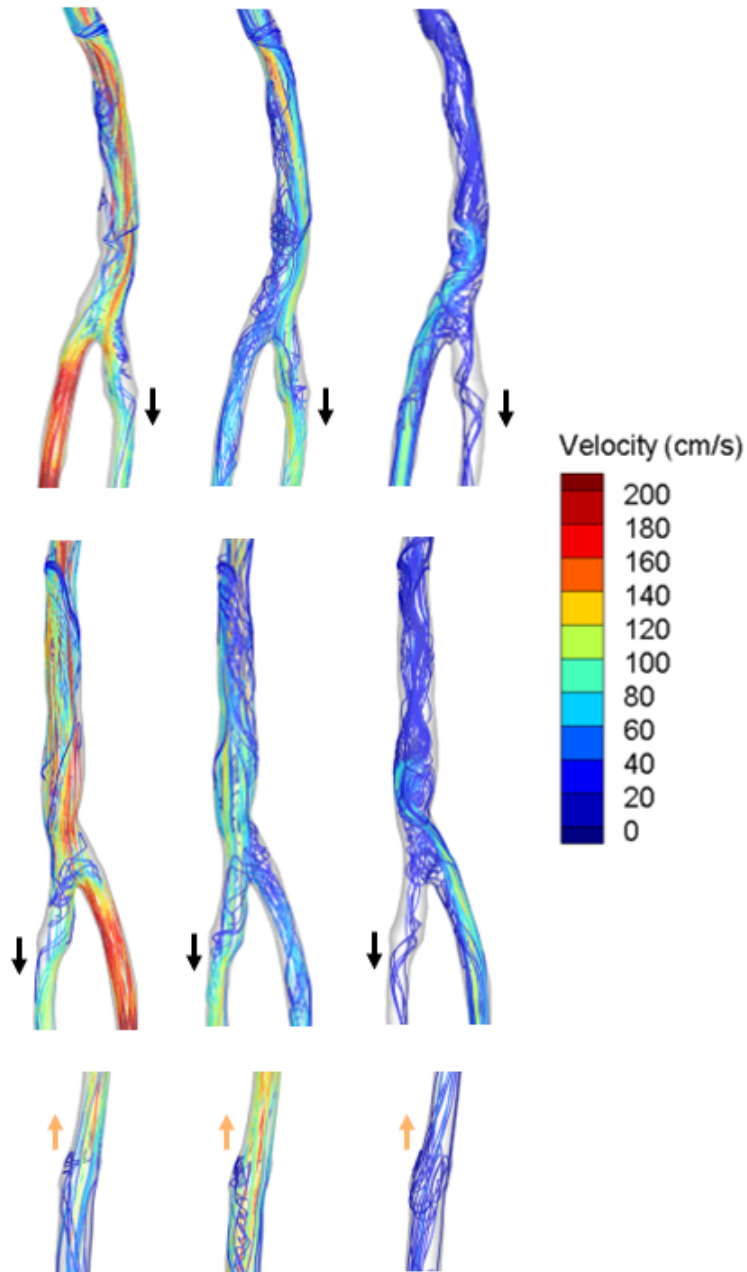


Figure B.10: Velocity streamlines during peak systole (left), systolic deceleration (middle) and peak backflow (right) for the highlighted regions of patient 1 case S4 (overestimation of vessel lumen).

Uncertainty in inlet velocity profile

C.1 Womersley with DUS based flow rate

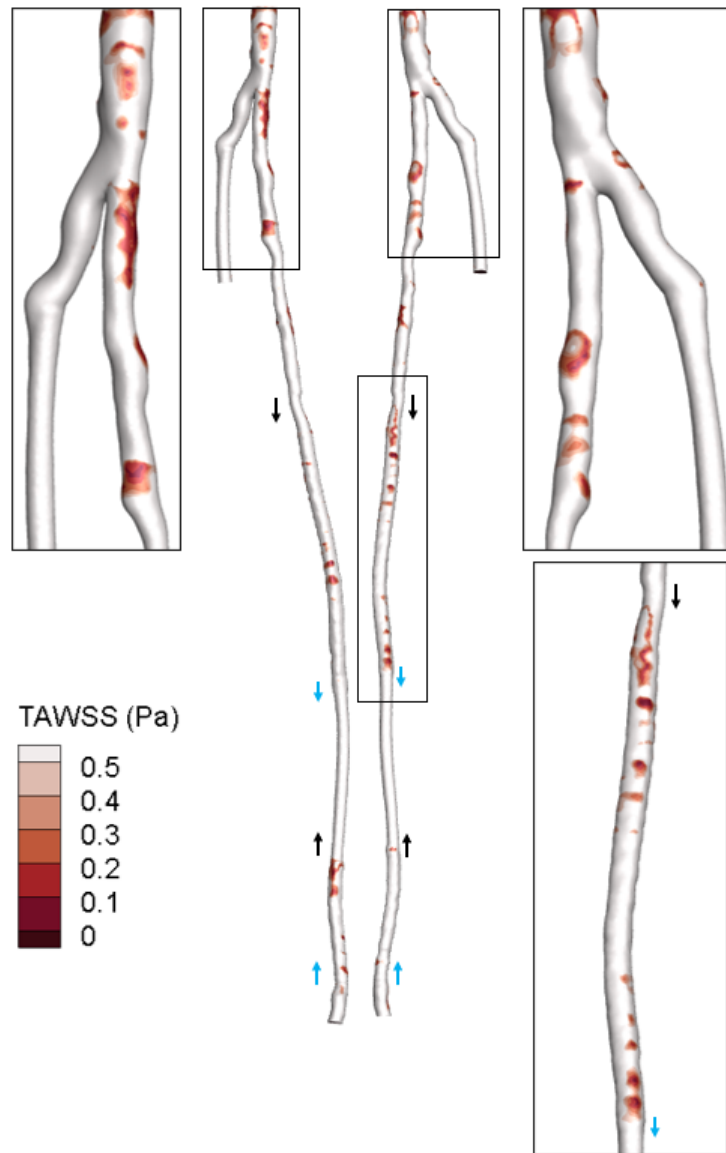


Figure C.1: The TAWSS over one cardiac cycle for patient 2 using a Womersley inlet velocity profile. The proximal and distal stent markers and the direction of the stents are indicated with the arrows: black for the proximal Everflex stent and blue for the distal Everflex stent.

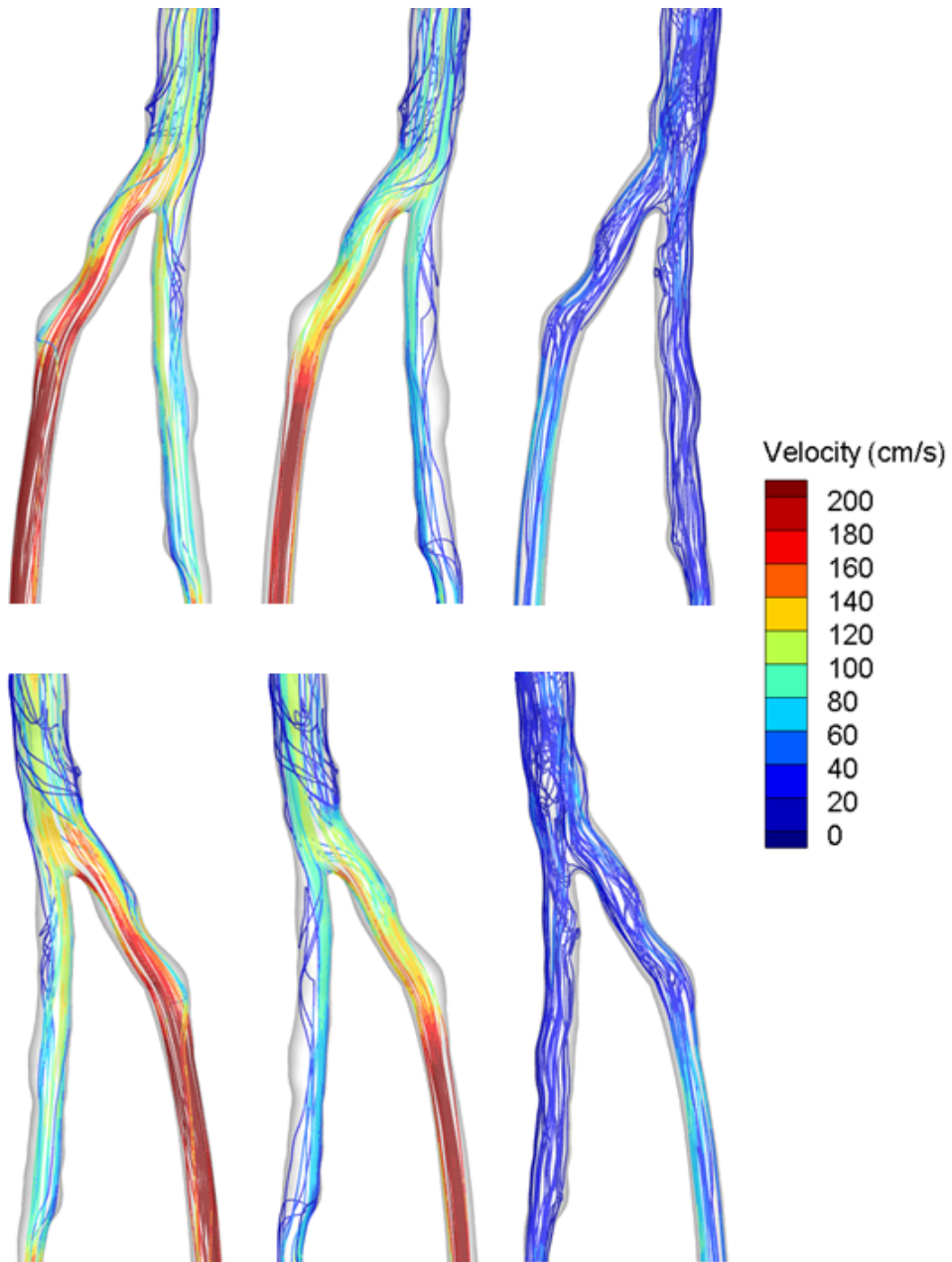


Figure C.2: Velocity streamlines during peak systole (left), systolic deceleration (middle) and peak backflow (right) around the femoral bifurcation for patient 2 using a Womersley inlet velocity profile.

C.2 Womersley with echo PIV based flow rate

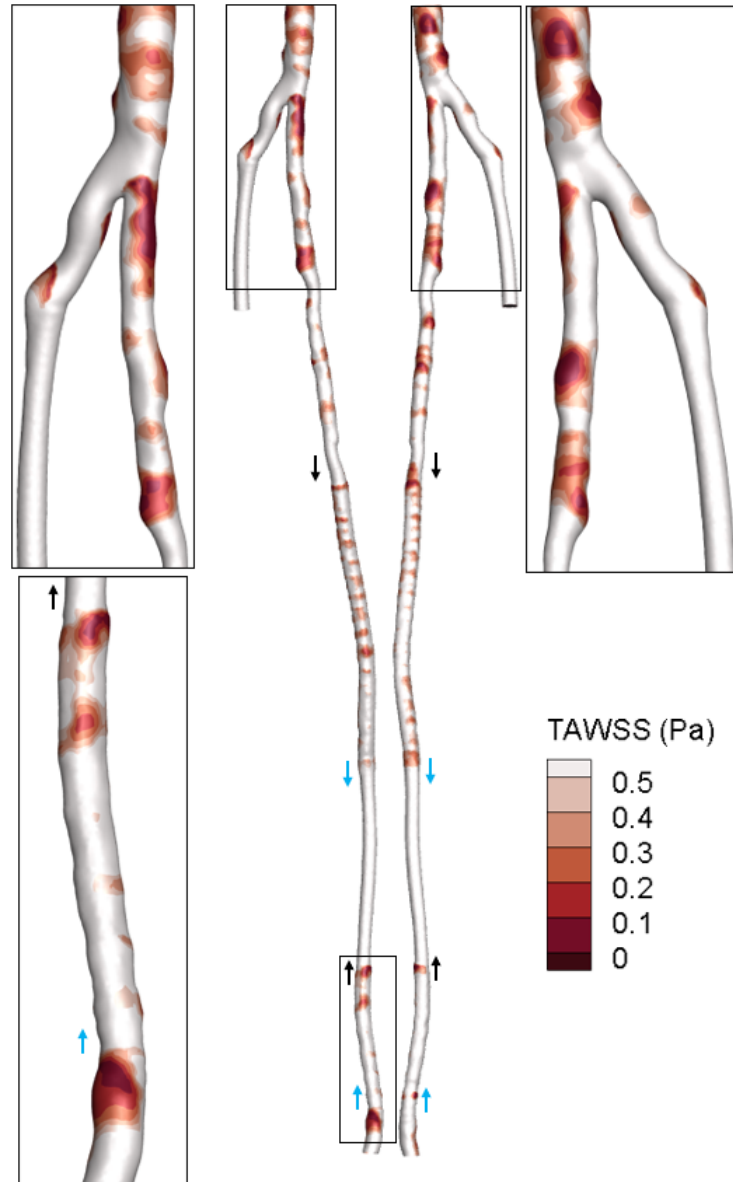


Figure C.3: The TAWSS over one cardiac cycle for patient 2 using an echo PIV inlet velocity profile. The proximal and distal stent markers of the stents are indicated: black for the proximal Everflex stent and blue for the distal Everflex stent.

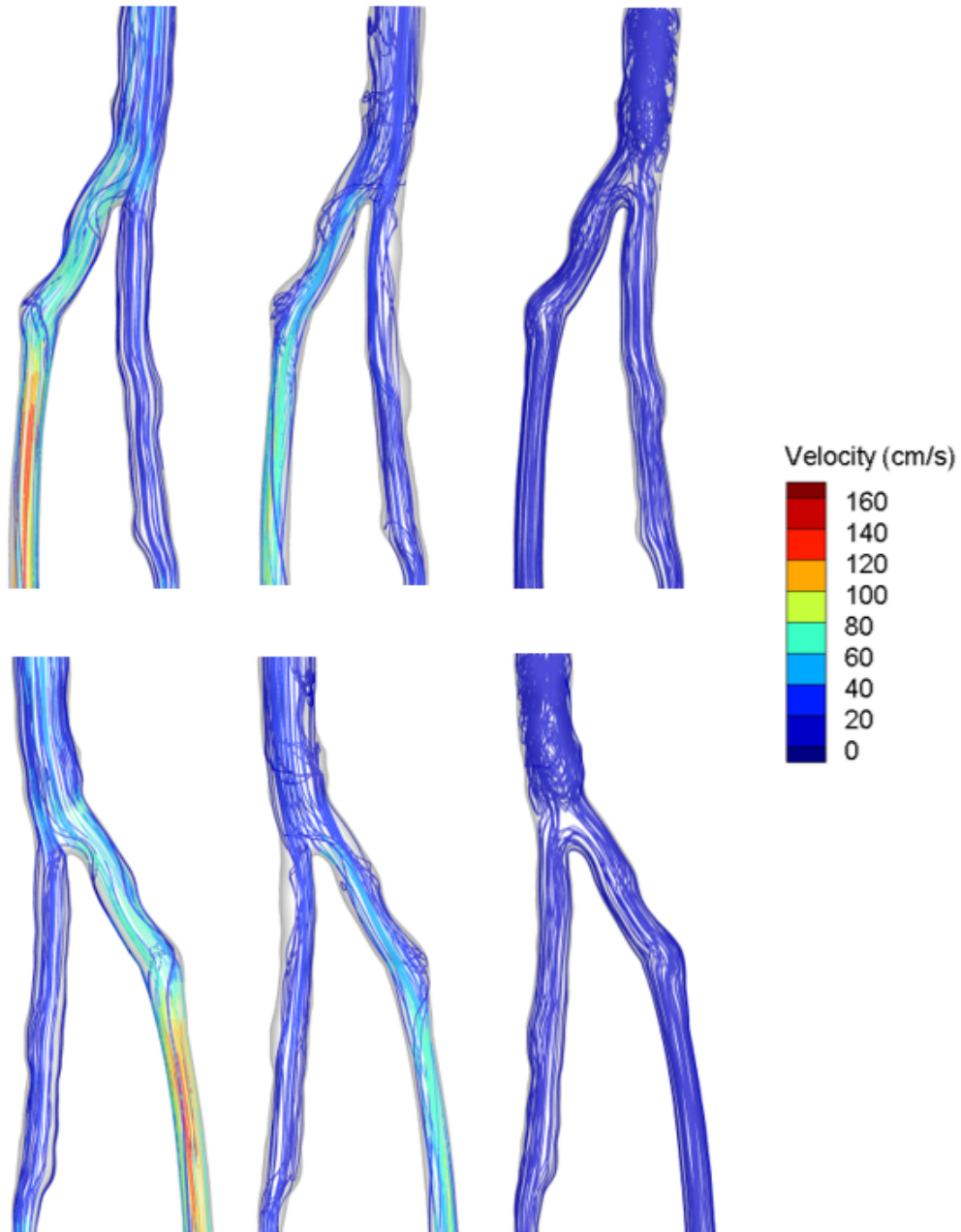


Figure C.4: Velocity streamlines during peak systole (left), systolic deceleration (middle) and peak backflow (right) around the femoral bifurcation for patient 2 using a Womersley inlet velocity profile based on an echo PIV flow rate.

C.3 Echo PIV with echo PIV based flow rate

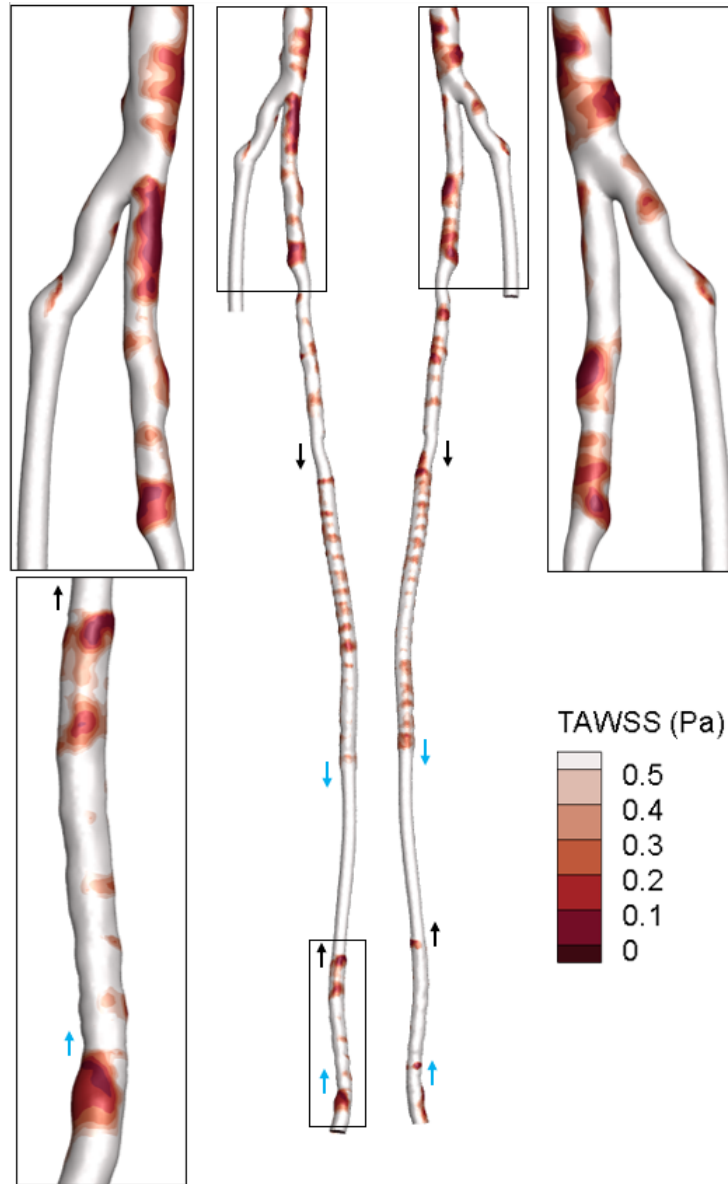


Figure C.5: The TAWSS over one cardiac cycle for patient 2 using an echo PIV inlet velocity profile. The proximal and distal stent markers of the stents are indicated: black for the proximal Everflex stent and blue for the distal Everflex stent.

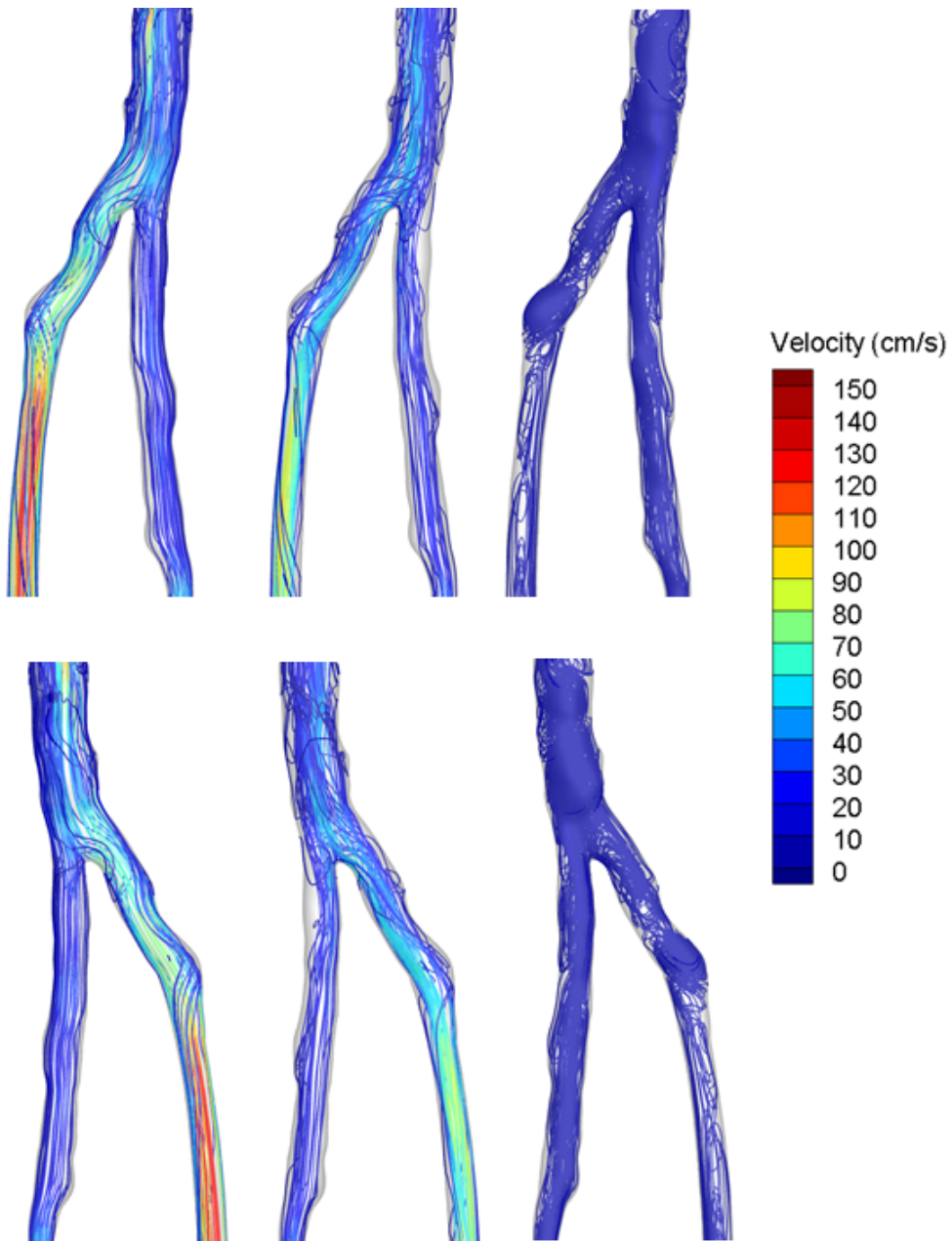


Figure C.6: Velocity streamlines during peak systole (left), systolic deceleration (middle) and peak backflow (right) around the femoral bifurcation for patient 2 using an echo PIV inlet velocity profile.